Some aspects of entanglement in paraxial light fields

A thesis submitted

in partial fulfillment for the award of the degree of

Doctor of Philosophy

by

Soumya Asokan

Department of Physics

Indian Institute of Space Science and Technology

Thiruvananthapuram, India

Certificate

This is to certify that the thesis titled **Some aspects of entanglement in paraxial light fields** submitted by **Soumya Asokan**, to the Indian Institute of Space Science and Technology, Thiruvananthapuram, in partial fulfillment for the award of the degree of **Doctor of Philosophy**, is a bonafide record of the research work carried out by her under my supervision. The contents of this thesis, in full or in parts, have not been submitted to any other Institute or University for the award of any degree or diploma.

Dr. J. Solomon Ivan,
Associate Professor.

Dr. Sudheesh Chethil,
Professor,
HOD, Dept. of Physics

Place: Thiruvananthapuram
Date: April 2024

Declaration

I declare that this thesis titled **Some aspects of entanglement in paraxial light fields** submitted in partial fulfillment for the award of the degree of **Doctor of Philosophy** is a record of original work carried out by me under the supervision of **Dr. J. Solomon Ivan**, and has not formed the basis for the award of any degree, diploma, associateship, fellowship, or other titles in this or any other Institution or University of higher learning. In keeping with the ethical practice in reporting scientific information, due acknowledgments have been made wherever the findings of others have been cited.

Place: Thiruvananthapuram
Date: April 2024

Soumya Asokan
(SC18D037)

Acknowledgements

I would like to express my deepest gratitude to all those who have supported me throughout my journey of pursuing a PhD and the completion of this thesis.

I am immensely grateful to my supervisor, Dr. J. Solomon Ivan, for his unwavering guidance, valuable insights, and continuous encouragement. His expertise, patience, and constructive feedback have been instrumental in shaping this research work. I am indebted to the members of my doctoral committee, Dr. Ravi Pant, Dr. Apoorva Nagar, Dr. Dinesh N. Naik, and Dr. Mahesh S., for their insightful comments, suggestions, and their commitment to improving the quality of this thesis. I would like to express my sincere gratitude to Prof. C. S. Narayanamurthy, Dr. Sudheesh Chethil (Head of the Department), Dr. Naveen Surendran, Dr. S. Murugesh, Dr. Umesh R. Kadhane, and Dr. Ashok Kumar, for their tireless efforts in imparting knowledge and for the mentorship they have provided me throughout my academic journey. I would also like to extend my heartfelt appreciation to lab assistants Lekshmy Devan and Surasreelekshmi. I am grateful to IIST for providing me with the research facilities and resources, which have been instrumental in carrying out this work.

I would like to thank my colleagues and friends Athira T. S., Lekshmi S. R., Ann Mary Tomy, Aswathy M., Haritha A., Sreekala K., Bhasha Sathyan, Varsha M. V., Chithra R. Nair, Sreelekshmi Mohan, Arya Raju, Kathu Sudevan, Olivia Zacharia, Dr. Ameen Yasir, Dr. Pramod Panchal, Dr. Surya Kumar Gautham, Sajith V. S., Kiran Divakar, Dakshin Tillo, Swaliha B. H., Harikrishnan P., Jerin A. Thachil, Deepak Raj R., Sai Meghana Tunikapati, Anjusha Mathew, Dr. Aravind G. P., Swetha V. C., and Athira G. S., for their constant support and motivation. Their presence has made this journey enjoyable and memorable.

Special thanks to my mother, Ajitha Asokan, and other family members for their unwavering support, love, and encouragement throughout my academic pursuits. Their belief in my abilities has been a driving force behind my success. To my late father, Dr. C. V. Asokan, thank you for instilling in me a love for learning and an unwavering belief in the power of education. Your wisdom, guidance, and unwavering encouragement have been a source of strength throughout my academic journey. Although you are no longer physically with me, your spirit continues to inspire and motivate me to pursue excellence in everything I do. To my late brother, Prasanth Asokan, you were not only my sibling but also my closest

confidant and cheerleader. Your unwavering support, enthusiasm, and belief in my abilities pushed me to overcome challenges and reach for my goals.

To everyone mentioned above and those not explicitly named, thank you for your contributions, assistance, and belief in my abilities. This work would not have been possible without your involvement and support.

Soumya Asokan

Abstract

The detection and estimation of entanglement in the optical domain have been extensively explored, drawing inspiration from formal methods developed in quantum theory and quantum information. However, these approaches often introduce complexities in terms of achieving entanglement and necessitate the use of additional devices in the experimental setup. We aim to study entanglement in optics using elementary interferometric setups.

First, we focus on investigating polarization-spatial Gaussian entanglement in a coherent vectorial paraxial light field. We outline a method for detecting polarization-spatial Gaussian entanglement through fringe movement when a linear polarizer is rotated, with the light field passing through the polarizer. The fringe movement is identified as a sufficient condition for detecting polarization-spatial entanglement in coherent paraxial vector light fields. We demonstrate that two Gaussian light fields exhibiting a small relative tilt, substantial spatial overlap, and orthogonal polarizations possess close to 1 ebit of polarization-spatial entanglement. Furthermore, we experimentally demonstrate tunable polarization-spatial Gaussian entanglement using a folded Mach-Zehnder interferometer.

We then move on to address bipartite entanglement in partially coherent paraxial vector light fields. A generalized uncertainty principle suited for the polarization-spatial degrees of freedom is introduced. Partial transpose is implemented through the obtained generalized uncertainty principle. Partial transpose is shown to be necessary and sufficient in detecting entanglement for a class of partially coherent vector light fields which have their spatial part to be Gaussian. Also, an experimental realization of the studied entangled states using classical optical interferometry is outlined.

Next the study delves into the detection of polarization-spatial entanglement by implementing partial transpose on measured intensities. A sufficient criterion for polarization-spatial entanglement in partially coherent light fields based on intensities measured at various orientations of the polarizer, as implied through partial transpose, is outlined. Furthermore, we experimentally demonstrate the detection of polarization-spatial entanglement through the proposed method, using a Mach-Zehnder interferometer setup.

Finally, though a scalar singular paraxial light field does not possess polarization-spatial entanglement, it could possess entanglement between other degrees of freedom such as radial-angular entanglement. Detection and estimation of the same requires the knowledge

of both amplitude and phase of the light field. While the amplitude can be easily measured, the phase has to be retrieved from intensity measurements. Once the phase is successfully retrieved, important properties such as mode expansion, orbital angular momentum, and radial-angular entanglement of the light field can be directly determined based on the estimated field amplitudes. We demonstrate the estimation of the phase of a singular paraxial light field from experimentally measured intensities using a Gerchberg–Saxton type algorithm. A combination of cylindrical lenses which does not conserve the orbital angular momentum of the light field is used in obtaining the measured intensities. Consistent extraction of the phases in regard of the orbital angular momentum is demonstrated both at the input and output transverse planes, using the measured intensities.

Contents

List of Figures

List of Tables

Abbreviations

CCD	charge-coupled device
CHSH	Clauser-Horne Shimony-Holt
ebit	entanglement bit
GS	Gerchberg-Saxton
GSM	Gaussian Schell-model
HG	Hermite Gaussian
LG	Laguerre Gaussian
LHS	left-hand side
OAM	orbital angular momentum
PBS	polarizing beam splitter
QWP	quarter wave plate
RHS	right-hand side
SLM	spatial light modulator
SPP	spiral phase plate

Nomenclature

$A(x, y; z)$	Amplitude function
$\mathbf{B}$	Magnetic field
c	Velocity of light in vacuum
$\mathbf{c}$	$2/w_0^2$
C_θ	$\cos(\theta)$
$C(\tilde{n}; z_i)$	Intensity correlation value between $I(x, y; z_i)$ and $I_{\tilde{n}}(x, y; z_i)$
$C(\rho_p)$	Concurrence
$\det(\cdot)$	Determinant of the matrix
$\dim(\cdot)$	Dimension of the matrix
$\mathbf{d}$	$[\delta_1/\sqrt{c}, \delta_2\sqrt{c}/\kappa]^{\mathrm{T}}$
$\hat{D}(\mathbf{d})$	Displacement operator
$E(\rho_p)$	von-Neumann entropy
$\mathbf{E}$	Electric field
f	Focal length of a thin lens
$f_x\,(f_y)$	Focal length of a thin cylindrical lens whose curvature is along $x\,(y)$ direction
$\mathrm{f}_x\,(\mathrm{f}_y)$	Spatial frequency component along $x\,(y)$ direction
$F\{\cdot\}$	Fourier transform
$F^{-1}\{\cdot\}$	Inverse Fourier transform
$\mathcal{F}(d)$	2×2 matrix corresponding to free propagation by distance d
$\mathbf{F}(d)$	Ray transfer matrix for free propagation by distance d
$\mathcal{F}_d$	Free propagation unitary
h	Planck's constant
$H_m(\cdot)$	Hermite polynomial of order m
$\mathcal{H}$	Hilbert space
i	$\sqrt{-1}$
$\hat{i}$	Unit vector along the x-axis

$I(x, y)$	Intensity function
$I_\theta(x, y)$	Intensity at polarizer oriented at θ
$\hat{j}$	Unit vector along the y-axis
$\hat{k}$	Unit vector along the z-axis
$L_{j-\lvert m\rvert}^{2\lvert m\rvert}(\cdot)$	Associated Laguerre polynomial
L_{op}	Minimum optical path length
$\mathcal{L}(f)$	2×2 matrix corresponding to thin lens of focal length f
$\mathcal{L}_f$	Thin lens unitary
$\mathcal{L}_f^x$	Thin cylindrical lens unitary whose curvature varies in the x-direction
$\mathcal{L}_f^y$	Thin cylindrical lens unitary whose curvature varies in the y-direction
$\mathbf{L}(f)$	Ray transfer matrix for a thin lens of focal length f
$\mathbf{L}_x(f)$ [$\mathbf{L}_y(f)$]	Ray transfer matrix for a thin cylindrical lens of focal length f whose curvature is along x (y) direction
$\lvert m\rangle$	Fock state which represents the wave function $\psi_m(x)$
n, n_1, n_2	Refractive indices of the given medium
$\mathbf{p}$	(p_x, p_y)
p_x (p_y)	$-i/\kappa(\partial/\partial x)$ ($-i/\kappa(\partial/\partial y)$)
$\hat{p}_x$ ($\hat{p}_y$)	$-i/\kappa(\partial/\partial x)$ ($-i/\kappa(\partial/\partial y)$) in the position representation
$\mathbf{P}(d)$	Symplectic matrix associated with two-dimensional Fourier transform
$\mathbf{P}_y(d)$	Symplectic matrix associated with a constituent of partial Fourier transform
R_z	Radius of curvature at a particular z
$\mathbf{S}$	4-dimensional symplectic matrix
S	2-dimensional symplectic matrix
$\mathrm{S}_0, \mathrm{S}_1, \mathrm{S}_2, \mathrm{S}_3$	Stokes parameters
$S(\rho_p)$	Degree of polarization
S_θ	$\sin(\theta)$
$Sp(2, \mathbb{R})$	Symplectic group in 2 dimensions
$Sp(4, \mathbb{R})$	Symplectic group in 4 dimensions
t	time
$\mathrm{tr}(\cdot)$	Trace of the matrix
$\hat{\mathbf{U}}(\mathbf{S})$	Most general quadratic in the operators $\hat{x}$, $\hat{p_x}$, $\hat{y}$, and $\hat{p}_y$
$\hat{U}_x(S)$ [$\equiv \hat{U}(S)$]	Most general quadratic in the operators $\hat{x}$ and $\hat{p_x}$
$\hat{U}_y(S)$	Most general quadratic in the operators $\hat{y}$, and $\hat{p}_y$

$\hat{\mathcal{U}}(S, \mathbf{d})$	Most general Gaussian unitary in the operators $\hat{x}$ and $\hat{p_x}$ including translations
$\hat{U}_{12}$	Polarization-conditional Gaussian unitary transformation
$\hat{\mathcal{U}}_{12}$	Polarization-conditional Gaussian unitary transformation including translations
$\mathbf{V}$	4×4 variance matrix
V	2×2 variance matrix
w_0	Width of the paraxial light field at waist plane
w_z	Width of the paraxial light field at a particular z
$W(\mathbf{x}, \mathbf{p}) \equiv W(\boldsymbol{\xi})$	Wigner distribution function
$W(x, p_x) \equiv W(\xi)$	Wigner distribution function corresponding to $\hat{\Gamma}$
$W_G(\xi)$	Wigner distribution function corresponding to $\hat{\Gamma}_G$
$\hat{x}$	x in the position representation
$\|x\rangle$	Eigenstate of the position operator $\hat{x}$
$\mathbf{x}$	(x, y)
x_j	Distance between the point p_j and the optical axis in the x–z plane
x'_j	Angle between the ray going through the point p_j and the optical axis in the x–z plane
x_j	$[x_j, x'_j]^{\mathrm{T}}$
$\hat{y}$	y in the position representation
$\|y\rangle$	Eigenstate of the position operator $\hat{y}$
y_j	Distance between the point p_j and the optical axis in the y–z plane
y'_j	Angle between the ray going through the point p_j and the optical axis in the y–z plane
y_j	$[y_j, y'_j]^{\mathrm{T}}$
z_r	Rayleigh range
$\mathbb{0}$	2×2 zero matrix
$\|0\rangle$	$[1, 0]^{\mathrm{T}}$
$\mathbb{1}$	2×2 identity matrix
$\|1\rangle$	$[0, 1]^{\mathrm{T}}$
θ_i	Angle of incidence
θ_r	Angle of refraction
$\varphi_{m_1 m_2}(x, y; z)$	Hermite Gaussian light field at a particular z
$\varphi(x, y, z, t)$	Scalar function of space-time variables
$\varphi_s(x, y, z)$	Spatial part of φ

$\varphi_t(t)$	Temporal part of φ
ζ_z	$\tan^{-1}(z/z_r)$
$\psi(x, y; z)$	Paraxial scalar light field
$\psi_{jm}(r, \theta; z)$	Laguerre Gaussian light field at a particular z
$\psi_m(x)$	Hermite Gaussian mode in a single variable at the waist plane
$\psi_m(x; z)$	Hermite Gaussian mode in a single variable at a particular z
$\psi(r)$	Radial part of first-order Laguerre-Gaussian modes
$\Psi(x, y)$	Paraxial vector light field
$\mathrm{e}^{i\chi}$	Angular part of first-order Laguerre-Gaussian modes
$\Delta(x, y)$	Lens thickness function
λ	Wavelength of the light field
$\lambda_\pm$	Eigenvalues of ρ_p
$\mathbf{\Lambda}$	$\mathrm{diag}(\Lambda, 1/\Lambda)$
μ_0	Permeability of free space
ϵ_0	Permittivity of free space
∇	Gradient operator
δ_α	Tilt in the x-z direction
κ	$2\pi/\lambda$
τ	Orbital angular momentum
ω	κc
$\phi(x, y; z)$	Phase of the light field
$\lvert\eta\rangle$	Coherent polarization state
ξ	$[x, p_x]^{\mathrm{T}}$
$\hat{\xi}$	$[\hat{x}, \hat{p}_x]^{\mathrm{T}}$
$\Delta\hat{\xi}$	$[\Delta\hat{x}, \Delta\hat{p}_x]^{\mathrm{T}}$
$\boldsymbol{\xi}$	$[x, y, p_x, p_y]^{\mathrm{T}}$
$\hat{\boldsymbol{\xi}}$	$[\hat{x}, \hat{y}, \hat{p}_x, \hat{p}_y]^{\mathrm{T}}$
$\Delta\hat{\boldsymbol{\xi}}$	$[\Delta\hat{x}, \Delta\hat{p}_x, \Delta\hat{y}, \Delta\hat{p}_y]^{\mathrm{T}}$
$\rho(x, y)$	Density matrix
ρ_p	Reduced density matrix
ρ_{ij}	Entries of ρ_p
$\Gamma(x_1, x_2)$	Cross-spectral density of a partially coherent scalar light field
$\hat{\Gamma}$	Cross-spectral density operator of a partially coherent scalar light field
$\hat{\mathbf{\Gamma}}$	Cross-spectral density operator of a partially coherent vector

	light field
$\hat{\Gamma}_G$	Gaussian cross-spectral density operator of a partially coherent scalar light field
$\Gamma_{sc}(x_1, x_2)$	Cross-spectral density of a scalar GSM light field
$\hat{\Gamma}_{sc}$	Cross-spectral density operator of a scalar GSM light field

Chapter 1

Introduction

1.1 Entanglement in optics

Quantum mechanical systems and classical optic systems share the commonality of the superposition principle. As a result, it is possible to find instances when one mimics the other. For instance, in Refs. [1–5] quantum random walks have been effectively simulated using classical light, and in Refs. [6, 7] the classical optic analogue of teleportation has been demonstrated. Similarly, quantum mechanical matter has been found to reproduce standard classical optical phenomena such as interference and diffraction [8–13]. A fundamental consequence of the superposition principle when two or more degrees of freedom are involved is the notion of entanglement.

Entanglement is defined as inseparability of sums of product states that exist in different vector spaces. The concept of entanglement has been well explored both in the quantum domain [14–24] as well as in the classical domain [6, 7, 25–59]. The various similarities and differences between the quantum optical and classical optical entanglement were discussed in Refs. [28, 31, 32, 35, 50, 55]. Classical light fields having entangled degrees of freedom have been of much interest lately, and have found various applications in the possible simulation of quantum phenomena [6, 7, 39–44]. They have also been used in encoding information for optical communication [6, 7, 37, 38], and polarization metrology [29]. Polarization spatial entangled light fields helped resolve the problem of defining Mueller matrices in a consistent manner [45].

Bipartite entanglement has been well explored in several works and there exist several methods towards their detection such as violation of Bell-type inequalities [33, 34, 36, 53, 55–59], and the use of positive maps [15, 21–23, 60–64]. Experimental detection of polarization-spatial entanglement by violation of Bell-type inequality, implemented through intensity measurements, was demonstrated in Refs. [33, 36, 55, 56, 58]. Note that

implementation of Bell inequality in the polarization-spatial context, requires the estimation of expectation values of observables pertaining to both polarization and spatial degrees of freedom, which is in principle obtained through multiple intensity measurements (see for instance Refs. [33, 57]). Maximal violation of Bell-type inequality is obtained on a maximally polarization-spatial entangled light field as shown in Refs. [33, 36, 56, 58]. The case of violation of Bell-type inequality in partially coherent polarization-spatial entangled light fields was considered in Refs. [36, 58].

Bell-type inequalities witness entanglement through expectation values of local observables. Positive maps on the other hand are implemented on the density operator, and entanglement is inferred through violation of positivity conditions. A method to detect bipartite entanglement has been through the use of the partial transpose map [60]. This map has been found to be necessary and sufficient in detecting bipartite entanglement in certain finite dimensional [14, 61, 62, 64] as well as infinite dimensional contexts [21–23, 63]. The presence of bipartite entanglement not detected by partial transpose is well known, and the separability problem is still open in a generic bipartite setting [14, 15]. Bipartite entanglement not detected by partial transpose has interesting physical consequence such as the existence of bound entanglement [21, 24].

1.2 Quantum entanglement and its classical analogue

The association between entanglement and quantum mechanics is so strong that the prefix "quantum" is often considered redundant; entanglement is inherently quantum. However, the defining characteristic of entangled quantum states is their non-separability, a trait not exclusive to the quantum domain.

Let us consider a quantum system $\mathcal{S}$ consisting of two subsystems denoted by $\mathcal{S}_1$ and $\mathcal{S}_2$, respectively. For instance, a scenario where two particles with mass m are confined to move along a line, with coordinates x_1 and x_2, respectively, connected to the equilibrium point by two identical springs of spring constant $k = m\omega^2$, with ω being the angular frequency. This forms a bipartite quantum system governed by the Hamiltonian $\hat{H} = \hat{H}_1 + \hat{H}_2$, where

$$\hat{H}_{i=1,2} = \frac{1}{2m}\hat{p}_i^2 + \frac{1}{2}m\omega^2\hat{x}_i^2, \tag{1.1}$$

with $\hat{p}_i$ and $\hat{x}_i$ being the momentum and position operators, respectively. In this case, the two subsystems $\mathcal{S}_1$ and $\mathcal{S}_2$ are associated with the two particles.

Now contemplate a second scenario where a single particle of mass m is moving across

a plane (x_1, x_2), connected to the equilibrium point $x_1 = 0 = x_2$ by a spring of spring constant k. Here we have a two-dimensional harmonic oscillator with Hamiltonian

$$\begin{aligned}\hat{H} &= \frac{1}{2m}(\hat{p}_1^2 + \hat{p}_2^2) + \frac{1}{2}m\omega^2(\hat{x}_1^2 + \hat{x}_2^2) \\ &= \hat{H}_1 + \hat{H}_2, \end{aligned} \tag{1.2}$$

where $\hat{H}_i$ is given by Eq. (1.1). In this case, the two subsystems $\mathcal{S}_1$ and $\mathcal{S}_2$ are associated with the two Cartesian coordinates of the single particle. In both cases the Hamiltonian $\hat{H}$ is the same. The general state vector $|\Psi\rangle$ which satisfies the Schrödinger equation $i/\kappa\partial|\Psi\rangle/\partial t = \hat{H}|\Psi\rangle$, belongs to a Hilbert space $\mathcal{H}$ which in turn is the tensor product of two Hilbert spaces associated with the two subsystems $\mathcal{S}_1$ and $\mathcal{S}_2$: $\mathcal{H} = \mathcal{H}_1 \otimes \mathcal{H}_2$.

On comparing the two cases considered above, the main difference lies in the fact that in the first case the two subsystems are associated with two distinct physical objects (two particles) that can have spatial separation, whereas, in the second case the two subsystems are associated with the orthogonal coordinates of a single physical object (single particle). This difference has serious consequences when the state vector $|\Psi\rangle$ is entangled, that is,

$$|\Psi\rangle \neq |\psi_1\rangle \otimes |\psi_2\rangle. \tag{1.3}$$

Here, $|\psi_1\rangle$ and $|\psi_2\rangle$ represent the states of the subsystems $\mathcal{S}_1$ and $\mathcal{S}_2$, respectively.

The entanglement in both cases considered above can be classified as two different types of entanglement [26, 28, 35]: (i) intersystem or multiparticle entanglement and (ii) intrasystem or entanglement between different degrees of freedom of a single particle. Note that, although these look deceptively similar, only type (i) yield non-local correlations and only type (ii) has a classical analogy. Non-locality is a fundamental aspect of quantum mechanics and should not be confused with quantum entanglement. Intrasystem entanglement can manifest in both quantum and classical systems, and it inherently possesses a local nature by definition. This is because the two or more entangled degrees of freedom are confined within the same physical object. In our work, we deal with classical optical analogue of intrasystem entanglement. A typical example would be a paraxial vector light field non-separable in the polarization and spatial degrees of freedom. Such entangled light fields are discussed in detail in the next chapter.

A minimal definition of entanglement between different degrees of freedom of a classical system as given in Ref. [55] is: "If in a physical system described by the laws of classical wave mechanics, an observable quantity that depends on two (or more) independent

degrees of freedom, say x and y, can be mathematically represented by a non-separable function $f(x, y)$ such that $f(x, y) \neq u(x)v(y)$, then such a system is said to display classical entanglement". In Ref. [35], on exploring an analogous model system for quantum information processing using classical wave optics, researchers have discovered that while the classical model can effectively mimic many aspects of entanglement, it falls short in replicating quantum non-locality.

1.3 Summary of results obtained in the thesis

In this section we will outline the results obtained in this thesis. Numerous works have been done towards detection and estimation of entanglement in the optical context, by importing and implementing formal methods developed in quantum theory/quantum information [34, 56, 59, 65]. Typically this renders the experiment cumbersome in terms of the means to achieve entanglement, and also in terms of the use of additional devices in the setup. In this thesis, we demonstrated using an elementary interferometric setup, generation, detection and estimation of pure state entanglement. Tunable polarization-spatial Gaussian entangled light fields were generated using a folded Mach-Zehnder setup. Fringe movement was shown to be a sufficient criterion in detecting entanglement. Estimation of entanglement was demonstrated using polarimetry. As understood formally from the Schmidt decomposition [66], orthogonal modes were a necessity for maximal entanglement and sophisticated experimental setups, that use devices such as spatial light modulators (SLMs), dove prisms and digital micromirror devices [34, 56, 59, 65], were required in achieving it. Nevertheless, we were able to show that two Gaussian light fields with a small relative tilt (of the order of 10^{-4} radians), but with substantial spatial overlap, and orthogonal polarizations, can have close to maximal entanglement. This is attributed to the inherent wavelength dependent scale in the problem.

As mentioned earlier, partial transpose map has been found to be both necessary and sufficient for detecting entanglement in certain finite and infinite dimensional systems. In our work, we specifically study bipartite entanglement in $2 \times \infty$ dimensional systems. We settled the issue of separability between the polarization and spatial degrees of freedom for a particular class of states which have their spatial part to be Gaussian. Negativity under partial transpose was shown to be necessary and sufficient in detecting entanglement. To implement the partial transpose, we introduced a generalized uncertainty principle tailored to our specific context. Furthermore, we propose an experiment using the Mach-Zehnder interferometer to realize these entangled states. This setup provides us with a versatile

tool for engineering polarization-spatial entanglement, which holds potential applications in fields such as polarization metrology and optical communication that utilize vector light fields.

Moreover, we have introduced a technique for detecting polarization-spatial entanglement in partially coherent vector light fields based on intensity measurements. The implementation of partial transpose involves sequentially adding intensities measured at different polarizer orientations. We establish that the negativity of the combined intensities serves as a sufficient criterion for detecting polarization-spatial entanglement. To experimentally demonstrate the detection of polarization-spatial entanglement using this method, we use a Mach-Zehnder interferometer setup. Generating partially coherent vector light fields by simulating them as a sequence of pure input polarization-spatial entangled states, we show that these light fields violate the established criterion, thus indicating the presence of polarization-spatial entanglement. Although the considered examples are restrictive, the method itself is applicable to any arbitrary partially coherent polarization-spatial states for entanglement detection.

Further, we have successfully conducted experiments to extract phases with dislocations from singular light fields using a Gerchberg Saxton (GS) type algorithm. The phases of field amplitudes at the output, which possess fractional orbital angular momentum (OAM), were also extracted. These experimental results validate the theoretical approach outlined in Ref. [67]. An important aspect of our method is its generality in extracting dislocated phases from intensity measurements without imposing constraints on the mode expansion of the light field. Consequently, the mode expansion, OAM, and the radial-angular entanglement [68] of the light field can be straightforwardly derived from the estimated field amplitudes at both the input and output transverse planes. This demonstrates the versatility and broad applicability of our approach in extracting various properties of the light field.

1.4 Organization of the thesis

We have given an outline of the thesis in Chapter 1. Chapter 2 provides an overview of the fundamental concepts in optics. Section 2.1 discusses ray transfer matrices that correspond to various symmetric and asymmetric optical transformations in the paraxial limit. In Section 2.2, we delve into Maxwell's equations, the paraxial wave equation, and their solutions. This section establishes the groundwork for understanding wave propagation in optical systems. Section 2.3 explains the Huygen's Fresnel diffraction principle and the Fresnel approximation for free space propagation. These play a crucial role in the devel-

opment of an algorithm for free space propagation as outlined in Ref. [69]. Section 2.4 outlines thin lens as a phase transformation, whereas the unitary representation of various optical transformations is discussed in Section 2.5. Furthermore, Sections 2.6, 2.7, 2.8 and 2.9 explores the Wigner distribution function, variance matrix, uncertainty principle and OAM associated with a paraxial light field, respectively. This highlights the interconnectedness of different aspects of the light field and their implications in optical systems. In Section 2.10 we provide a brief overview of partial coherence in scalar paraxial light fields. Vector light fields are introduced in Section 2.11. Partial coherence in vector paraxial light fields is outlined here. Also, a generalized uncertainty principle suited for the polarization spatial degrees of freedom of a paraxial light field is obtained. Finally in Section 2.12, light fields having entangled degrees of freedom is discussed. Polarization-spatial entanglement in coherent and partially coherent light fields is discussed here. Through these discussions, Chapter 2 provides a solid foundation of knowledge on optics, enabling a deeper understanding of the subsequent chapters in the thesis.

Chapter 3 focuses on polarization-spatial entanglement in coherent paraxial light fields. In Section 3.2, we explore the detection of polarization-spatial entanglement through fringe movement. Section 3.3 presents a comprehensive overview of the method used for estimating polarization-spatial entanglement. This estimation method involves employing a quarter wave plate (QWP) and a linear polarizer to analyze the entangled light fields. In Section 3.4, we delve into a theoretical analysis that showcases an intriguing finding. We demonstrate that even with a small relative tilt between two Gaussian light fields, substantial spatial overlap, and orthogonal polarizations, a close to 1 ebit (entanglement bit) of polarization-spatial entanglement can be achieved. This phenomenon can be attributed to the inherent wavelength dependent scale within the problem. The experimental demonstration of the detection of polarization-spatial entanglement using fringe movement, and the estimation of this entanglement are outlined in the same section. These experimental demonstrations further validate the theoretical concepts discussed. Finally, we conclude with some closing remarks in Section 3.5.

Chapter 4 explore bipartite entanglement in $2 \times \infty$ dimensional systems, that have their spatial part to be Gaussian. In Section 4.2, we introduce a specific category of states for which we investigate the separability problem. To address the polarization-spatial entanglement, we employ the generalized uncertainty principle suitable for the present context to implement the partial transpose. The key outcome of the research discussed in this chapter is summarized here. In Section 4.3, we explore the experimental realization of the studied entangled states using classical optical interferometry. Finally, we conclude with some

closing remarks in Section 4.4.

Chapter 5 presents an approach for detecting entanglement in a partially coherent vector light fields by implementing partial transpose using intensities measured at different orientations of the polarizer on the incoming light field. In Section 5.2, we explain the implications of partial transpose on the measured intensities obtained from varying polarizer orientations. Section 5.3 focuses on discussing the detection of polarization-spatial entanglement through the partial transpose map implemented using the measured intensities. Furthermore, we provide an outline of an experimental demonstration of the proposed method in this section. The experimental results are subsequently discussed in Section 5.4. Finally, we conclude the chapter with some closing remarks in Section 5.5.

In Chapter 6, we present an experimental demonstration of a GS-type phase retrieval algorithm, for retrieving phases with dislocation. This algorithm uses a transformation outlined in Ref. [67]. The first-order optical system considered here consists of a combination of three cylindrical lenses that do not conserve OAM. Once the phase is retrieved, the mode expansion, OAM, and radial-angular entanglement [68] of the light field can be straightforwardly extracted from the estimated field amplitudes. Section 6.2 provides an explanation of the essential optical transformations and their corresponding realizations employed in our algorithm. In Section6.3, we elaborate on our proposed algorithm and describe the experimental setup. The results obtained from both the experiment and the algorithm are outlined in this section. Finally, we conclude the chapter with some closing remarks in Section 6.4.

Chapter 7 serves as the concluding section of the thesis, where we provide a concise summary. We also take the opportunity to suggest potential areas for future research and exploration.

Chapter 2

Theoretical background

In this chapter, we provide a concise overview of the fundamental principles in classical optics. We begin by presenting ray transfer matrices, which describe elementary optical transformations including free propagation and thin lenses. Moving on, we delve into the derivation of the paraxial wave equation from Maxwell's equations and explore its solutions. Next, we introduce an algorithm for free space propagation based on the Huygens-Fresnel diffraction principle. We outline the concept of a thin lens as a phase transformation. Additionally, we explore the Wigner distribution function, variance matrix, uncertainty principle and OAM associated with a paraxial light field. We then discuss the notion of partial coherence for both scalar and vector light fields. A generalized uncertainty principle suited for the polarization-spatial degrees of freedom is obtained. Finally, we introduce the concept of entanglement between different degrees of freedom of a paraxial light field.

2.1 Ray optics

The ray optics is likely the most straightforward theory that can adequately describe the various phenomena of light in daily life. As light rays travel through two different media with different refractive indices, three distinct optical phenomena can occur: reflection, refraction, and transmission. These phenomena can be inferred as a result of Fermat's principle, which states that the optical path length of an actual ray between any two points is shorter than the optical length of any other curve that joins the two points [70]

Let us consider the phenomenon of reflection of light at a surface as shown in Fig. 2.1. Light ray from point A strikes the mirror MM$'$ and then gets reflected to point C. Let us assume the point where the light ray strikes the mirror to be B$'$. According to Fermat's principle the optical path length traversed by the ray, i.e., n(AB$'$+B$'$C) should be minimum, where n is the refractive index of the medium. Consider a point A$'$ which is a mirror image

of the point A, such that AR = RA′ and consequently AB′ = A′B′. Thus, n(AB′ + B′C) = n(A′B′ + B′C), and for n(A′B′ + B′C) to be minimum all three points should lie on the straight line A′C. Consequently B′ coincides with B, i.e., by Fermat's principle a light ray traveling from A to C through mirror MM′ has the point of reflection at the interface to be at B. Laws of reflection states that the angle of incidence (∠ABN) and the angle of reflection (∠NBC) must be equal, and that the incident ray (AB), reflected ray (BC), and the normal to the surface at the point of incidence (BN) must lie on the same plane.

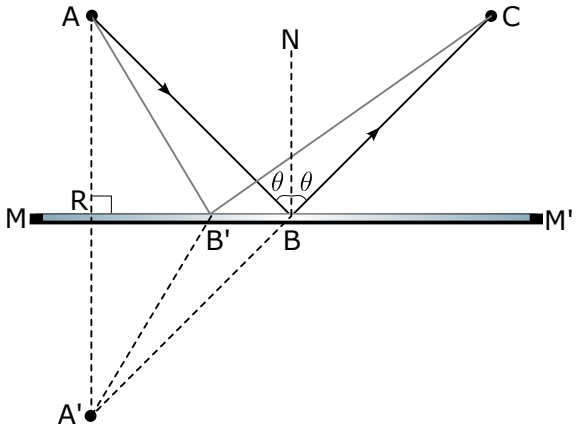

Figure 2.1: Reflection of light from a plane mirror MM′.

Let us now consider the phenomenon of refraction of light through a two-medium system of refractive indices n_1 and n_2 as shown in Fig. 2.2. Line PQ denotes the interface between the two mediums. Light ray from point A in medium 1 strikes the interface PQ at point B and then refract to point C in medium 2. In order to obtain the minimum optical path length from A to C (L_{op}), we draw perpendiculars AM (= h_1) and CN (= h_2). From Fig. 2.2, we have the optical path length from A to C as

$$L_{\text{op}} = n_1\text{AB} + n_2\text{BC} = n_1\sqrt{x^2 + h_1^2} + n_2\sqrt{(L-x)^2 + h_2^2}\,, \tag{2.1}$$

where x =MB, L =MN. To minimize L_{op} we must have $\frac{dL_{\text{op}}}{dx} = 0$, which in turn implies

$$\frac{2n_1 x}{\sqrt{x^2 + h_1^2}} - \frac{2n_2(L-x)}{\sqrt{(L-x)^2 + h_2^2}} = 0. \tag{2.2}$$

Equivalently, we have

$$n_1 \sin\theta_i = n_2 \sin\theta_r, \tag{2.3}$$

which is the Snell's law of refraction.

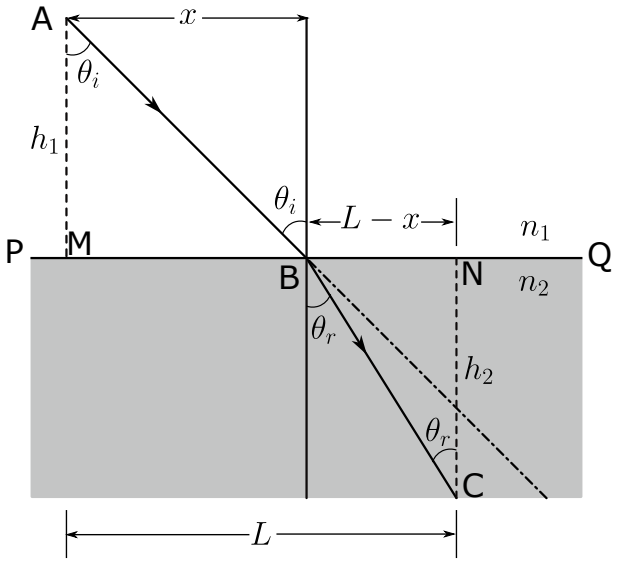

Figure 2.2: Refraction of light through a two-medium system of refractive indices n_1 and n_2.

2.1.1 Ray transfer matrices

Ray transfer matrices (ABCD matrices) are used to describe the propagation of paraxial rays through optical systems consisting of various optical transformations [71, 72]. These matrices also describe the propagation of Gaussian light fields through such optical systems. Let us assume the z-axis to be the optical axis of the system. A light ray is characterized by the distances from the optical axis in x and y coordinates, and by the angles made by the ray with x-z and y-z planes. In the case of symmetric first-order optical systems, such as free propagation and thin lens, the ray transforms symmetrically in x-z and y-z planes. A thin cylindrical lens is an example for an asymmetric first-order optical system. Let us first consider symmetric first-order optical systems.

Consider a light ray as shown in Fig. 2.3, where the z-axis is chosen as the optical axis. As light ray in a given transverse plane ($z =$ constant) of an optical system is characterized by the displacement x from the optical axis as well as the angle or slope x' with respect to the optical axis. For paraxial rays the angle x' is assumed to be small. On passage of a paraxial ray through an optical system, the parameters x_2 and x_2' of the outgoing light field is found to be linearly dependent on the parameters x_1 and x_1' of the incoming light field,

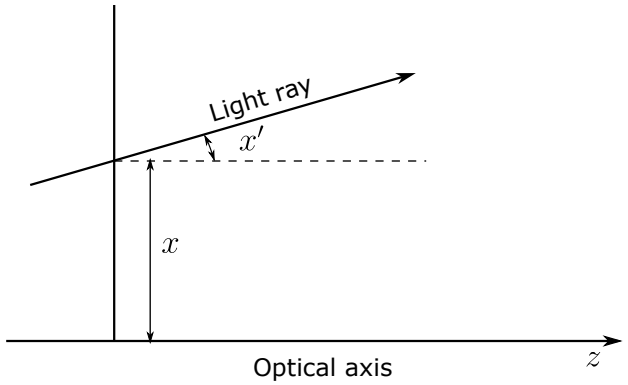

Figure 2.3: Light ray.

and the relation can be written in the matrix form as

$$\begin{bmatrix} x_2 \\ x_2' \end{bmatrix} = \begin{bmatrix} A & B \\ C & D \end{bmatrix} \begin{bmatrix} x_1 \\ x_1' \end{bmatrix}. \tag{2.4}$$

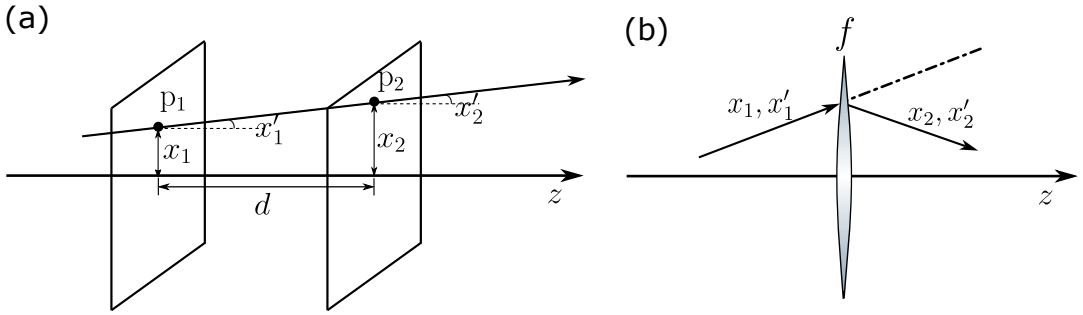

Figure 2.4: (a) Free propagation through a distance d. (b) Thin lens of focal length f.

The ray transfer matrix $\mathcal{F}(d)$ corresponding to free propagation through a distance d [see Fig. 2.4 (a)] in the x-z plane is given by

$$\mathcal{F}(d) = \begin{bmatrix} 1 & d \\ 0 & 1 \end{bmatrix}. \tag{2.5}$$

Similarly, the ray transfer matrix $\mathcal{L}(f)$ corresponding to a thin lens of focal length f [see

Fig. 2.4 (b)] in the x-z plane is given by

$$\mathcal{L}(f) = \begin{bmatrix} 1 & 0 \\ \frac{-1}{f} & 1 \end{bmatrix}. \tag{2.6}$$

Since both free propagation and thin lens are symmetric first-order optical systems the light ray transforms the same way in the y-z plane. Thus, the ray transfer matrices of free propagation by distance d, i.e., $\mathbf{F}(d)$, and thin lens of focal length f, i.e., $\mathbf{L}(f)$ are given by

$$\begin{bmatrix} \mathrm{x}_2 \\ \mathrm{y}_2 \end{bmatrix} = \mathbf{F}(d) \begin{bmatrix} \mathrm{x}_1 \\ \mathrm{y}_1 \end{bmatrix}, \text{ where } \mathbf{F}(d) = \begin{bmatrix} \mathcal{F}(d) & \mathbb{0} \\ \mathbb{0} & \mathcal{F}(d) \end{bmatrix}, \text{ and} \tag{2.7}$$

$$\begin{bmatrix} \mathrm{x}_2 \\ \mathrm{y}_2 \end{bmatrix} = \mathbf{L}(f) \begin{bmatrix} \mathrm{x}_1 \\ \mathrm{y}_1 \end{bmatrix}, \text{ where } \mathbf{L}(f) = \begin{bmatrix} \mathcal{L}(f) & \mathbb{0} \\ \mathbb{0} & \mathcal{L}(f) \end{bmatrix}. \tag{2.8}$$

Here, $\mathrm{x}_j = [x_j, x_j']^{\mathrm{T}}$ and $\mathrm{y}_j = [y_j, y_j']^{\mathrm{T}}$ with $j = 1, 2$, and $\mathbb{0}$ denotes a 2×2 zero matrix. The superscript T denotes matrix transpose. On passage through asymmetric first-order optical systems the light ray transforms differently in the x-z plane and the y-z plane. For instance consider a thin cylindrical lens of focal length f as shown in Fig. 2.5, having curvature in the x-direction. This has the same effect as a thin lens of focal length f in the x-z plane and has no effect in the y–z plane, i.e.,

$$\begin{bmatrix} \mathrm{x}_2 \\ \mathrm{y}_2 \end{bmatrix} = \mathbf{L}_x(f) \begin{bmatrix} \mathrm{x}_1 \\ \mathrm{y}_1 \end{bmatrix}, \text{where } \mathbf{L}_x(f) = \begin{bmatrix} \mathcal{L}(f) & \mathbf{0} \\ \mathbf{0} & \mathbb{1} \end{bmatrix}. \tag{2.9}$$

Here $\mathbf{L}_x(f)$ is the ray transfer matrix corresponding to the thin cylindrical lens having curvature along the x-direction and $\mathbb{1}$ denotes 2×2 identity matrix. Note that a thin cylin-

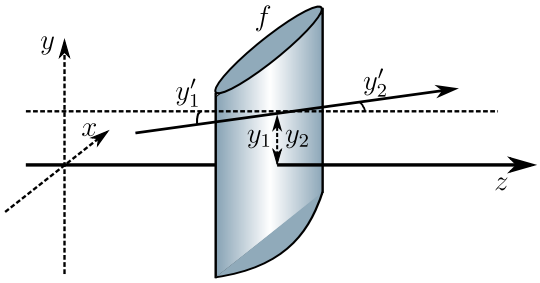

Figure 2.5: Thin cylindrical lens of focal length f, having curvature in the x-direction.

drical lens of focal length f having curvature along the y-direction has the ray transfer

matrix given by

$$\mathbf{L}_y(f) = \begin{bmatrix} \mathbb{1} & \mathbf{0} \\ \mathbf{0} & \mathcal{L}(f) \end{bmatrix}. \tag{2.10}$$

Now that we have discussed the ray transfer matrices corresponding to various optical transformations such as free propagation and thin lens, we move on to obtaining these transformations using wave optics in the paraxial limit.

2.2 Wave optics

Wave optics is a branch of physics that deals with the study of light as a wave phenomenon. It focuses on understanding and analyzing the behaviour of light waves, including phenomena such as interference, diffraction, polarization, and dispersion. In wave optics, light is considered as an electromagnetic wave that propagates through space. This wave nature of light is described by Maxwell's equations, which govern the behaviour of electromagnetic fields. These equations relate the electric and magnetic fields to each other and describe how they propagate and interact with matter.

2.2.1 Maxwell's Equations

Maxwell's equations are a set of fundamental equations that describe the behaviour of electric and magnetic fields in classical electromagnetism. They were formulated by the Scottish physicist James Clerk Maxwell in the 19$^{\text{th}}$ century and played a crucial role in unifying the previously separate theories of electricity and magnetism. Maxwell's equations in free space (in regions where electrostatic charges and current are absent) [73], can be written as follows:

$$\nabla \cdot \mathbf{E} = 0, \tag{2.11}$$

$$\nabla \cdot \mathbf{B} = 0, \tag{2.12}$$

$$\nabla \times \mathbf{E} = -\frac{\partial \mathbf{B}}{\partial t}, \text{ and} \tag{2.13}$$

$$\nabla \times \mathbf{B} = \mu_0 \epsilon_0 \frac{\partial \mathbf{E}}{\partial t}, \tag{2.14}$$

where $\nabla = \hat{i}\frac{\partial}{\partial x} + \hat{j}\frac{\partial}{\partial y} + \hat{k}\frac{\partial}{\partial z}$, $\mathbf{E}$ is the electric field (with units kg m s^{-2} C^{-1}), $\mathbf{B}$ is magnetic field (with units kg s^{-2} A^{-1}), ϵ_0 is permittivity of free space (8.85×10^{-12} m^{-3} kg^{-1} s^4 A^2),

μ_0 is permeability of free space ($4\pi \times 10^{-7}$ m kg s^2 A^{-2}), and t is time (with units s).

2.2.2 Wave equation in free space

The wave equation in free space describes the behaviour of a wave propagating through a medium where there are no external forces or sources. It can be readily obtained from Maxwell's equations using vector calculus identities [74]. Applying curl operation on both sides of Eq. (2.13), and then using Eqs. (2.11) and (2.14), we obtain

$$\begin{aligned} \nabla \times (\nabla \times \mathbf{E}) &= -\frac{\partial}{\partial t}(\nabla \times \mathbf{B}) \\ \nabla(\nabla \cdot \mathbf{E}) - \nabla^2 \mathbf{E} &= -\mu_0 \epsilon_0 \frac{\partial^2 \mathbf{E}}{\partial t^2} \\ \nabla^2 \mathbf{E} &= \mu_0 \epsilon_0 \frac{\partial^2 \mathbf{E}}{\partial t^2}. \end{aligned} \tag{2.15}$$

Similarly, applying curl operation on both sides of Eq. (2.14), and then using Eqs. (2.12) and (2.13), we obtain

$$\begin{aligned} \nabla \times (\nabla \times \mathbf{B}) &= \mu_0 \epsilon_0 \frac{\partial}{\partial t}(\nabla \times \mathbf{E}) \\ \nabla(\nabla \cdot \mathbf{B}) - \nabla^2 \mathbf{B} &= -\mu_0 \epsilon_0 \frac{\partial^2 \mathbf{B}}{\partial t^2} \\ \nabla^2 \mathbf{B} &= \mu_0 \epsilon_0 \frac{\partial^2 \mathbf{B}}{\partial t^2}. \end{aligned} \tag{2.16}$$

We have the velocity of light $c = \frac{1}{\sqrt{\mu_0 \epsilon_0}} = 3 \times 10^8$ ms^{-1}, and thus the electric and magnetic fields $\mathbf{E}$ and $\mathbf{B}$ satisfy the partial differential equation

$$\nabla^2 \varphi = \frac{1}{c^2} \frac{\partial^2 \varphi}{\partial t^2}, \tag{2.17}$$

where φ is a scalar function of space-time variables. Note that Eq. (2.17) is the three-dimensional wave equation.

2.2.3 Paraxial wave equation

The paraxial wave equation can be derived by making specific assumptions about the wave behaviour. It assumes that the wave is slowly varying in space and that the angles of propagation are small, allowing for linear approximations. The paraxial wave equation is typically derived from the more general wave equation by neglecting higher-order terms.

Let us assume the scalar function φ in Eq. (2.17) is separable in space and time, that is,

$$\varphi(x, y, z, t) = \varphi_s(x, y, z)\varphi_t(t). \tag{2.18}$$

Here φ_s and φ_t denote functions purely in space and time respectively. From Eqs. (2.17) and (2.18), we have

$$\frac{1}{\varphi_s}\nabla^2\varphi_s = \frac{1}{c^2}\frac{1}{\phi_t}\frac{d^2\varphi_t}{dt^2}. \tag{2.19}$$

The left-hand side (LHS) and right-hand side (RHS) of the above equation is purely a function of space and time respectively, and can be equated to some constant, say κ^2. Thus we obtain

$$\nabla^2\varphi_s = -\kappa^2\varphi_s, \text{ and} \tag{2.20}$$

$$\frac{d^2\varphi_t}{dt^2} = -\omega^2\varphi_t. \tag{2.21}$$

Here, Eq. (2.20) is known as Helmholtz's equation and $\omega = \kappa c$. Note that for a monochromatic source ($\kappa = 2\pi/\lambda$ with λ being the wavelength) the solution to Eq. (2.21) is given by

$$\varphi_t(t) = \exp(-i\omega t). \tag{2.22}$$

Assuming $\varphi_s(x, y, z)$ of Eq. (2.20) travels along the z-axis, we have [69]

$$\varphi_s(x, y, z) \approx \psi(x, y; z)\exp(i\kappa z), \tag{2.23}$$

where $\psi(x, y; z)$ slowly varies with respect to z. On substituting Eq. (2.23) in Eq. (2.20) we obtain

$$\left(\frac{\partial^2}{\partial x^2} + \frac{\partial^2}{\partial y^2} + \frac{\partial^2}{\partial z^2}\right)\psi\exp(i\kappa z) = -\kappa^2\psi\exp(i\kappa z). \tag{2.24}$$

We have

$$\begin{aligned}\frac{\partial^2(\psi \mathrm{e}^{i\kappa z})}{\partial z^2} &= \left(\frac{\partial^2\psi}{\partial z^2} + 2i\kappa\frac{\partial\psi}{\partial z} - \kappa^2\psi\right)\mathrm{e}^{i\kappa z} \\ &\approx \left(2i\kappa\frac{\partial\psi}{\partial z} - \kappa^2\psi\right)\mathrm{e}^{i\kappa z},\end{aligned} \tag{2.25}$$

since under paraxial approximation $\frac{\partial^2\psi}{\partial z^2} \approx 0$. Equation (2.24) can now be rewritten as

$$\frac{\partial^2\psi}{\partial x^2} + \frac{\partial^2\psi}{\partial y^2} + 2i\kappa\frac{\partial\psi}{\partial z} = 0, \tag{2.26}$$

which is nothing but the well known paraxial Helmholtz equation, or more commonly known as the paraxial wave equation [69, 72].

2.2.4 Solutions to the paraxial wave equation

The paraxial wave equation describes the propagation of a wave in the paraxial approximation, where the angles of propagation are small. Paraxial light fields are solutions to the paraxial wave equation given in Eq. (2.26). Hermite Gaussian (HG) modes and Laguerre Gaussian (LG) modes are examples of such solutions. HG modes are solutions to the paraxial wave equation that have complex intensity distributions characterized by the Hermite polynomials. These light fields exhibit distinct spatial patterns along the transverse direction and are given by [72, 75]

$$\varphi_{m_1m_2}(x,y;z) = \psi_{m_1m_2}(x,y;z)\exp[i\phi(x,y;z)], \text{ with} \tag{2.27}$$

$$\psi_{m_1m_2}(x,y;z) = \psi_{m_1}(x;z)\psi_{m_2}(y;z), \text{ and} \tag{2.28}$$

$$\phi(x,y;z) = -\frac{(x^2+y^2)\kappa}{2R_z} - (m_1+m_2+1)\zeta_z, \text{ where} \tag{2.29}$$

$$\psi_{m_1}(x;z) = \left(\frac{2}{\pi}\right)^{\frac{1}{4}}\left(\frac{1}{2^{m1}m_1!w_z}\right)^{\frac{1}{2}} H_{m_1}\left(\frac{\sqrt{2}x}{w_z}\right)\exp\left(-\frac{x^2}{w_z^2}\right). \tag{2.30}$$

Here, $\psi_{m2}(y;z)$ is the same as $\psi_{m1}(x;z)$ with x and m_1 replaced with y and m_2, $H_{m_1}(\cdot)$ is the Hermite polynomial of order m_1 with m_1, m_2 taking integer values ≥ 0, z is the distance of propagation from the waist plane, w_z is the width of the light field at a given z, R_z is the radius of curvature at a given z, $(m_1+m_2+1)\zeta_z$ is the Gouy phase picked by the light field on propagation [71], $\zeta_z = \tan^{-1}(z/z_r)$, Rayleigh range $z_r = \kappa w_0^2/2$, and w_0 is the width of the light field at $z = 0$. The width w_z and the radius of curvature R_z of the light field is given by

$$w_z^2 = w_0^2\left(1+\frac{z^2}{z_r^2}\right), \text{ and} \tag{2.31}$$

$$R_z = z\left(1+\frac{z_r^2}{z^2}\right). \tag{2.32}$$

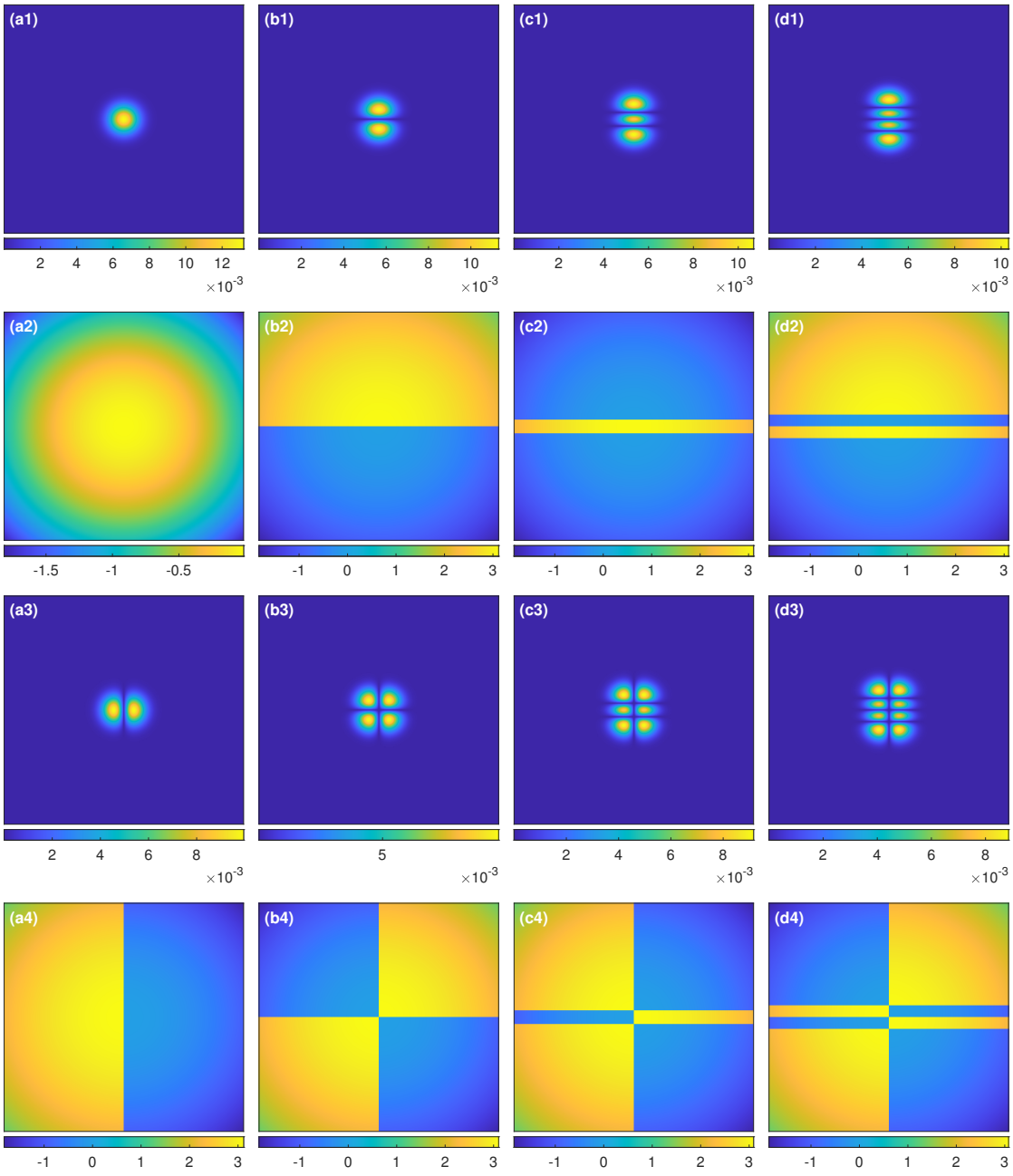

Figure 2.6: The amplitude and phase profiles of some HG modes [see Eq. (2.27)]. The first row depicts the amplitude profiles of HG modes with $m_1 = 0$ and $m_2 = 0, 1, 2, 3$. The corresponding phase profiles are provided in the second row. Similarly, the third row depicts the amplitude profiles of HG modes with $m_1 = 1$ and $m_2 = 0, 1, 2, 3$. The corresponding phase profiles are provided in the fourth row.

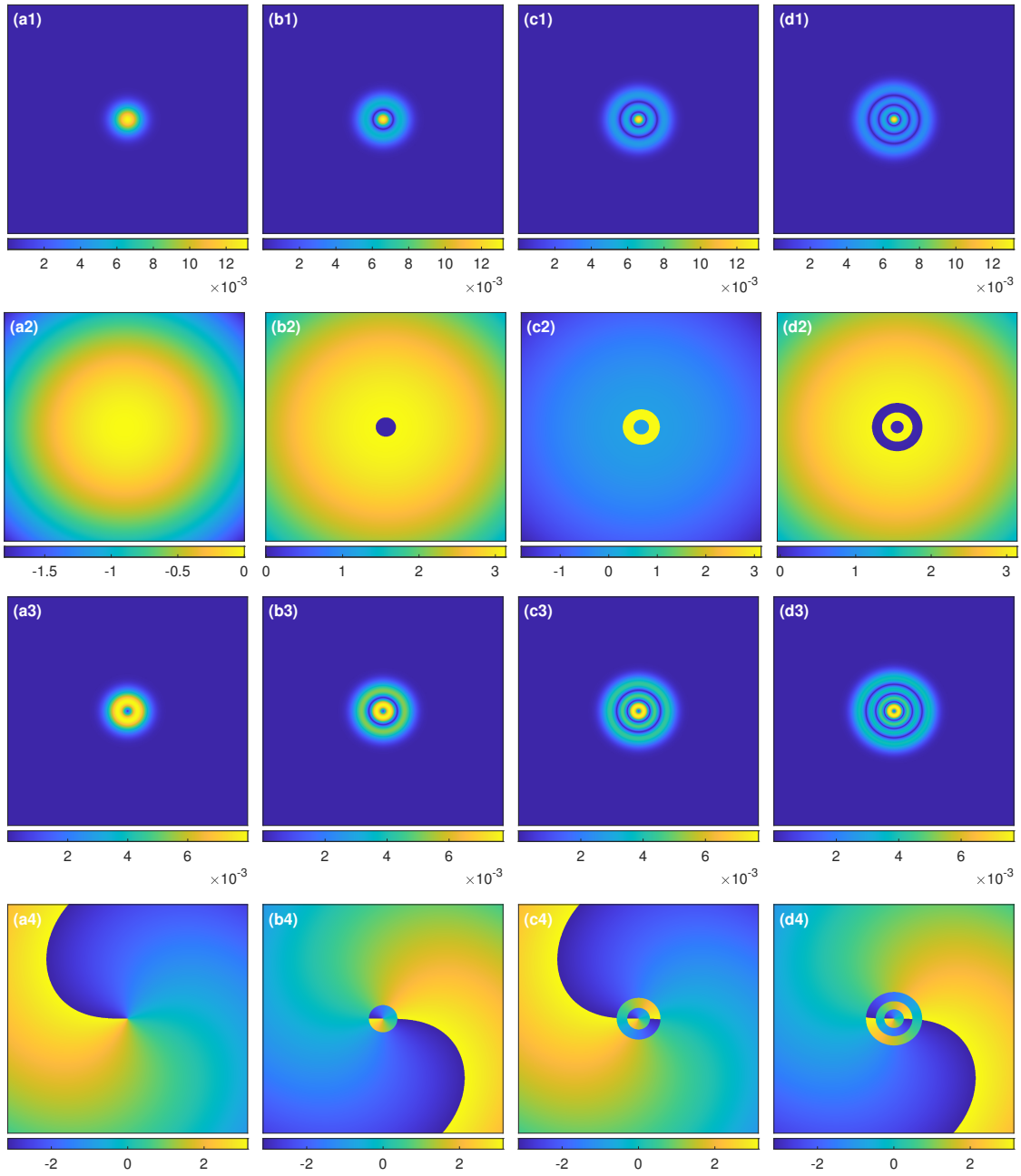

Figure 2.7: The amplitude and phase profiles of some LG modes [see Eq. (2.33)]. The first row depicts the amplitude profiles of LG modes with $j = 0, 1, 2, 3$ and $m = 0$. The corresponding phase profiles are provided in the second row. Similarly, the third row depicts the amplitude profiles of LG modes with $j = 0.5, 1.5, 2.5, 3.5$ and $m = 0.5$. The corresponding phase profiles are provided in the fourth row.

LG modes are solutions to the paraxial wave equation that have azimuthal variations characterized by the Laguerre polynomials. They exhibit a characteristic doughnut-shaped

intensity profile with a dark central spot. An LG mode labeled by radial and azimuthal indices j and m, respectively, can be written in the radial coordinates $r = \sqrt{x^2 + y^2}$ and $\theta = \tan^{-1}(y/x)$, at a particular z, as [72, 76, 77]

$$\psi_{jm}(r, \theta; z) = \sqrt{\frac{2}{\pi w_z^2}} \left[\frac{(j - |m|)!}{(j + |m|)!}\right]^{\frac{1}{2}} \left[\frac{\sqrt{2}r}{w_z}\right]^{2|m|} L_{j-|m|}^{2|m|}\left(\frac{2r^2}{w_z^2}\right) \times \exp\left[-\frac{r^2}{w_z^2}\right] \exp\left[i\phi_{jm}(r, \theta; z)\right], \text{ where} \tag{2.33}$$

$$\phi_{jm}(r, \theta; z) = -\frac{\kappa r^2}{2R_z} + 2m\theta - (2j + 1)\zeta_z. \tag{2.34}$$

Here, $L_{j-|m|}^{2|m|}(\cdot)$ is the Laguerre polynomial. Note that the radial index j can take half integer values, i.e., $0, \frac{1}{2}, 1, ...$, and azimuthal index m can take values $-j, -(j-1), ...j$ for a given j. The LG mode given by Eq. (2.33) can also be denoted as $\psi_{lp}(r, \theta; z)$, where the azimuthal and radial indices l and p can take purely integer values [72], with $l = 2m$, and $p = j - |m|$.

2.3 Huygens-Fresnel diffraction principle and Fresnel approximation for free space propagation

This section is devoted to the development of an algorithm for free space propagation, as outlined in [69]. The Huygens-Fresnel diffraction principle is a fundamental concept in diffraction theory that provides a method for understanding how waves propagate and interact with obstacles or apertures. It is named after Dutch physicist Christiaan Huygens and French physicist Augustin-Jean Fresnel, who made significant contributions to the development of this principle. According to this principle, when a wave encounters an obstacle or passes through an aperture, each point on the wavefront acts as a source of secondary wavelets. These wavelets interfere with each other, leading to constructive and destructive interference patterns that determine the resulting wavefront shape beyond the obstacle or aperture.

The diffraction geometry for free space propagation is as shown in Fig. 2.8, where the diffracting aperture lies in the transverse coordinates (x', y') and is illuminated in positive z direction. The light field is calculated across the observation plane defined by the transverse coordinates (x, y). The z-axis is normal to both the aperture plane as well as the observation plane.

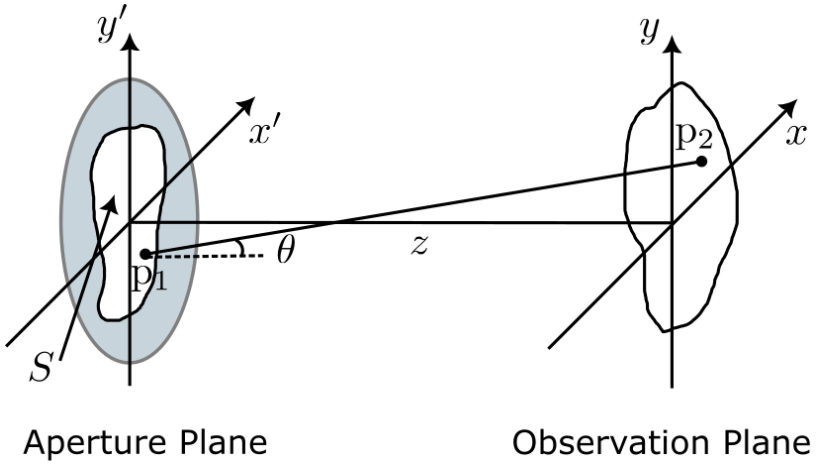

Figure 2.8: Diffraction geometry for free space propagation.

The Huygens-Fresnel principle can be stated as

$$\psi(\mathrm{p}_0) = \frac{1}{i\lambda} \int\int_S \psi(\mathrm{p}_1) \frac{\mathrm{e}^{i\kappa r_{01}}}{r_{01}} \cos\theta \, ds, \tag{2.35}$$

where $\psi(\mathrm{p}_1)$ is the field at point p_1 on the aperture plane, $\psi(\mathrm{p}_0)$ is the field at point p_0 on the observation plane, and θ is the angle between the outward normal and the vector $\vec{r}_{01}$ pointing from p_0 to p_1. The aperture plane surface S is illuminated by the light field.

Substituting $\cos\theta = z/r_{01}$, Eq. (2.35) can be rewritten as

$$\psi(x,y) = \frac{z}{i\lambda} \int\int_S \psi(x',y') \frac{\mathrm{e}^{i\kappa r_{01}}}{r_{01}^2} \, dx'dy', \tag{2.36}$$

where the distance r_{01} is given by $r_{01} = \sqrt{z^2 + (x-x')^2 + (y-y')^2}$. On binomial approximation, when the distance $z >> (x-x')^2 + (y-y')^2$,

$$r_{01} \approx z \left[1 + \frac{1}{2} \left(\frac{x-x'}{z} \right)^2 + \frac{1}{2} \left(\frac{y-y'}{z} \right)^2 \right]. \tag{2.37}$$

Applying the binomial approximation only in the exponential part, we get

$$\psi(x,y) = \frac{\mathrm{e}^{i\kappa z}}{i\lambda z} \int\int_{-\infty}^{\infty} \psi(x',y') \exp\left\{ \frac{i\kappa}{2z} \left[(x-x')^2 + (y-y')^2 \right] \right\} dx'dy'. \tag{2.38}$$

The convolution form of the above equation is given as

$$\psi(x,y) = \int\int_{-\infty}^{\infty} \psi(x',y')h(x-x',y-y')dx'dy', \tag{2.39}$$

where the convolution kernel is given by

$$h(x,y) = \frac{\mathrm{e}^{i\kappa z}}{i\lambda z}\exp\left[\frac{i\kappa}{2z}(x^2+y^2)\right]. \tag{2.40}$$

The integral given by Eq. (2.38) is known as the Fresnel diffraction integral. Here we remark that while Eq. (2.7) is the ray optic version of free propagation, Eq. (2.38) is the wave optic version of the same.

The diffraction integral can also be realized by taking the Fourier transform of the product of the complex field just to the right of the aperture and a quadratic phase exponential. Thus, the propagated field $\psi(x,y;z)$ can be written in terms of $\psi(x,y;0)$ and the Huygens-Fresnel kernel $h(x,y)$ as :

$$\psi(x,y;z) = \psi(x,y;0) * h(x,y), \tag{2.41}$$

$$F\{\psi(x,y;z)\} = F\{\psi(x,y;0)\} \times H(\mathrm{f}_x,\mathrm{f}_y), \tag{2.42}$$

$$\psi(x,y;z) = F^{-1}[F\{\psi(x,y;0)\} \times H(\mathrm{f}_x,\mathrm{f}_y)], \tag{2.43}$$

where $F\{\cdot\}$ and $F^{-1}\{\cdot\}$ stand for the Fourier and inverse Fourier transformations, f_x and f_y are the spatial frequency components along x- and y-directions, and $H(\mathrm{f}_x,\mathrm{f}_y)$ is the Fourier transform of Huygens-Fresnel kernel given by

$$H(\mathrm{f}_x,\mathrm{f}_y) = F\{h(x,y)\} = \mathrm{e}^{i\kappa z}\exp[-i\pi\lambda z(\mathrm{f}_x^2+\mathrm{f}_y^2)]. \tag{2.44}$$

2.4 Thin lens as a phase transformation

A lens is typically made of an optically dense material, such as glass, with a refractive index around 1.5. This material exhibits a slower propagation velocity for optical disturbances compared to air. When a ray enters a thin lens at coordinates (x,y) on one face, it approximately exits at the same coordinates on the opposite face, indicating minimal displacement of the ray within the lens. As a result, a thin lens primarily introduces a delay in the incident wavefront that is proportionate to the thickness of the lens at each point.

Let the thickness of the lens at its axis, i.e., the maximum thickness of the lens, be

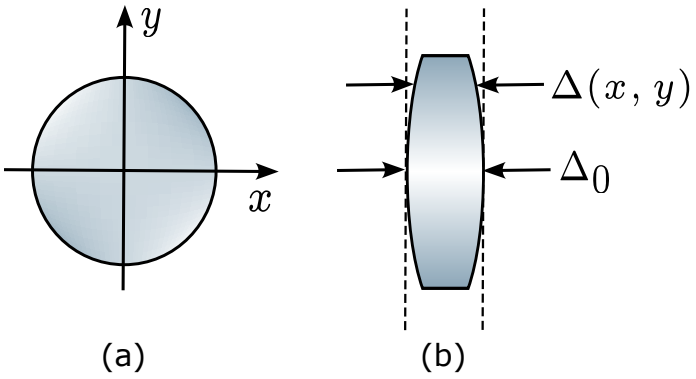

Figure 2.9: (a) Front view of the lens, (b) side view of the lens.

denoted as Δ_0, and the thickness at coordinates (x, y) be denoted as $\Delta(x, y)$ (see Fig. 2.9). The total phase delay suffered by the light field at coordinates (x, y) on passage through the lens can be written as

$$\phi(x, y) = \kappa n \Delta(x, y) + \kappa[\Delta_0 - \Delta(x, y)], \tag{2.45}$$

where n is the refractive index of the lens material. From Fig. 2.9 it is clear that, $\kappa n \Delta(x, y)$ is the phase delay introduced by the lens, and $\kappa[\Delta_0 - \Delta(x, y)]$ is the phase delay introduced by the remaining region of free space between the two planes. Phase transformation due to the thin lens is of the form [69]

$$\mathcal{L}_f(x, y) = \exp(i\kappa\Delta_0) \exp[i\kappa(n-1)\Delta(x, y)]. \tag{2.46}$$

The paraxial light field $\psi'(x, y)$ at the exit plane is related to the paraxial light field $\psi(x, y)$ at the entry plane as

$$\psi'(x, y) = \mathcal{L}_f(x, y)\psi(x, y). \tag{2.47}$$

The lens can be assumed to be made up of three parts as shown in Fig. 2.10. Thus, the thickness function $\Delta(x, y)$ can be written as

$$\begin{aligned}\Delta(x, y) &= \Delta_{01} - \left(R_1 - \sqrt{R_1^2 - x^2 - y^2}\right) + \Delta_{02} + \Delta_{03} - \left(R_2 - \sqrt{R_2^2 - x^2 - y^2}\right) \\ &= \Delta_0 - R_1\left(1 - \sqrt{1 - \frac{x^2 + y^2}{R_1^2}}\right) - R_2\left(1 - \sqrt{1 - \frac{x^2 + y^2}{R_2^2}}\right),\end{aligned} \tag{2.48}$$

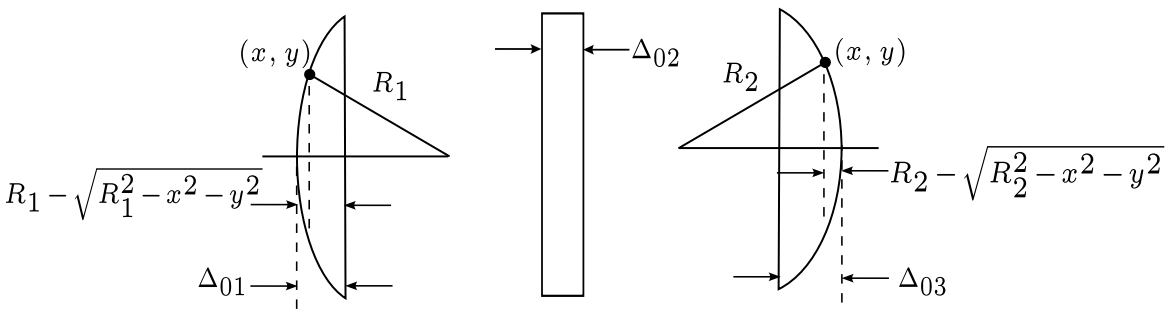

Figure 2.10: Side view of the lens in (b) of Fig. 2.9 is split into two curved parts and one flat part as shown here, in order to calculate the thickness function $\Delta(x, y)$.

where $\Delta_0 = \Delta_{01} + \Delta_{02} + \Delta_{03}$. On paraxial approximation

$$\sqrt{1 - \frac{x^2 + y^2}{R_1^2}} \approx 1 - \frac{x^2 + y^2}{2R_1^2}, \text{ and} \tag{2.49}$$

$$\sqrt{1 - \frac{x^2 + y^2}{R_2^2}} \approx 1 - \frac{x^2 + y^2}{2R_2^2}. \tag{2.50}$$

Thus, we have

$$\Delta(x, y) = \Delta_0 - \frac{x^2 + y^2}{2}\left(\frac{1}{R_1} + \frac{1}{R_2}\right). \tag{2.51}$$

On substituting Eq. (2.51) in Eq. (2.46) we obtain

$$\begin{aligned}\mathcal{L}_f(x, y) &= \exp(i\kappa n\Delta_0) \exp\left[-i\kappa(n-1)\frac{x^2 + y^2}{2}\left(\frac{1}{R_1} + \frac{1}{R_2}\right)\right] \\ &= \exp(i\kappa n\Delta_0) \exp\left[-\frac{i\kappa}{2f}(x^2 + y^2)\right].\end{aligned} \tag{2.52}$$

Here the focal length of the lens f is given by

$$\frac{1}{f} \equiv (n-1)\left(\frac{1}{R_1} + \frac{1}{R_2}\right). \tag{2.53}$$

Neglecting the constant phase factor, the phase transformation due to lens can be rewritten as

$$\mathcal{L}_f(x, y) = \exp\left[-\frac{i\kappa}{2f}(x^2 + y^2)\right]. \tag{2.54}$$

Here we remark that while Eq. (2.8) is the ray optic version of thin lens transformation, Eq. (2.54) is the wave optic version of the same.

2.5 Unitary representation of linear canonical transformations

Under the action of a paraxial unitary transformation $\hat{\mathbf{U}}$ generated by the most general quadratic in the operators $\hat{x}, \hat{p}_x, \hat{y}$, and $\hat{p_y}$ (first-order optical system) [78], a paraxial light field $\psi(x, y; z)$ transforms as

$$\psi(x, y; z) \longrightarrow \hat{\mathbf{U}}\psi(x, y; z). \tag{2.55}$$

As seen from Refs. [78, 79], the unitary transformation $\hat{\mathbf{U}}$ is in correspondence with a symplectic matrix $\mathbf{S} \in Sp(4, \mathbb{R})$, i.e., $\hat{\mathbf{U}} \equiv \hat{\mathbf{U}}(\mathbf{S})$. For instance, let $\hat{\boldsymbol{\xi}} = [\hat{x}, \hat{p}_x, \hat{y}, \hat{p}_y]^{\mathsf{T}}$, then

$$\hat{\mathbf{U}}^{\dagger}(\mathbf{S})\hat{\boldsymbol{\xi}}\hat{\mathbf{U}}(\mathbf{S}) = \mathbf{S}\hat{\boldsymbol{\xi}}, \text{ where} \tag{2.56}$$

$$\mathbf{S}\Sigma\mathbf{S}^{\mathsf{T}} = \Sigma, \text{ with } \Sigma = \Omega \oplus \Omega, \text{ and} \tag{2.57}$$

$$\Omega = \begin{bmatrix} 0 & 1 \\ -1 & 0 \end{bmatrix}. \tag{2.58}$$

In other words, $\mathbf{S}$ is a linear canonical transformation [80]. We have, $\hat{x} = x$, $\hat{y} = y$, $\hat{p}_x = -\frac{i}{\kappa}\frac{\partial}{\partial x}$, and $\hat{p}_y = -\frac{i}{\kappa}\frac{\partial}{\partial y}$ in the position representation [81]. The definition for momentum operator is identical to the quantum mechanical definition wherein the wavelength λ is replaced with the Planck's constant h.

Let us now consider two different examples of unitary transformations: free propagation by distance d, and thin lens of focal length f . First, we have the free propagation unitary given by

$$\mathcal{F}_d = \exp\left[\frac{-id\kappa}{2}(\hat{p}_x^2 + \hat{p}_y^2)\right]. \tag{2.59}$$

If $\hat{\mathbf{U}} = \mathcal{F}_d$, then Eq. (2.56) can be written as

$$\mathcal{F}_d^{\dagger}\hat{\boldsymbol{\xi}}\mathcal{F}_d = \mathbf{F}(d)\hat{\boldsymbol{\xi}}, \tag{2.60}$$

where $\mathbf{F}(d)$ is the ray transfer matrix corresponding to free propagation by distance d [see

Eq. (2.7)]. Next, we have the unitary operator $\mathcal{L}_f$ corresponding to thin lens of focal length f, given by

$$\mathcal{L}_f = \exp\left[-\frac{i\kappa}{2f}(\hat{x}^2+\hat{y}^2)\right] \equiv \mathcal{L}_f^x \otimes \mathcal{L}_f^y, \tag{2.61}$$

where $\mathcal{L}_f^x$ and $\mathcal{L}_f^y$ act on operators $[\hat{x},\hat{p}_x]^{\mathrm{T}}$ and $[\hat{y},\hat{p}_y]^{\mathrm{T}}$ alone. If $\hat{\mathbf{U}} = \mathcal{L}_f$, then

$$\mathcal{L}_f^\dagger \hat{\boldsymbol{\xi}} \mathcal{L}_f = \mathbf{L}(f)\hat{\boldsymbol{\xi}}, \tag{2.62}$$

where $\mathbf{L}(f)$ is the ray transfer matrix corresponding to thin lens of focal length f [see Eq. (2.8)]. The unitary transformations $\mathcal{L}_f^x$ and $\mathcal{L}_f^y$ have their associated ray transfer matrices to be $\mathbf{L}_x(f)$ and $\mathbf{L}_y(f)$ corresponding to cylindrical lenses whose curvatures are in the x- and y-directions, respectively [see Eq. (2.9)].

Let us say the unitary transformation $\hat{\mathbf{U}}(\mathbf{S})$ acts identically on the operators $[\hat{x},\hat{p}_x]^{\mathrm{T}}$ and $[\hat{y},\hat{p}_y]^{\mathrm{T}}$. In that case, we have

$$\hat{\mathbf{U}}(\mathbf{S}) = \hat{U}_x(S) \otimes \hat{U}_y(S), \text{ and} \tag{2.63}$$

$$\mathbf{S} = S \oplus S, \tag{2.64}$$

where $\hat{U}_x(S)$ and $\hat{U}_y(S)$ are the most general quadratic in $\hat{x},\hat{p}_x$ and $\hat{y},\hat{p}_y$, respectively, with $S \in Sp(2,\mathbb{R})$. For instance, let $\hat{\xi} = [\hat{x},\hat{p}_x]^{\mathrm{T}}$, then

$$\hat{U}^\dagger(S)\,\hat{\xi}\,\hat{U}(S) = S\,\hat{\xi}, \text{ where} \tag{2.65}$$

$$S\,\Omega\,S^{\mathrm{T}} = \Omega, \tag{2.66}$$

and $\hat{U}(S) \equiv \hat{U}_x(S)$.

HG mode in a single variable at the waist plane, can be written as (see Section 2.2.4)

$$\psi_m(x) = \langle x|m\rangle = \left[\frac{1}{2^m m!}\sqrt{\frac{\mathrm{c}}{\pi}}\right]^{\frac{1}{2}} \exp\left[-\frac{\mathrm{c}x^2}{2}\right] H_m\left(x\sqrt{\mathrm{c}}\right). \tag{2.67}$$

Here $\mathrm{c} = \frac{2}{w_0^2}$, $|x\rangle$ is the eigenstate of the position operator $\hat{x}$, and $|m\rangle$ is the Fock state which represents the wave function $\psi_m(x)$. Under the action of a paraxial unitary transformation $\hat{U}$ generated by the most general quadratic in the operators $\hat{x}$ and $\hat{p}_x$, the HG mode $\langle x|m\rangle$ for instance, transforms as $\langle x|m\rangle \longrightarrow \langle x|\hat{U}|m\rangle$ [78].

Let us now move on to the situation when the unitary transformations include transla-

tions as well. That is,

$$\hat{\mathcal{U}} \equiv \hat{\mathcal{U}}(S, \mathbf{d}) = \hat{D}(\mathbf{d})\hat{U}(\mathbf{S}), \tag{2.68}$$

where $\hat{D}(\mathbf{d}) = \exp[i\delta_2\sqrt{\mathrm{c}}\hat{x} - \frac{i\kappa\delta_1}{\sqrt{\mathrm{c}}}\hat{p}_x]$ with $\mathbf{d} = \left[\frac{\delta_1}{\sqrt{\mathrm{c}}}, \frac{\delta_2\sqrt{\mathrm{c}}}{\kappa}\right]^{\mathrm{T}}$ is the displacement operator, and $\hat{U}(\cdot)$ is a unitary transformation generated by a quadratic Hamiltonian as in Eq. (2.65). We have

$$\hat{\mathcal{U}}^{\dagger}(S, \mathbf{d})\,\hat{\xi}\,\hat{\mathcal{U}}(S, \mathbf{d}) = S\,\hat{\xi} + \mathbf{d}. \tag{2.69}$$

Note that $\hat{U}(\mathbf{S}, \mathbf{d})$ is the most general Gaussianity preserving transformation on the spatial degree of freedom.

2.6 Wigner distribution function

A paraxial coherent light field propagating along the z-direction can be represented as

$$\varphi(x, y, z, t) = \psi(x, y; z)\exp[i(\kappa z - \omega t)], \text{ where} \tag{2.70}$$

$$\psi(x, y; z) = A(x, y; z)\exp[i\phi(x, y; z)], \tag{2.71}$$

with $A(x, y; z)$ being the amplitude, and $\phi(x, y; z)$ being the phase of the light field.

A system of lenses and free propagations is well represented by its ray transfer matrix [67, 82, 83], and there is a corresponding unitary transformation acting on the paraxial light field under its action [79, 84, 85]. This correspondence is well captured through the Wigner distribution function [86]. The Wigner distribution function of the paraxial coherent light field $\psi(x, y; z)$ in terms of transverse position $\mathbf{x} = (x, y)$ and transverse momentum $\mathbf{p} = (p_x, p_y)$ is defined as [79, 85–88]:

$$W(\boldsymbol{\xi}) \equiv W(\mathbf{x}, \mathbf{p}) = \left(\frac{\kappa}{\pi}\right)^2 \int_{-\infty}^{\infty}\int_{-\infty}^{\infty} \psi^*(\mathbf{x} - \mathbf{x}'; z)\,\psi(\mathbf{x} + \mathbf{x}'; z)\exp(-i2\kappa\mathbf{x}'.\mathbf{p})dx'dy', \tag{2.72}$$

where $\boldsymbol{\xi} = [x, p_x, y, p_y]^{\mathrm{T}}$. All information regarding $\psi(x, y; z)$ is contained in the Wigner distribution function $W(\boldsymbol{\xi})$. Under the action of a unitary transformation, corresponding to the ray transfer matrix $\mathbf{S}$, the resultant Wigner distribution function $W'(\boldsymbol{\xi})$ is related to the

input Wigner distribution function $W(\boldsymbol{\xi})$ as [79, 87] :

$$W'(\boldsymbol{\xi}) = W(\mathbf{S}^{-1}\boldsymbol{\xi}). \tag{2.73}$$

For instance, free propagation by distance d and thin lens of focal length f are two elementary unitary transformations realized on a coherent paraxial light field whose ray transfer matrices are given by $\mathbf{F}(d)$ and $\mathbf{L}(f)$ respectively [see Eqs. (2.7) and (2.8)]. As seen in Eq. 2.73, under the unitary transformations corresponding to ray transfer matrices $\mathbf{F}(d)$ and $\mathbf{L}(f)$ on $\psi(x, y; z)$, the Wigner distribution function transforms as $W(\mathbf{F}(d)^{-1}\boldsymbol{\xi})$ and $W(\mathbf{L}(f)^{-1}\boldsymbol{\xi})$ respectively.

2.7 Variance matrix

A paraxial coherent light field $\psi(x, y; z)$ can be characterized through its 4×4 variance matrix $\mathbf{V}$, whose entries $\mathbf{V}(i, j)$ are given by [63, 77, 89]

$$\mathbf{V}(i,j) = \langle\{\Delta\hat{\boldsymbol{\xi}}_i, \Delta\hat{\boldsymbol{\xi}}_j\}\rangle = \int \Delta\boldsymbol{\xi}_i \Delta\boldsymbol{\xi}_j W(\boldsymbol{\xi}) d^4\boldsymbol{\xi}. \tag{2.74}$$

Here, the operator array $\Delta\hat{\boldsymbol{\xi}}$ is defined as $\Delta\hat{\boldsymbol{\xi}} = [\Delta\hat{x}, \Delta\hat{p}_x, \Delta\hat{y}, \Delta\hat{p}_y]^{\mathrm{T}}$, with $\Delta\hat{\boldsymbol{\xi}}_i = \hat{\boldsymbol{\xi}}_i - \langle\hat{\boldsymbol{\xi}}_i\rangle$, and $\langle\hat{\boldsymbol{\xi}}_i\rangle = \int_{-\infty}^{\infty}\int_{-\infty}^{\infty} \psi^*(x, y; z)\, \hat{\boldsymbol{\xi}}_i\, \psi(x, y; z) dxdy$. Also, $\{\cdot\}$ denotes the anti-commutator. Under the action of a unitary transformation $\hat{\mathbf{U}}(\mathbf{S})$ the variance matrix $\mathbf{V}$ transforms as,

$$\mathbf{V} \longrightarrow \mathbf{V}' = \mathbf{S}\mathbf{V}\mathbf{S}^{\mathrm{T}}, \tag{2.75}$$

where $\mathbf{S}$ is the symplectic matrix corresponding to the unitary transformation $\hat{\mathbf{U}}(\mathbf{S})$.

2.8 Uncertainty principle

The uncertainties are defined as the expectations of the Hermitian operators $\{\Delta\hat{\boldsymbol{\xi}}_i, \Delta\hat{\boldsymbol{\xi}}_j\} = (\Delta\hat{\boldsymbol{\xi}}_i\Delta\hat{\boldsymbol{\xi}}_j + \Delta\hat{\boldsymbol{\xi}}_j, \Delta\hat{\boldsymbol{\xi}}_i)/2$:

$$\langle\{\Delta\hat{\boldsymbol{\xi}}_i, \Delta\hat{\boldsymbol{\xi}}_j\}\rangle = \int \Delta\boldsymbol{\xi}_i \Delta\boldsymbol{\xi}_j W(\boldsymbol{\xi}) d^4\boldsymbol{\xi}. \tag{2.76}$$

Note that on arranging the uncertainties or variances into a 4×4 matrix we have the variance matrix $\mathbf{V}$ as defined in Eq. (2.74). Thus the uncertainty principle can be written in the

compact form as [63, 79, 90]

$$\mathbf{V} + \frac{i}{2\kappa}\Sigma \geq 0, \tag{2.77}$$

where Σ is as given by Eq. (2.57). Note that, by the inequality given above we mean that the matrix on the LHS is positive semi-definite, that is, the matrix have non negative eigenvalues.

2.9 Orbital angular momentum (OAM)

In the context of optics and electromagnetic waves, the OAM of a light field refers to the rotational component of its angular momentum. It arises from the spatial distribution of the wavefront and the phase structure of the light field. The OAM of the light field is associated with the helical or twisting nature of the wavefront. The OAM states can be generated using spiral phase plates (SPPs), computer-generated holograms, etc., which imprint a specific phase pattern onto the light field.

The OAM τ as evaluated on the paraxial light field $\psi(x, y; z)$ is [91]:

$$\begin{aligned} \tau &= \kappa \left[\left\langle \Delta\hat{x}\Delta\hat{p}_y \right\rangle - \left\langle \Delta\hat{y}\Delta\hat{p}_x \right\rangle \right] \quad \text{and} \\ &= \kappa \int_{-\infty}^{\infty}\int_{-\infty}^{\infty} (xp_y - yp_x) W(\boldsymbol{\xi}) dxdy, \end{aligned} \tag{2.78}$$

as evaluated on its Wigner distribution function [89]. It can be readily seen that the OAM τ can also be written as

$$\tau = \kappa \left[\mathbf{V}(1,4) - \mathbf{V}(2,3) \right], \tag{2.79}$$

where $\mathbf{V}$ is the variance matrix. The variance matrix $\mathbf{V}_{\mathrm{LG}}$ corresponding to an LG mode $\psi_{jm}(r, \theta; z)$ of Eq. (2.33) is given by [77]

$$\mathbf{V}_{\mathrm{LG}} = \begin{bmatrix} \frac{(2j+1)w_z^2}{4} & \frac{(2j+1)z}{\kappa^2 w_0^2} & 0 & \frac{m}{\kappa} \\ \frac{(2j+1)z}{\kappa^2 w_0^2} & \frac{(2j+1)}{\kappa^2 w_0^2} & -\frac{m}{\kappa} & 0 \\ 0 & -\frac{m}{\kappa} & \frac{(2j+1)w_z^2}{4} & \frac{(2j+1)z}{\kappa^2 w_0^2} \\ \frac{m}{\kappa} & 0 & \frac{(2j+1)z}{\kappa^2 w_0^2} & \frac{(2j+1)}{\kappa^2 w_0^2} \end{bmatrix}. \tag{2.80}$$

On evaluating τ of such an LG mode, we obtain [77,91]

$$\tau = \kappa \left[\mathbf{V}_{\mathrm{LG}}(1,4) - \mathbf{V}_{\mathrm{LG}}(2,3)\right] = 2m. \tag{2.81}$$

2.10 Partial coherence

For the sake of simplicity, we will refer to a one-dimensional optical light field. A spatially partially coherent scalar light field, is described by its cross-spectral density $\Gamma(x_1, x_2)$, or equivalently its cross-spectral density operator [86]

$$\hat{\Gamma} = \int\int dx_1 dx_2 \Gamma(x_1, x_2) |x_1\rangle\langle x_2|, \tag{2.82}$$

where $\Gamma(x_1, x_2) = \langle x_1|\hat{\Gamma}|x_2\rangle$. $\hat{\Gamma}$ is Hermitian positive semi-definite and $\Gamma(x, x) = I(x)$ is the transverse plane intensity. We consider light fields of normalized intensity, that is, $\int \Gamma(x, x)dx = 1$.

An equivalent representation of the light field is through the Wigner distribution function which captures all information contained in the cross-spectral density $\Gamma(x_1, x_2)$ [92, 93]. The Wigner distribution function $W(x, p_x)$ corresponding to the cross-spectral density operator $\hat{\Gamma}$ can be written as

$$W(x, p_x) = \frac{\kappa}{\pi} \int_{-\infty}^{\infty} \langle x + x'|\hat{\Gamma}|x - x'\rangle \mathrm{e}^{-i2\kappa x' p} dx'. \tag{2.83}$$

With $W(x, p_x) \equiv W(\xi)$, where $\xi = [x, p_x]^{\mathsf{T}}$, we have

$$\hat{\Gamma} \longrightarrow \hat{U}(S)\hat{\Gamma}\hat{U}^{\dagger}(S) \iff W(\xi) \longrightarrow W(S^{-1}\xi). \tag{2.84}$$

The uncertainty principle can be obtained as a consequence of the positivity of $\hat{\Gamma}$. For instance, by defining $\hat{m}_s = a_1\Delta\hat{x} + a_2\Delta\hat{p}_x$ with a_1 and a_2 to be complex coefficients, and constructing the positive operator $\hat{m}_s\hat{m}_s^{\dagger}$, we require

$$\langle \hat{m}_s\hat{m}_s^{\dagger}\rangle = \mathrm{tr}(\hat{m}_s\hat{m}_s^{\dagger}\hat{\Gamma}) \geq 0. \tag{2.85}$$

Here, for instance $\Delta\hat{x} = \hat{x} - \langle\hat{x}\rangle$, and $\mathrm{tr}(\cdot)$ denotes trace. The positivity requirement in

(2.85) can be equivalently written as

$$V + \frac{i}{2\kappa}\Omega \geq 0, \tag{2.86}$$

where the entries of the 2×2 variance matrix V are given by

$$V(i,j) = \langle\{\Delta\hat{\xi}_i, \Delta\hat{\xi}_j\}\rangle = \text{tr}(\{\Delta\hat{\xi}_i, \Delta\hat{\xi}_j\}\hat{\Gamma}) = \int \Delta\xi_i \Delta\xi_j W(\xi) d^2\xi. \tag{2.87}$$

Here $\Delta\hat{\xi} = [\Delta\hat{x}, \Delta\hat{p}_x]^{\text{T}}$, with $\Delta\hat{\xi}_i = \hat{\xi}_i - \langle\hat{\xi}_i\rangle$, and $\langle\hat{\xi}_i\rangle = \text{tr}(\hat{\xi}_i\hat{\Gamma})$. For states with $\langle\hat{\xi}_i\rangle = 0$, $V(i,j) = \langle\{\hat{\xi}_i, \hat{\xi}_j\}\rangle$.

Note that the inequality in (2.86) is the optical analogue of the quantum mechanical uncertainty principle, where h has been replaced with λ (see for instance Ref. [79]). Further, demanding the positivity of the determinant of the LHS of (2.86) will imply

$$(\langle\hat{x}^2\rangle - \langle\hat{x}\rangle^2)(\langle\hat{p}_x^2\rangle - \langle\hat{p}_x\rangle^2) \geq \frac{1}{4\kappa^2}, \tag{2.88}$$

the optical analogue of the Heisenberg uncertainty principle. In other words, the product of the squares of the spreads in position and direction of propagation (momentum) of the paraxial light field cannot be lower than a particular value determined by the wavelength.

Proceeding further, by Eq. (2.84), it is readily seen that when $\hat{\Gamma} \longrightarrow \hat{U}(S)\,\hat{\Gamma}\,\hat{U}^{\dagger}(S)$, the corresponding variance matrix

$$V \longrightarrow V' = SVS^{\text{T}}. \tag{2.89}$$

2.10.1 Gaussian cross-spectral density

A Gaussian cross-spectral density has its $\Gamma(x_1, x_2)$ to be Gaussian and we may henceforth denote it as $\Gamma_G(x_1, x_2) = \langle x_1|\hat{\Gamma}_G|x_2\rangle$. The corresponding Wigner distribution function $W_G(\xi)$ can be written as

$$W_G(\xi) = \frac{[\det(V_G)]^{-1/2}}{2\pi} \exp\left[-\frac{1}{2}\xi^{\text{T}} V_G^{-1}\xi\right]. \tag{2.90}$$

Here $\det(\cdot)$ denotes determinant. As evident, the variance matrix V_G completely determines the cross-spectral density operator. Further, from Eqs. (2.84) and (2.90), $\hat{U}(S)$ is Gaussianity preserving and can be labeled as a Gaussian unitary transformation.

A particular case of light sources with a Gaussian cross-spectral density are the Gaus-

sian Schell-model (GSM) [86] light fields, which are readily produced experimentally, for instance, using ground glass plates in Refs. [94, 95] and using SLMs by time varying the coherent light fields in Refs. [96–98]. The cross-spectral density of a scalar GSM light field at $z = 0$ can be written as

$$\langle x_1|\hat{\Gamma}_{sc}|x_2\rangle = \sqrt{\frac{\mathrm{c}(1-q)}{\pi(1+q)}}\exp\left[-\frac{\mathrm{c}(1-q)}{2(1+q)}(x_1^2+x_2^2) - \frac{\mathrm{c}q}{1-q^2}(x_1-x_2)^2\right], \tag{2.91}$$

$$\text{where } \hat{\Gamma}_{sc} = \sum_m \lambda_m |m\rangle\langle m|, \tag{2.92}$$

with $\lambda_m = (1-q)q^m$, c and q are positive parameters, and $0 \leq q < 1$. Note that $\int_{-\infty}^{\infty}\langle x|\hat{\Gamma}_{sc}|x\rangle dx = 1$. Using Eqs. 2.83 and 2.91, the corresponding Wigner distribution function $W_{sc}(\xi)$ is obtained as

$$\begin{aligned} W_{sc}(\xi) &= \frac{\kappa}{\pi}\int_{-\infty}^{\infty}\langle x+x'|\hat{\Gamma}_{sc}|x-x'\rangle \mathrm{e}^{-i2\kappa x' p}dx' \\ &= \frac{\kappa(1-q)}{\pi(1+q)}\exp\left[\frac{-\mathrm{c}(1-q)}{1+q}x^2 - \frac{\kappa^2(1-q)}{\mathrm{c}(1+q)}p^2\right]. \end{aligned} \tag{2.93}$$

Note that the GSM light field has the first order moments $\langle\hat{\xi}_i\rangle = 0$, and thus we have the entries of its variance matrix $V_{sc}(i,j) = \langle\hat{\xi}_i, \hat{\xi}_j\rangle$. Thus the uncertainty principle for the GSM light field can be written as

$$V_{sc} + \frac{i}{2\kappa}\Omega = \begin{bmatrix} \frac{1+q}{2\mathrm{c}(1-q)} & \frac{i}{2\kappa} \\ -\frac{i}{2\kappa} & \frac{\mathrm{c}}{2\kappa^2}\frac{1+q}{1-q} \end{bmatrix} \equiv \begin{bmatrix} a & \frac{i}{2\kappa} \\ -\frac{i}{2\kappa} & b \end{bmatrix} \geq 0, \tag{2.94}$$

where the diagonal entries are relabeled as a and b for brevity.

We note in passing that corresponding to any normalized centered Gaussian cross-spectral density operator $\hat{\Gamma}_G\left(\langle\hat{\xi}_i\rangle = 0\right)$, there is a normalized GSM density operator $\hat{\Gamma}_{sc}$ related through a Gaussian unitary $\hat{U}_0$, preserving the spectrum. That is [79],

$$\hat{\Gamma}_G \equiv \hat{U}_0\hat{\Gamma}_{sc}\hat{U}_0^{\dagger}, \tag{2.95}$$

and consequently we have

$$V_G = S_0 V_{sc} S_0^{\mathrm{T}}, \tag{2.96}$$

where S_0 is the symplectic matrix corresponding to $\hat{U}_0$.

2.11 Vector light fields

Consider a coherent paraxial vector light field propagating along the z-axis. Let us assign a binary variable u to denote the state of polarization of the vector light field. Any coherent polarization state can be written as [99]

$$|\eta\rangle = \sum_{u=0,1} c_u |u\rangle, \tag{2.97}$$

where $|0\rangle \equiv [1,0]^{\mathrm{T}}$ and $|1\rangle \equiv [0,1]^{\mathrm{T}}$ represent two orthogonal polarization states, say horizontal and vertical polarization states, respectively, and c_u are complex coefficients. A paraxial vector light field $|\Psi\rangle$, propagating along the z-axis can be represented as

$$|\Psi\rangle = c_0|0\rangle|\psi_1\rangle + c_1|1\rangle|\psi_2\rangle \equiv \begin{bmatrix} c_0|\psi_1\rangle \\ c_1|\psi_2\rangle \end{bmatrix}, \tag{2.98}$$

where $|\psi_1\rangle$ and $|\psi_2\rangle$ represent the spatial states of the light field in respective polarizations. In the position basis we have, $|x,y\rangle \equiv |x\rangle \otimes |y\rangle$, where $|x\rangle$ and $|y\rangle$ are eigenstates of the position operators $\hat{x}$ and $\hat{y}$ respectively, and they satisfy [76, 79, 99]

$$\hat{x}|x\rangle = x|x\rangle, \text{ and } \hat{y}|y\rangle = y|y\rangle. \tag{2.99}$$

In the position representation a spatial state $|\psi_i\rangle$ can be represented as the field amplitude $\psi_i(x,y) \equiv \langle x,y|\psi_i\rangle$, so that

$$\Psi(x,y) = \begin{bmatrix} c_0\psi_1(x,y) \\ c_1\psi_2(x,y) \end{bmatrix}. \tag{2.100}$$

2.11.1 Partially coherent vector light field

Let us now move on to partially coherent vector light fields. A spatially partially coherent vector light field is characterized by its cross-spectral density operator

$$\hat{\mathbf{\Gamma}} = \sum_{i}^{n} p_i |\Psi_i\rangle\langle\Psi_i|, \tag{2.101}$$

where in the polarization spatial state

$$|\Psi_i\rangle = \begin{bmatrix} c_{0i}|\psi_{1i}\rangle \\ c_{1i}|\psi_{2i}\rangle \end{bmatrix} \tag{2.102}$$

occurs with probability p_i.

Let us consider a partially coherent vector light field in single variable. $\{|u;x\rangle = |u\rangle \otimes |x\rangle\}$ provide a natural basis in the polarization-spatial degrees of freedom. The cross-spectral density operator $\hat{\mathbf{\Gamma}}$ which is Hermitian and positive semi-definite can be defined as [100]

$$\hat{\mathbf{\Gamma}} = \sum_{u,v} dx_1 dx_2 \Gamma_{uv}(x_1, x_2)|u;x_1\rangle\langle v;x_2|, \tag{2.103}$$

where $\Gamma_{uv}(x_1, x_2) = \langle u;x_1|\hat{\Gamma}|v;x_2\rangle$. Note that, in the position representation the point-wise transverse plane intensity of the vector light field is given by $\Gamma_{00}(x,x) + \Gamma_{11}(x,x) = I(x)$. Henceforth we consider vector light fields having normalized intensity, that is, $\int [\Gamma_{00}(x,x) + \Gamma_{11}(x,x)]\, dx = 1$.

A simple example of $\hat{\mathbf{\Gamma}}$ would be the product polarization-spatial Gaussian cross-spectral density operator

$$\hat{\mathbf{\Gamma}}_G = |\eta\rangle\langle\eta| \otimes \hat{\Gamma}_G = \begin{bmatrix} |c_0|^2\hat{\Gamma}_G & c_0c_1^*\hat{\Gamma}_G \\ c_1c_0^*\hat{\Gamma}_G & |c_1|^2\hat{\Gamma}_G \end{bmatrix}, \tag{2.104}$$

where $|\eta\rangle$ is a polarization state and $\hat{\Gamma}_G$ is a Gaussian cross-spectral density operator.

2.11.2 Generalized uncertainty principle

Consider the operator $\hat{m}_v = |0\rangle \otimes (a_1\hat{x} + a_2\hat{p}_x) + |1\rangle \otimes (a_3\hat{x} + a_4\hat{p}_x)$, where a_1, a_2, a_3 and a_4 are complex coefficients, and construct the positive operator $\hat{m}_v\hat{m}_v^\dagger$. We have

$$\langle \hat{m}_v\hat{m}_v^\dagger \rangle = \text{tr}(\hat{m}_v\hat{m}_v^\dagger\hat{\mathbf{\Gamma}}_G) \geq 0, \tag{2.105}$$

and consequently we have the following matrix to be positive semi-definite, i.e., [101]

$$\begin{bmatrix} \langle\hat{x}^2\rangle_{00} & \langle\hat{x}\hat{p}_x\rangle_{00} & \langle\hat{x}^2\rangle_{01} & \langle\hat{x}\hat{p}_x\rangle_{01} \\ \langle\hat{p}_x\hat{x}\rangle_{00} & \langle\hat{p}_x^2\rangle_{00} & \langle\hat{p}_x\hat{x}\rangle_{01} & \langle\hat{p}_x^2\rangle_{01} \\ \langle\hat{x}^2\rangle_{10} & \langle\hat{x}\hat{p}_x\rangle_{10} & \langle\hat{x}^2\rangle_{11} & \langle\hat{x}\hat{p}_x\rangle_{11} \\ \langle\hat{p}_x\hat{x}\rangle_{10} & \langle\hat{p}_x^2\rangle_{10} & \langle\hat{p}_x\hat{x}\rangle_{11} & \langle\hat{p}_x^2\rangle_{11} \end{bmatrix} \geq 0, \tag{2.106}$$

which is the generalized uncertainty principle for the vector case. Here the subscripts of the matrix entries in the LHS of (2.106) denote the polarization components.

On considering unitary transformations that includes translations, we need an uncertainty principle that involves the first order moments. To this end, we define the operator $\hat{m}_c = |0\rangle \otimes (a_1 + a_2\hat{x} + a_3\hat{p}_x) + |1\rangle \otimes (a_4 + a_5\hat{x} + a_6\hat{p}_x)$, where a_1, a_2, a_3, a_4, a_5 and a_6 are complex coefficients, and construct the positive operator $\hat{m}_c\hat{m}_c^\dagger$. We have

$$\langle\hat{m}_c\hat{m}_c^\dagger\rangle = \mathrm{tr}(\hat{m}_c\hat{m}_c^\dagger\hat{\mathbf{\Gamma}}_G) \geq 0, \tag{2.107}$$

and consequently

$$\begin{bmatrix} \langle 1\rangle_{00} & \langle\hat{x}\rangle_{00} & \langle\hat{p}_x\rangle_{00} & \langle 1\rangle_{01} & \langle\hat{x}\rangle_{01} & \langle\hat{p}_x\rangle_{01} \\ \langle\hat{x}\rangle_{00} & \langle\hat{x}^2\rangle_{00} & \langle\hat{x}\hat{p}_x\rangle_{00} & \langle\hat{x}\rangle_{01} & \langle\hat{x}^2\rangle_{01} & \langle\hat{x}\hat{p}_x\rangle_{01} \\ \langle\hat{p}_x\rangle_{00} & \langle\hat{p}_x\hat{x}\rangle_{00} & \langle\hat{p}_x^2\rangle_{00} & \langle\hat{p}_x\rangle_{01} & \langle\hat{p}_x\hat{x}\rangle_{01} & \langle\hat{p}_x^2\rangle_{01} \\ \langle 1\rangle_{10} & \langle\hat{x}\rangle_{10} & \langle\hat{p}_x\rangle_{10} & \langle 1\rangle_{11} & \langle\hat{x}\rangle_{11} & \langle\hat{p}_x\rangle_{11} \\ \langle\hat{x}\rangle_{10} & \langle\hat{x}^2\rangle_{10} & \langle\hat{x}\hat{p}_x\rangle_{10} & \langle\hat{x}\rangle_{11} & \langle\hat{x}^2\rangle_{11} & \langle\hat{x}\hat{p}_x\rangle_{11} \\ \langle\hat{p}_x\rangle_{10} & \langle\hat{p}_x\hat{x}\rangle_{10} & \langle\hat{p}_x^2\rangle_{10} & \langle\hat{p}_x\rangle_{11} & \langle\hat{p}_x\hat{x}\rangle_{11} & \langle\hat{p}_x^2\rangle_{11} \end{bmatrix} \geq 0, \tag{2.108}$$

which is the generalized uncertainty principle for the vector case including translations. Here the subscripts of the matrix entries in the LHS of (2.108) denote the polarization components.

2.12 Entanglement

As mentioned in Chapter 1, the notion of entanglement emerges naturally from the superposition principle when one deals with tensor product of vector spaces. It has been well explored in the context of quantum mechanical systems [14]. More recently, the notion has been explored in the context of optics and is generally referred to as classical entanglement of optical field. It has been explored both in the scalar [59, 68, 102, 103] and vecto-

rial [6, 7, 25–40, 104] regimes. Light fields having entangled degrees of freedom has been used in polarization metrology [29] as well as in encoding information for optical communication [37, 38, 104]. They have been further used for characterizing channels [39] and for computation [40].

Detection and estimation of entanglement in light fields having entangled degrees of freedom has been demonstrated in several works [25,33,34,36,41–44,46,47,56,103–111]. Violation of Bell-type inequality to detect entanglement in the optical context has been demonstrated in Refs. [25, 33, 34, 36, 103]. Similarly, violation of Mermin's inequality was demonstrated in Ref. [105], and the Clauser-Horne Shimony-Holt (CHSH) inequality in Refs. [46, 47, 106]. The analogue of quantum tomography in the optical context has been demonstrated in [41–44]. In Ref. [43], the notion of coherence was extended in the most general manner through entanglement by considering the polarization, spatial, and temporal degrees of freedom

2.12.1 Polarization-spatial entanglement

Consider a paraxial vector light field $|\Psi\rangle$ as in Eq. (2.98), propagating along the z-axis. When $|\psi_1\rangle = |\psi_2\rangle = |\psi_s\rangle$, $\Psi(x, y)$ of Eq. (2.100) is manifestly of the product form in the polarization-spatial degrees of freedom and can be denoted as $\Psi_s(x, y)$. That is, we have

$$\Psi_s(x, y) = \begin{bmatrix} c_0 \\ c_1 \end{bmatrix} \psi_s(x, y). \tag{2.109}$$

On the contrary, when $|\psi_1\rangle \neq |\psi_2\rangle$, $\Psi(x, y)$ of Eq. (2.100) is polarization-spatial entangled.

Assuming that the source is quasi-monochromatic, the density matrix corresponding to a coherent paraxial vector light field can be expressed as [112, 113]:

$$\begin{aligned} \rho(x, y) &= \Psi(x, y)\Psi(x, y)^\dagger \\ &= \begin{bmatrix} |c_0|^2|\psi_1(x, y)|^2 & c_0c_1^*\psi_1(x, y)\psi_2^*(x, y) \\ c_1c_0^*\psi_2(x, y)\psi_1^*(x, y) & |c_1|^2|\psi_2(x, y)|^2 \end{bmatrix}. \end{aligned} \tag{2.110}$$

The polarization-spatial entanglement of $\Psi(x, y)$ can be evaluated, for instance, from the reduced density matrix ρ_p (also the polarization matrix) resulting from $\rho(x, y)$ by tracing

away the spatial degrees of freedom. That is,

$$\rho_p = \begin{bmatrix} \iint |c_0|^2 |\psi_1(x,y)|^2 dxdy & \iint c_0 c_1^* \psi_1(x,y)\psi_2^*(x,y)dxdy \\ \iint c_0^* c_1 \psi_1^*(x,y)\psi_2(x,y)dxdy & \iint |c_1|^2 |\psi_2(x,y)|^2 dxdy \end{bmatrix}$$
$$\equiv \begin{bmatrix} \rho_{00} & \rho_{01} \\ \rho_{10} & \rho_{11} \end{bmatrix}. \tag{2.111}$$

The Stokes parameters S_0, S_1, S_2 and S_3 are obtained from the entries of ρ_p as [86]:

$$\mathrm{S}_0 = \rho_{00} + \rho_{11}, \tag{2.112}$$
$$\mathrm{S}_1 = \rho_{00} - \rho_{11}, \tag{2.113}$$
$$\mathrm{S}_2 = \rho_{01} + \rho_{10}, \tag{2.114}$$
$$\mathrm{S}_3 = i\left(\rho_{10} - \rho_{01}\right). \tag{2.115}$$

Here $\mathrm{S}_0 \approx 1$ since we have normalized the field intensity. The degree of polarization $S(\rho_p) = \sqrt{\mathrm{S}_1^2 + \mathrm{S}_2^2 + \mathrm{S}_3^3}$ can be restated in terms of the eigenvalues $\lambda_\pm$ of ρ_p as [112]:

$$S(\rho_p) = \lambda_+ - \lambda_-. \tag{2.116}$$

Note that $(\lambda_+ + \lambda_-) = \mathrm{S}_0$.

The degree of polarization-spatial entanglement can be quantified through concurrence as defined on $\Psi(x,y)$ and evaluated on ρ_p, i.e., $C(\rho_p) = \sqrt{2[1 - \mathrm{tr}(\rho_p^2)]}$ [43, 114, 115], which in the present context reduces to

$$C(\rho_p) = 2\sqrt{\lambda_+ \lambda_-}. \tag{2.117}$$

Note that $C^2(\rho_p) + S^2(\rho_p) = 1$ [43].

The polarization-spatial entanglement as contained in $\Psi(x,y)$ can also be quantified through the von-Neumann entropy of the reduced density matrix ρ_p as [66, 116]:

$$E(\rho_p) = -\lambda_+ \log(\lambda_+) - \lambda_- \log(\lambda_-), \tag{2.118}$$

where '$\log$' denotes logarithm to the base 2.

2.12.2 Detection of polarization-spatial entanglement using partial transpose map

Let us say we have a general state $\hat{\rho}$ which acts on the Hilbert space $\mathcal{H} = \mathcal{H}_A \otimes \mathcal{H}_B$, where $\mathcal{H}_A$ and $\mathcal{H}_B$ are the Hilbert spaces corresponding to the subsystems A and B, respectively. If we write the state as a block matrix we have

$$\rho = \begin{bmatrix} A_{11} & A_{12} & \cdots & A_{1n} \\ A_{21} & A_{22} & & \\ \vdots & & \ddots & \\ A_{n1} & & & A_{nn} \end{bmatrix}, \tag{2.119}$$

where $n = \dim(\mathcal{H}_A)$, and each block A_{ij} is a square matrix of dimension $m = \dim(\mathcal{H}_B)$. On taking partial transpose (with respect to the subsystem B) we obtain

$$\rho^{\mathrm{PT}_B} = \begin{bmatrix} A_{11}^{\mathrm{T}} & A_{12}^{\mathrm{T}} & \cdots & A_{1n}^{\mathrm{T}} \\ A_{21}^{\mathrm{T}} & A_{22}^{\mathrm{T}} & & \\ \vdots & & \ddots & \\ A_{n1}^{\mathrm{T}} & & & A_{nn}^{\mathrm{T}} \end{bmatrix}. \tag{2.120}$$

If $\hat{\rho}$ is separable then we have

$$\rho^{\mathrm{PT}_B} \geq 0, \tag{2.121}$$

also called as the Peres-Horodecki separability criterion [60,61]. In other words, if ρ^{PT_B} has a negative eigenvalue, then $\hat{\rho}$ is non-separable. The result is independent of the subsystem that was transposed.

Partial transpose map has been found to be necessary and sufficient in detecting bipartite entanglement in certain finite dimensional [14, 61, 62, 64] as well as infinite dimensional contexts [21–23, 63]. In order to apply partial transpose to the present context consider a polarization-spatial density operator

$$\hat{\rho} = \begin{bmatrix} |c_0|^2 |\psi_1\rangle\langle\psi_1| & c_0 c_1^* |\psi_1\rangle\langle\psi_2| \\ c_1 c_0^* |\psi_2\rangle\langle\psi_1| & |c_1|^2 |\psi_2\rangle\langle\psi_2| \end{bmatrix}. \tag{2.122}$$

On taking transpose on the spatial part alone we obtain

$$\hat{\rho}^{\text{PT}} = \begin{bmatrix} |c_0|^2(|\psi_1\rangle\langle\psi_1|)^{\text{T}} & c_0c_1^*(|\psi_1\rangle\langle\psi_2|)^{\text{T}} \\ c_1c_0^*(|\psi_2\rangle\langle\psi_1|)^{\text{T}} & |c_1|^2(|\psi_2\rangle\langle\psi_2|)^{\text{T}} \end{bmatrix}. \tag{2.123}$$

The partial transpose map has implications on the uncertainties or second moments. On implementing transpose operation through the generalized uncertainty principle we have (see Section 2.11.2)

$$\text{tr}(\hat{m}_c\hat{m}_c^\dagger\hat{\rho}^{\text{PT}}) \geq 0. \tag{2.124}$$

The above inequality has to be satisfied for $\hat{\rho}$ to be separable in the polarization-spatial degrees of freedom. In other words violation of (2.124) implies $\hat{\rho}$ is entangled in the polarization-spatial degrees of freedom.

We may recall that a spatially partially coherent vector light field is characterized by its cross-spectral density operator $\hat{\mathbf{\Gamma}}$ as in

$$\hat{\mathbf{\Gamma}} = \sum_i^n p_i|\Psi_i\rangle\langle\Psi_i|, \tag{2.125}$$

as seen in Eq. (2.101). When every $|\Psi_i\rangle$ of the decomposition is of the product form, i.e., when $|\psi_{1i}\rangle = |\psi_{2i}\rangle\,\forall\, i$, $\hat{\mathbf{\Gamma}}$ is said to be separable in the polarization and spatial degrees of freedom. Detection of polarization-spatial entanglement in partially coherent vector light fields by implementing partial transpose through the generalized uncertainty principle is illustrated in Chapter 4.

2.13 Concluding remarks

To summarize, we covered a range of topics in this chapter. First, we examined ray transfer matrices, corresponding to symmetric and asymmetric optical transformations including free propagation, thin lenses, and thin cylindrical lenses, in the paraxial limit. We also touched upon Maxwell's equations and the paraxial wave equation, as well as their solutions. Next, we explored the Huygen's Fresnel diffraction principle and the Fresnel approximation for free space propagation. The concept of a thin lens as a phase transformation was also discussed. We further delved into the unitary representation of various optical transformations. In addition, we explored the Wigner distribution function, variance ma-

trix, uncertainty principle and OAM associated with a paraxial light field. We discussed partial coherence in both scalar and vector light fields. A generalized uncertainty principle suited for the polarization-spatial degrees of freedom is obtained in this chapter. Lastly, we outlined the topic of entanglement between different degrees of freedom of a paraxial light field.

Chapter 3

Polarization-spatial Gaussian entanglement in a folded Mach-Zehnder interferometer

3.1 Introduction

In this chapter, we show that fringe movement in intensity of the light field on insertion and rotation of a polarizer, is a sufficient criteria for polarization-spatial entanglement in coherent paraxial vector light fields. Polarization-spatial entanglement is estimated by tracing away the spatial degrees of freedom in order to obtain the reduced density matrix (polarization matrix) whose eigenvalues then characterize the polarization-spatial entanglement. We demonstrate close to 1 ebit [116, 117] of entanglement by coupling non-orthogonal spatially overlapping Gaussian modes with slight relative tilts, with orthogonal states of polarization, in a folded Mach-Zehnder interferometer, using a QWP and a linear polarizer. Tunable polarization-spatial entanglement is demonstrated by varying the polarization of the Gaussian light field at the input of the folded Mach-Zehnder interferometer. We note that maximal polarization-spatial entanglement of 1 ebit is typically obtained by coupling orthogonal spatial modes with orthogonal states of polarization [33, 56].

The chapter is organized as follows. In Section 3.2, we outline how detection of polarization-spatial entanglement is possible through fringe movement. In Section 3.3, we review the method towards the estimation of polarization-spatial entanglement using a QWP and a linear polarizer. In Section 3.4, we outline a theoretical analysis wherein we show that two Gaussian light fields with a small relative tilt but with substantial spatial overlap, and orthogonal polarizations, can have close to 1 ebit of polarization-spatial entanglement. This is

attributed to the inherent wavelength dependent scale in the problem. Experimental demonstration of the detection of polarization-spatial entanglement through fringe movement and its estimation is outlined in the same Section. We finally end with some concluding remarks in Section 3.5.

3.2 Detection of coherent polarization-spatial entanglement using fringe movement

We outline a procedure which detects polarization-spatial entanglement through fringe movement. Consider the passage of a paraxial vector light field $\Psi(x,y)$ as in Eq. (2.109) through a rotated linear polarizer. We obtain the output to be

$$\begin{bmatrix} C_\theta^2 & S_\theta C_\theta \\ S_\theta C_\theta & S_\theta^2 \end{bmatrix} \begin{bmatrix} c_0 \\ c_1 \end{bmatrix} \psi(x,y) = (c_0 C_\theta + c_1 S_\theta) \begin{bmatrix} C_\theta \\ S_\theta \end{bmatrix} \psi(x,y). \tag{3.1}$$

Here $C_\theta \equiv \cos\theta$ and $S_\theta \equiv \sin\theta$. The intensity of light field after passage through the polarizer is given by

$$\begin{aligned} I_s(x,y) &= \left(|c_0|^2 C_\theta^2 + |c_1|^2 S_\theta^2 + c_0 c_1^* S_\theta C_\theta + c_1 c_0^* S_\theta C_\theta\right) |\psi(x,y)|^2 \\ &= |c_0 C_\theta + c_1 S_\theta|^2 |\psi(x,y)|^2. \end{aligned} \tag{3.2}$$

That is, $I_s(x,y)$ is essentially $|\psi(x,y)|^2$ modulated by an overall θ, c_0, and c_1 dependent factor. Consequently when we rotate the polarizer (vary θ) there is no fringe movement (movement of the zeros of the intensity) apart from an overall modulation of the intensity.

On the contrary, on passage of a paraxial vector light field as in Eq. (2.100) [not separable as in Eq. (2.109)] through a rotated linear polarizer, we obtain

$$\begin{bmatrix} C_\theta^2 & S_\theta C_\theta \\ S_\theta C_\theta & S_\theta^2 \end{bmatrix} \begin{bmatrix} c_0\psi_1(x,y) \\ c_1\psi_2(x,y) \end{bmatrix} = (c_0 C_\theta \psi_1(x,y) + c_1 S_\theta \psi_2(x,y)) \begin{bmatrix} C_\theta \\ S_\theta \end{bmatrix}. \tag{3.3}$$

The intensity of light field after passage through the polarizer is given by,

$$\begin{aligned} I_\theta(x,y) &= |c_0|^2 C_\theta^2 |\psi_1(x,y)|^2 + |c_1|^2 S_\theta^2 |\psi_2(x,y)|^2 \\ &\quad + c_0 c_1^* S_\theta C_\theta \psi_1(x,y)\psi_2^*(x,y) + c_0^* c_1 S_\theta C_\theta \psi_1^*(x,y)\psi_2(x,y) \\ &= |c_0 C_\theta \psi_1(x,y) + c_1 S_\theta \psi_2(x,y)|^2. \end{aligned} \tag{3.4}$$

That is, the resulting intensity is the consequence of the interference of the scalar amplitudes $c_0 C_\theta \psi_1(x,y)$ and $c_1 S_\theta \psi_2(x,y)$, and the zeros of the superposition $c_0 C_\theta \psi_1(x,y) + c_1 S_\theta \psi_2(x,y)$ can vary as θ is varied. In other words, as the polarizer is rotated, the fringes can move indicating the presence of polarization-spatial entanglement.

However, there are instances of polarization-spatial entangled light fields for which the rotation of the polarizer causes no fringe movement. For instance, consider the paraxial vectorial light field given by

$$\Psi(r,\chi) = \begin{bmatrix} \psi(r)\mathrm{e}^{i\chi} \\ \psi(r)\mathrm{e}^{-i\chi} \end{bmatrix}, \tag{3.5}$$

where $\psi(r)$ is the radial part of first-order LG modes $\psi_{\pm 1\,0}(r,\theta;z)$ ($l = \pm 1, p = 0$, see Section 2.2.4) and $\mathrm{e}^{\pm i\chi}$ is the angular part. As evident, the orthogonal spatial modes are coupled to the orthogonal states of polarization with equal Schmidt coefficients and hence the vector light field is maximally polarization-spatial entangled. On passage of the paraxial vectorial light field as in Eq. (3.5) through a rotated linear polarizer we obtain

$$\begin{bmatrix} C_\theta^2 & S_\theta C_\theta \\ S_\theta C_\theta & S_\theta^2 \end{bmatrix} \begin{bmatrix} \psi(r)\mathrm{e}^{i\chi} \\ \psi(r)\mathrm{e}^{-i\chi} \end{bmatrix} = \psi(r)\left(C_\theta \mathrm{e}^{i\chi} + S_\theta \mathrm{e}^{-i\chi}\right) \begin{bmatrix} C_\theta \\ S_\theta \end{bmatrix}. \tag{3.6}$$

The intensity of the light field after passage through the polarizer is given by

$$I(r,\chi,\theta) = (1 + S_{2\theta} C_{2\chi})\,|\psi(r)|^2. \tag{3.7}$$

That is, $I(r,\chi,\theta)$ is essentially $|\psi(r)|^2$ modulated by an overall θ and χ dependent factor. Consequently, when we rotate the polarizer (vary θ) there is no fringe movement (movement of the zeros of the intensity), apart from an overall modulation of the intensity. In this sense, fringe movement is a sufficient but not necessary condition for polarization-spatial entanglement, in the present context. In other words, fringe movement on insertion and rotation of a linear polarizer indicates the presence of polarization-spatial entanglement in coherent paraxial vector light fields, but fringe stationarity doesn't necessarily indicate the absence

of it. It is important to note that, though we cannot say that the light field is not entangled on observing fringe stationarity, we can still use fringe movement as a method to detect the presence of polarization-spatial entanglement and the same is demonstrated through examples later in this chapter.

Let us say that we were able to detect polarization spatial entanglement in a light field by observing fringe movement in the intensity of the light field on insertion and rotation of a linear polarizer. However, this does not aid us in quantifying the degree of entanglement present. As discussed in Section 2.12, polarization-spatial entanglement can be estimated through evaluation of the reduced density matrix ρ_p of Eq. (2.111). The procedure for evaluation of ρ_p through intensity measurements is discussed in the following section.

3.3 Estimation of polarization-spatial entanglement using intensity measurements

We now review the procedure to estimate the reduced density matrix ρ_p of Eq. (2.111) through intensity measurements, which is done by tracing away the spatial degrees of freedom, using a QWP and a linear polarizer [118]. On passage of $\Psi(x, y)$ through a QWP at 0° and then through a rotated linear polarizer we obtain,

$$\begin{aligned}\tilde{\Psi}(x,y) &= \begin{bmatrix} C_\theta^2 & S_\theta C_\theta \\ S_\theta C_\theta & S_\theta^2 \end{bmatrix} \begin{bmatrix} 1 & 0 \\ 0 & i \end{bmatrix} \begin{bmatrix} c_0\psi_1(x,y) \\ c_1\psi_2(x,y) \end{bmatrix} \\ &= (c_0 C_\theta \psi_1(x,y) + ic_1 S_\theta \psi_2(x,y)) \begin{bmatrix} C_\theta \\ S_\theta \end{bmatrix}. \end{aligned} \tag{3.8}$$

The intensity of light field $\tilde{\Psi}(x, y)$ is given by,

$$\begin{aligned}\tilde{I}_\theta(x,y) &= |c_0|^2 C_\theta^2 |\psi_1(x,y)|^2 + |c_1|^2 S_\theta^2 |\psi_2(x,y)|^2 \\ &\quad - ic_0 c_1^* S_\theta C_\theta \psi_1(x,y)\psi_2^*(x,y) + ic_0^* c_1 S_\theta C_\theta \psi_1^*(x,y)\psi_2(x,y) \\ &= |c_0 C_\theta \psi_1(x,y) + ic_1 S_\theta \psi_2(x,y)|^2. \end{aligned} \tag{3.9}$$

Using Eqs. (3.4) and (3.9) we can obtain the entries of ρ_p as

$$\rho_{00} = \iint I_{0^\circ}(x,y)dxdy, \tag{3.10}$$

$$\rho_{01} = \iint \frac{I_{45^\circ}(x,y) - I_{135^\circ}(x,y)}{2}dxdy + i\iint \frac{\tilde{I}_{45^\circ}(x,y) - \tilde{I}_{135^\circ}(x,y)}{2}dxdy, \tag{3.11}$$

$$\rho_{10} = \iint \frac{I_{45^\circ}(x,y) - I_{135^\circ}(x,y)}{2}dxdy - i\iint \frac{\tilde{I}_{45^\circ}(x,y) - \tilde{I}_{135^\circ}(x,y)}{2}dxdy, \tag{3.12}$$

$$\rho_{11} = \iint I_{90^\circ}(x,y)dxdy. \tag{3.13}$$

Note that in the above equations we have neglected the transmission loss due to both the polarizer and the QWP. As mentioned earlier in Section 2.12, once we have evaluated the reduced density matrix ρ_p, the polarization spatial entanglement can be estimated from the eigenvalues of ρ_p.

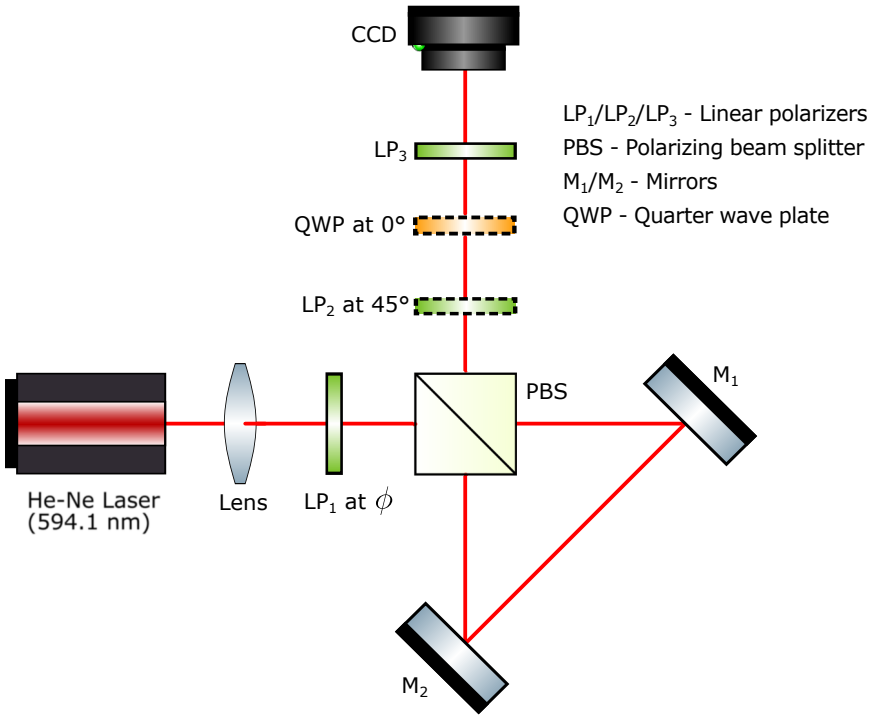

Figure 3.1: Schematic diagram of a folded Mach-Zehnder interferometer setup using PBS.

3.4 Experimental demonstration using a folded Mach-Zehnder interferometer

In order to experimentally obtain a coherent paraxial vector light field as in Eq. (2.100) we choose a folded Mach-Zehnder interferometer with a polarizing beam splitter (PBS) as shown in Fig. 3.1. Experimental demonstration of detection and estimation of polarization-spatial entanglement is carried out using this folded Mach-Zehnder interferometer setup. Here, for our experiment, the coherent Gaussian light field coming from a 594.1 nm He-Ne laser source is passed through a convex lens which controls the divergence. It is then passed through a linear polarizer (LP_1) oriented at ϕ and then through the PBS. The linearly polarized light falls on the PBS which splits the light into its horizontal and vertical components. The horizontal and vertical components take the clockwise and anti-clockwise paths respectively in the folded Mach-Zehnder interferometer and recombine at the PBS. While the two light fields traverse almost similar distances, they acquire slightly different tilts due to the orientation of mirrors M_1 and M_2. The width of the Gaussian light field emerging from the PBS was ≈ 1.3 mm in the present experiment. We now proceed to demonstrate detection as well as estimation of polarization-spatial entanglement in this recombined light field. But before doing so we first outline a theoretical analysis which suggests that it is possible to obtain close to 1 ebit of polarization-spatial entanglement with a Gaussian light field drawn from the same source with its orthogonal polarization components possessing a small relative tilt.

3.4.1 Theoretical analysis of the proposed experimental setup

Assume the linearly polarized (at ϕ) paraxial light field entering the PBS to be a Gaussian at the waist plane. That is,

$$\Psi(x,y) = \begin{bmatrix} C_\phi \\ S_\phi \end{bmatrix} \psi_0(x,y), \text{ where}$$
$$\psi_0(x,y) = a_0 \exp\left(-\frac{(x^2+y^2)}{w_0^2}\right). \tag{3.14}$$

Here a_0 is the initial amplitude. $\psi_0(x, y)$ after propagating through a distance z can be written as

$$\psi(x, y) = a_0 \exp\left(-\frac{(x^2 + y^2)}{w_z^2}\right) \exp\left(-\frac{i\kappa(x^2 + y^2)}{2R_z}\right) \exp\left(i\kappa z + i\zeta_z\right). \tag{3.15}$$

The horizontal and vertical components of the light field $\Psi(x, y)$ on passage through the folded Mach-Zehnder interferometer acquire a relative tilt such that the recombined light field can be written as

$$\Psi(x, y) = \begin{bmatrix} C_\phi \psi_1(x, y) \\ S_\phi \psi_2(x, y) \end{bmatrix}, \tag{3.16}$$

where $\psi_1(x, y) = \psi(x, y)$ and $\psi_2(x, y) = \psi(x', y')$, with $x' = x + z\delta_\alpha$, $y' = y$ and

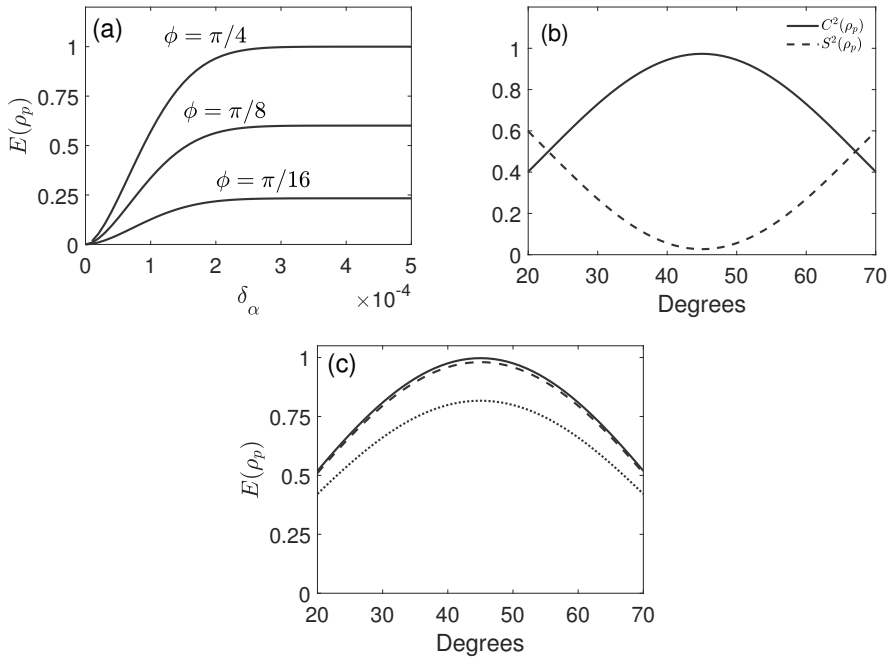

Figure 3.2: (a) plots the variation of polarization-spatial Gaussian entanglement $E(\rho_p)$ with relative tilt δ_α for various polarizer angles ϕ (see Fig. 3.1). (b) plots the variation of concurrence $C^2(\rho_p)$ (solid line) and degree of polarization $S^2(\rho_p)$ (dashed line) with polarizer angle ϕ for relative tilt $\delta_\alpha = 2.4 \times 10^{-4}$ radians. The solid line in (c) plots the variation of polarization-spatial Gaussian entanglement $E(\rho_p)$ with polarizer angle ϕ for the relative tilt $\delta_\alpha = 3 \times 10^{-4}$ radians, the dashed line plots the same for $\delta_\alpha = 2.4 \times 10^{-4}$ radians, and the dotted line for $\delta_\alpha = 1.5 \times 10^{-4}$ radians.

$z' = z - x\delta_\alpha$. We have assumed the tilt acquired to be along the x-z direction, and this

can be done without loss of generality. Since the two light fields traverse almost similar distances, we may further assume that w_z, R_z and ζ_z is approximately same for $\psi_1(x,y)$ and $\psi_2(x,y)$. Thus $\psi_2(x,y)$ can be written as

$$\begin{aligned}\psi_2(x,y) =& a_0 \exp\left(-\frac{((x+z\delta_\alpha)^2+y^2)}{w_z^2}\right)\exp\left(-\frac{i\kappa((x+z\delta_\alpha)^2+y^2)}{2R_z}\right)\\ &\times\exp\left(i\kappa(z-x\delta_\alpha)+i\zeta_z\right).\end{aligned} \tag{3.17}$$

Substituting from Eqs. (3.15) - (3.17) in Eqs. (3.10) - (3.13), the entries of reduced density matrix ρ_p after normalization is evaluated to be

$$\rho_{00} = C_\phi^2, \tag{3.18}$$

$$\rho_{01} = C_\phi S_\phi \exp\left(-\frac{z^2\delta_\alpha^2}{2w_z^2} - \frac{\kappa^2\delta_\alpha^2 w_z^2}{8}\left(1+\frac{z}{R_z}\right)^2 - \frac{i\kappa z\delta_\alpha^2}{2}\right), \tag{3.19}$$

$$\rho_{10} = C_\phi S_\phi \exp\left(-\frac{z^2\delta_\alpha^2}{2w_z^2} - \frac{\kappa^2\delta_\alpha^2 w_z^2}{8}\left(1+\frac{z}{R_z}\right)^2 + \frac{i\kappa z\delta_\alpha^2}{2}\right), \tag{3.20}$$

$$\rho_{11} = S_\phi^2. \tag{3.21}$$

The eigenvalues of ρ_p are now given by,

$$\lambda_\pm = \frac{\text{tr}(\rho_p) \pm \sqrt{\text{tr}^2(\rho_p) - 4\,\det(\rho_p)}}{2}. \tag{3.22}$$

In the present situation,

$$\text{tr}(\rho_p) = 1, \quad \text{and} \tag{3.23}$$

$$\det(\rho_p) = C_\phi^2 S_\phi^2\left[1-\exp\left[-\frac{z^2\delta_\alpha^2}{w_z^2} - \frac{\kappa^2\delta_\alpha^2 w_z^2}{4}\left(1-\frac{z}{R_z}\right)^2\right]\right]. \tag{3.24}$$

Note that when the relative tilt $\delta_\alpha = 0$ determinant of reduced density matrix $\det(\rho_p)$ equals 0 and the polarization-spatial entanglement is zero. However when $\delta_\alpha \neq 0$, the exponent in the right-hand side of Eq. (3.24) is sufficiently close to one for a sufficiently small but significant δ_α owing to the term proportional to $\kappa^2\delta_\alpha^2$ in the exponent. Consequently for such δ_α, $\det(\rho_p) \approx C_\phi^2 S_\phi^2$. When $C_\phi = S_\phi = \frac{1}{\sqrt{2}}$, we have $\lambda_\pm \approx \frac{1}{2}$, and the polarization-spatial entanglement is almost 1. To illustrate this we plot polarization-spatial Gaussian entanglement $E(\rho_p)$ as a function of relative tilt δ_α for various ϕ in Fig. 3.2 (a). Here we choose the propagation distance z to be 30 cm, with relative tilt angle δ_α to be

of the order of 10^{-4} radians. Figure 3.2 (b) plots the variation of $C^2(\rho_p)$ and $S^2(\rho_p)$ with polarizer angle ϕ for relative tilt $\delta_\alpha = 2.4 \times 10^{-4}$ radians. Figure 3.2 (c) plots the variation of polarization-spatial Gaussian entanglement $E(\rho_p)$ with polarizer angle ϕ for the relative tilts $\delta_\alpha = 3 \times 10^{-4}$ radians, 2.4×10^{-4} radians and 1.5×10^{-4} radians. As evident from Fig. 3.2 (c), for a relative tilt as low as $\delta_\alpha \approx 2.4 \times 10^{-4}$ radians we can have the polarization-spatial Gaussian entangled light field to be almost in Schmidt form (i.e., the Gaussian spatial modes corresponding to the orthogonal polarization components have their overlap integral to be approximately zero), even though the Gaussian light fields overlap spatially in a significant manner. For the above analysis w_0 was assumed to be 1.5 mm and $\lambda = 594$ nm.

3.4.2 Detecting polarization-spatial entanglement experimentally

The initial polarizer (LP_1) is kept at 45° so that we may have comparable intensities for the two interfering light fields thus ensuring better fringe contrast. In order to detect polarization-spatial entanglement through fringe movement the output light field from the PBS is passed through a single linear polarizer (LP_3). Figures 3.3 (a1) - 3.3 (a5) shows the output images recorded when LP_3 is varied from 70° to 110° at intervals of 10°. The shift in fringes is visible from the figure [see Eq. (3.4)], and this suggests the presence of polarization-spatial entanglement.

For zero entanglement case the fringes should remain stationary and this is demonstrated by introducing another polarizer (LP_2) at the output arm. The light field emerging out of LP_2 is linearly polarized and has a fixed spatial profile. Here, in order to get maximum intensity at the output we fix LP_2 at 45°. The output image is recorded by the charge-coupled device (CCD) in the same manner as before. Figures 3.3 (c1) - 3.3 (c5) shows the output images recorded when LP_3 is varied from 70° to 110° at intervals of 10°. Though there is a variation in fringe contrast the stationarity of the fringes is clearly in agreement with the fact that we have zero polarization-spatial entanglement [see Eq. (3.2)]. Figures 3.3 (b1) - 3.3 (b5) and Figs. 3.3 (d1) - 3.3 (d5) plots the fringes shown in Figs. 3.3 (a1) - 3.3 (a5) and Figs. 3.3 (c1) - 3.3 (c5), respectively reoriented along the x-axis (through a 45° coordinate transformation on the interferograms), so that the fringe shift (or fringe stationarity) is readily seen. A white line is drawn across the intensity plots shown in Figs. 3.3 (b1) - 3.3 (b5) at precisely the same location. As seen from the figure, the line resides over a dark fringe in Fig. 3.3 (b1), whereas it coincides with a bright fringe in Fig. 3.3 (b5), clearly indicating a shift in fringes. Similarly a white line is plotted across intensity plots

shown in Figs. 3.3 (d1) - 3.3 (d5), and it resides over the same dark fringe in all the figures indicating fringe stationarity. Figures 3.3 (e1) and 3.3 (e2) plot the diagonal entries in the interferograms 3.3 (a1), 3.3 (a3) and 3.3 (a5), and 3.3 (c1), 3.3 (c3) and 3.3 (c5), in order to make the fringe shift (or stationarity) even more explicit. The solid line, dotted line and dashed line of Fig. 3.3 (e1) correspond to diagonal entries of the interferograms in Figs. 3.3 (a1), 3.3 (a3) and 3.3 (a5) respectively [equivalently the x-axis entries of interferograms Figs. 3.3 (b1), 3.3 (b3) and 3.3 (b5)]. It is seen that the maxima of the solid line almost coincide with the minima of the dashed line indicating clearly the fringe shift. Similarly the solid line, dotted line and dashed line of Fig. 3.3 (e2) correspond to diagonal entries of the interferograms in Figs. 3.3 (c1), 3.3 (c3) and 3.3 (c5) respectively [equivalently the x-axis entries of interferograms Figs. 3.3 (d1), 3.3 (d3) and 3.3 (d5)]. The maxima and minima of all three lines coincide in this case indicating fringe stationarity.

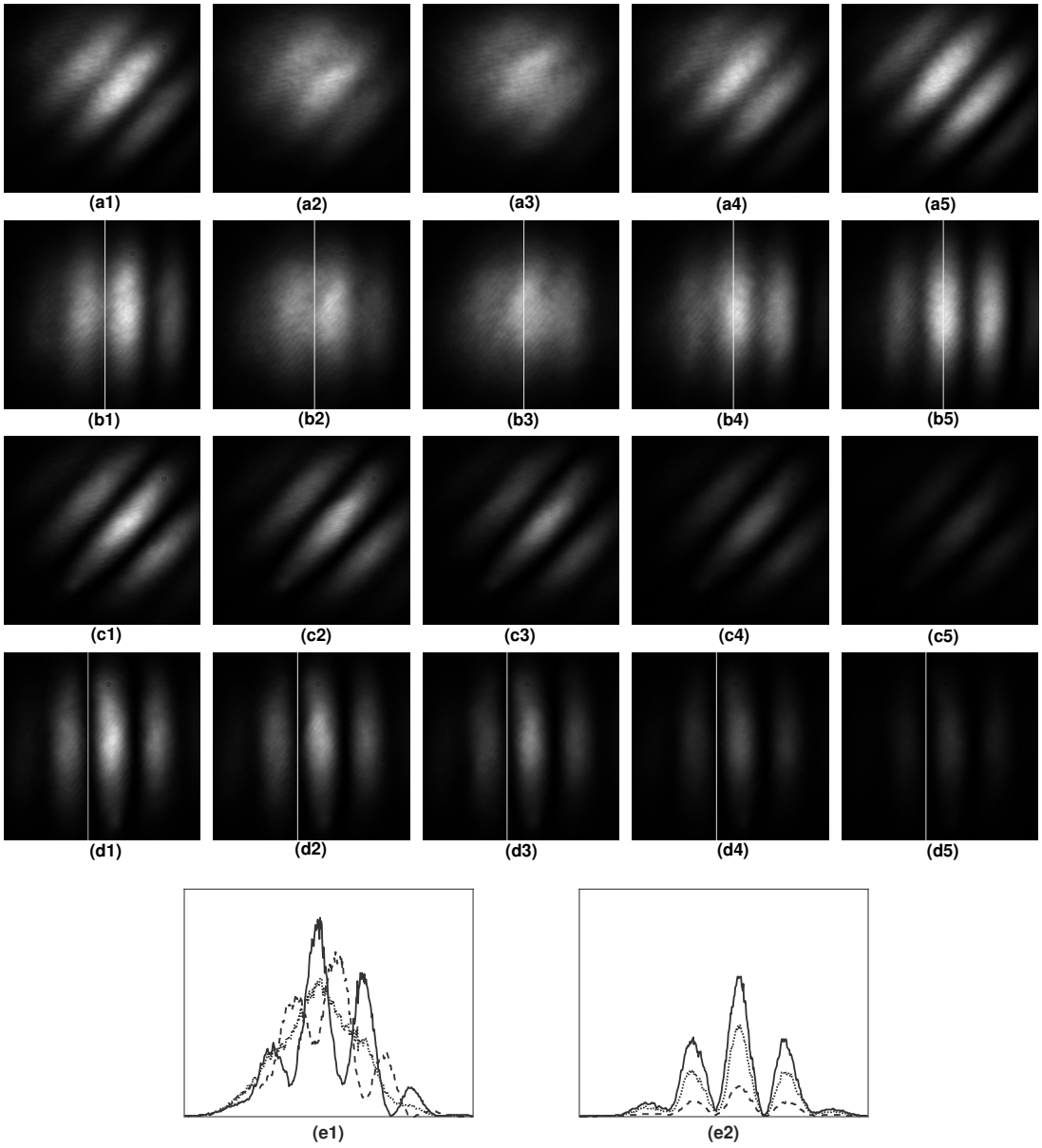

Figure 3.3: (a1) - (a5) plot the fringe pattern obtained on passage of the recombined light field emerging from the PBS through the polarizer LP_3 alone (refer Fig. 3.1). LP_3 is rotated from 70° to 110° in steps of 10°. (c1) - (c5) plot the fringe pattern obtained on passage of the recombined light field emerging from the PBS through the polarizers LP_2 and LP_3, with polarizer LP_2 (at 45°) inserted between LP_3 and the PBS. (b1) - (b5) and (d1) - (d5) re plot the fringes shown in (a1) - (a5) and (c1) - (c5) reoriented through a 45° coordinate transformation in order to make the fringe shift or fringe stationarity more explicit (observe the white line). This is made even more clear in (e1) and (e2). Solid line of (e1) plots the diagonal entries of (a1), dotted line plots the diagonal entries of (a3) and dashed line plots the diagonal entries of (a5). Similarly solid line of (e2) plots the diagonal entries of (c1), dotted line plots the diagonal entries of (c3) and dashed line plots the diagonal entries of (c5). In all the experiments the initial polarizer LP_1 is fixed at 45°.

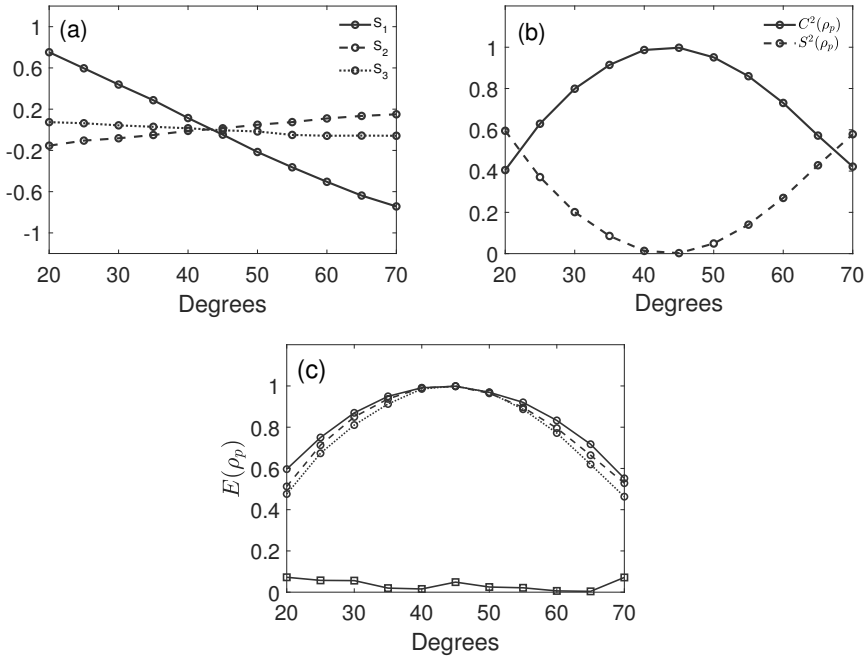

Figure 3.4: (a) plots the variation of estimated Stokes parameters S_1 (solid line), S_2 (dashed line) and S_3 (dotted line) with polarizer angle ϕ for a particular tilt, as obtained from ρ_p. (b) plots the variation of $C^2(\rho_p)$ (solid line) and $S^2(\rho_p)$ (dashed line) with polarizer angle ϕ for a particular tilt. The $\circ$ in (c) plot the estimated polarization-spatial entanglement $E(\rho_p)$ for three different tilts (shown by solid, dashed and dotted lines) when LP_2 is not inserted after the PBS, for varying ϕ. The $\square$ in (c) plot the estimated polarization-spatial entanglement $E(\rho_p)$ for a particular tilt when LP_2 is inserted after the PBS (see Fig. 3.1).

3.4.3 Estimating polarization-spatial entanglement experimentally

A relative tilt is introduced in one of the mirrors (see Fig. 3.1), and the presence of polarization-spatial entanglement is ensured through the fringe movement on rotation of polarizer LP_3 (without the insertion of LP_2 or QWP). Having ensured the presence of polarization-spatial entanglement, polarizer LP_1 is varied from 20° to 70° at intervals of 5° and the polarization-spatial entanglement is estimated for each orientation using the procedure outlined in Section 3.3 [see Eqs. (3.10) - (3.13)]. In order to estimate polarization-spatial entanglement using intensity measurements, first the output light field emerging from the PBS (for a fixed LP_1 angle) is passed through a single polarizer (LP_3) and the output image is recorded for every 45° rotation of LP_3 from 0° to 135° (for example see Fig. 3.3). For the next step a QWP at 0° is inserted between the PBS and polarizer LP_3 and the output image is recorded when LP_3 is at 45° and 135°. 50 intensity samples are taken at each orientation of LP_3

and averaged to suppress point wise intensity fluctuation. Using these intensity measurements polarization-spatial entanglement is estimated as outlined in Eqs. (3.10) - (3.13) by performing the integrals numerically. The experiment is repeated with the insertion of the polarizer LP_2 (at 45°) just after the PBS in which case the polarization-spatial entanglement is ideally zero. Figure 3.4 (a) plots the estimated Stokes parameters S_1 (solid line), S_2 (dashed line) and S_3 (dotted line) [see Eqs. (2.113) - (2.115)] for a particular tilt by varying the LP_1 angle from 20° to 70° in steps of 5°. Figure 3.4 (b) plots $S^2(\rho_p)$ (dashed line) and $C^2(\rho_p)$ (solid line) [see Eqs. (2.116) - (2.117)] for a particular tilt by varying the LP_1 angle from 20° to 70° in steps of 5°. In Fig. 3.4 (c) the $\circ$ plot the estimated polarization-spatial Gaussian entanglement [see Eq. (2.118)] for three different tilts (shown by solid, dashed and dotted lines) by varying the LP_1 angle from 20° to 70° in steps of 5°. As evident, we obtain close to 1 ebit of entanglement when LP_1 was oriented at 45°, and by tuning the orientation of LP_1 we are able to vary the polarization-spatial entanglement. This may be compared with the numerical results outlined in Fig. 3.2 (c). Further when polarizer LP_2 (at 45°) was inserted after the PBS the estimated entanglement was close to zero for varying LP_1 orientation [see Fig. 3.4 (c)].

3.5 Concluding remarks

To conclude, we have outlined a method to detect polarization-spatial entanglement in coherent vectorial paraxial light fields using fringe movement, through rotation of a linear polarizer. The fringe movement is shown to be a sufficient criteria for polarization-spatial entanglement in coherent paraxial vectorial light fields. We have experimentally shown that it is indeed possible to obtain close to 1 ebit of polarization-spatial entanglement purely with Gaussian spatial modes in orthogonal states of polarization even though the spatial modes overlap in a significant manner. We have also demonstrated tunable polarization-spatial Gaussian entanglement by varying the polarization of the input to the folded Mach-Zehnder interferometer. We believe the obtained results will be of definite consequence to several applications wherein there is requirement for maximal entanglement, which we have generated without using higher order spatial modes.

Chapter 4

Polarization-spatial Gaussian entanglement in partially coherent light fields

4.1 Introduction

In this chapter we address the problem of bipartite entanglement in $2 \times \infty$ dimensional systems. That is, qubit-harmonic oscillator mode Gaussian entanglement as may be read in the context of quantum mechanical systems, or equivalently, polarization-spatial Gaussian entanglement as may be read in the polarization wave optics context. We settle the issue of separability for a class of states with polarization-spatial degrees of freedom, with the spatial part being Gaussian. Partial transpose is shown to be necessary and sufficient in detecting entanglement. Partial transpose is implemented by introducing a generalized uncertainty principle suited for the present context. An experimental realization of such entangled states using classical optical interferometry is outlined.

The parallel that exists between qubit-harmonic oscillator mode systems and polarization wave optics is appreciated given the isomorphic relationship that exists, firstly between a qubit and a polarization state [86, 119], and secondly between a single quantum harmonic oscillator mode and a symmetric paraxial first-order optical system [79, 80]. While qubit-harmonic oscillator mode systems are quantum, polarization wave optics is classical. Qubit-harmonic oscillator mode systems are well explored, and with several applications (see for instance, Refs. [16–20, 120–126]). In Ref. [20], entanglement in such a system was demonstrated using a Bell-type inequality. Implementability of quantum operations in such systems was discussed in Refs. [16,18], and the thermodynamic aspects were explored in Refs. [17, 19]. Similarly, in Refs. [121–123] hybrid entanglement in such systems was explored. The entanglement so generated was deemed hybrid since the oscillator mode was classical, but the combined system was quantum. This may be contradistincted

with polarization-spatial entanglement which is purely classical. Polarization-spatial entanglement is well explored and with several applications [6, 7, 27, 29, 30, 37, 38, 45–47, 127–129]. For instance, it has found application in encoding information for optical communication [6, 7, 37, 38, 127–129]. Further, polarization-spatial entanglement helped resolve a long standing problem in classical optics [45].

While the present problem can be addressed using either of quantum or classical optics terminology, we prescribe to the classical wave optics approach. In what follows we assume that polarization gadgets and first-order optical systems act locally on the polarization and spatial degrees of freedom respectively, as can be done without loss of generality in the paraxial limit [130, 131].

The chapter is organized as follows. In Section 4.2, we introduce the class of states, for which, we study the separability problem. The partial transpose is implemented through the generalized uncertainty principle. The central result of the work discussed in this chapter is outlined here. In Section 4.3, we discuss the experimental realization of the studied entangled states using classical optical interferometry. We finally end with some concluding remarks in Section 4.4.

4.2 Partial coherence and polarization-spatial Gaussian entanglement

A partially coherent vector light field having Gaussian cross-spectral density $\hat{\mathbf{\Gamma}}_G$ is given by [see Eq. (2.104)]

$$\hat{\mathbf{\Gamma}}_G = |\eta\rangle\langle\eta| \otimes \hat{\Gamma}_G, \tag{4.1}$$

where $|\eta\rangle$ is a polarization state and $\hat{\Gamma}_G$ is a Gaussian cross-spectral density operator. We may recall from Section 2.11.2 that the generalized uncertainty principle is

$$\text{tr}(\hat{m}_v \hat{m}_v^\dagger \hat{\mathbf{\Gamma}}_G) \geq 0. \tag{4.2}$$

Consider the action of a polarization-conditional Gaussian unitary transformation $\hat{U}_{12}$ which implements the Gaussian unitary $\hat{U}_1$ on the spatial degree of freedom when state of polarization is $|0\rangle$, and implements the Gaussian unitary $\hat{U}_2$ on the spatial degree of freedom

when state of polarization is $|1\rangle$, that is

$$\hat{U}_{12} = |0\rangle\langle 0| \otimes \hat{U}_1 + |1\rangle\langle 1| \otimes \hat{U}_2 = \begin{bmatrix} \hat{U}_1 & 0 \\ 0 & \hat{U}_2 \end{bmatrix} \tag{4.3}$$

on $\hat{\mathbf{\Gamma}}_G$. We obtain

$$\begin{aligned} \hat{\mathbf{\Gamma}}_{U_{12}} &= \hat{U}_{12}\left(|\eta\rangle\langle\eta| \otimes \hat{\Gamma}_G\right)\hat{U}_{12}^\dagger \\ &= \begin{bmatrix} \hat{U}_1 & 0 \\ 0 & \hat{U}_2 \end{bmatrix} \begin{bmatrix} |c_0|^2\hat{\Gamma}_G & c_0c_1^*\hat{\Gamma}_G \\ c_1c_0^*\hat{\Gamma}_G & |c_1|^2\hat{\Gamma}_G \end{bmatrix} \begin{bmatrix} \hat{U}_1^\dagger & 0 \\ 0 & \hat{U}_2^\dagger \end{bmatrix} \\ &= \begin{bmatrix} |c_0|^2\hat{U}_1\hat{\Gamma}_G\hat{U}_1^\dagger & c_0c_1^*\hat{U}_1\hat{\Gamma}_G\hat{U}_2^\dagger \\ c_1c_0^*\hat{U}_2\hat{\Gamma}_G\hat{U}_1^\dagger & |c_1|^2\hat{U}_2\hat{\Gamma}_G\hat{U}_2^\dagger \end{bmatrix}. \end{aligned} \tag{4.4}$$

As evident, the action of $\hat{U}_{12}$ is generically not local and can generate entanglement between the polarization and spatial degrees of freedom. The goal here is to characterize bipartite entanglement in $\hat{\mathbf{\Gamma}}_{U_{12}}$ across the polarization-spatial divide.

Before proceeding further, we have the following observations regarding a polarization-conditional Gaussian unitary transformation $\hat{U}_{12}$. First, it is very much within the scope of physical realizability in quantum systems, see for instance Refs. [16–19, 120, 124–126]. Second, it is readily realized in classical optics using PBSs, mirrors, and lenses as outlined in Fig. (4.1). See Section 4.3 for detailed discussion.

Now proceeding further, consider the case where $\hat{U}_1 = \hat{U}_0^{-1}$ and $\hat{U}_2 = \hat{U}_{\mathcal{R}_\theta}\hat{U}_0^{-1}$. Here $\hat{U}_{\mathcal{R}_\theta} = \mathrm{e}^{\frac{-i\theta}{2}\left(c\hat{x}^2 + \frac{\kappa^2}{c}\hat{p}_x^2 - 1\right)}$. The symplectic ray transfer matrix $\mathcal{R}_\theta$ corresponding to $\hat{U}_{\mathcal{R}_\theta}$ is given by

$$\mathcal{R}_\theta = \begin{bmatrix} \cos\theta & \frac{\kappa}{c}\sin\theta \\ -\frac{c}{\kappa}\sin\theta & \cos\theta \end{bmatrix}. \tag{4.5}$$

Note that the variance matrix V_{sc} is invariant under the action of $\mathcal{R}_\theta$, that is,

$$\mathcal{R}_\theta V_{sc}\mathcal{R}_\theta^{\mathrm{T}} = V_{sc}. \tag{4.6}$$

On substituting $\hat{U}_1 = \hat{U}_0^{-1}$ and $\hat{U}_2 = \hat{U}_{\mathcal{R}_\theta}\hat{U}_0^{-1}$ in Eq. (4.4) and by making use of Eqs. (2.92)

and (2.95), we obtain

$$\hat{\mathbf{\Gamma}}_{U_{12}} = \sum_m \lambda_m \left(|\alpha_m\rangle\langle\alpha_m| \otimes |m\rangle\langle m| \right), \text{ where} \tag{4.7}$$

$$|\alpha_m\rangle = c_0|0\rangle + c_1 \mathrm{e}^{im\theta}|1\rangle, \tag{4.8}$$

and $|m\rangle$ is the Fock state [see Eq. (2.67)]. Note that, when $\theta = \pi$ and $c_0 = c_1 = \frac{1}{\sqrt{2}}$, in the above equation, we recover the cross-spectral density operator considered in Ref. [99]. Evidently for the choice of $\hat{U}_1 = \hat{U}_0^{-1}$ and $\hat{U}_2 = \hat{U}_{\mathcal{R}_\theta}\hat{U}_0^{-1}$ the cross-spectral density operator $\hat{\mathbf{\Gamma}}_{U_{12}}$ is separable, in the polarization-spatial degrees of freedom. We now proceed to analyze the situation when the Gaussian unitaries $\hat{U}_1$ and $\hat{U}_2$ are more general.

Assuming $\hat{U} = (\hat{U}_1\hat{U}_0)^{-1}\hat{U}_2\hat{U}_0$, it can be readily seen that the separability of $\hat{\mathbf{\Gamma}}_{U_{12}}$ is equivalent to the separability of $\hat{\mathbf{\Gamma}}_U$ given by

$$\begin{aligned}\hat{\mathbf{\Gamma}}_U &= \begin{bmatrix} 1 & 0 \\ 0 & \hat{U} \end{bmatrix} \begin{bmatrix} |c_0|^2\hat{\Gamma}_{sc} & c_0c_1^*\hat{\Gamma}_{sc} \\ c_1c_0^*\hat{\Gamma}_{sc} & |c_1|^2\hat{\Gamma}_{sc} \end{bmatrix} \begin{bmatrix} 1 & 0 \\ 0 & \hat{U}^\dagger \end{bmatrix} \\ &= \begin{bmatrix} |c_0|^2\hat{\Gamma}_{sc} & c_0c_1^*\hat{\Gamma}_{sc}\hat{U}^\dagger \\ c_1c_0^*\hat{U}\hat{\Gamma}_{sc} & |c_1|^2\hat{U}\hat{\Gamma}_{sc}\hat{U}^\dagger \end{bmatrix},\end{aligned} \tag{4.9}$$

where $\hat{\mathbf{\Gamma}}_{U_{12}}$ and $\hat{\mathbf{\Gamma}}_U$ are related by conjugation of the tensor product unitary operator $(|0\rangle\langle 0| + |1\rangle\langle 1|) \otimes \hat{U}_1\hat{U}_0$. That is,

$$\begin{aligned}\begin{bmatrix} \hat{U}_1\hat{U}_0 & 0 \\ 0 & \hat{U}_1\hat{U}_0 \end{bmatrix} \hat{\mathbf{\Gamma}}_U \begin{bmatrix} \hat{U}_0^\dagger\hat{U}_1^\dagger & 0 \\ 0 & \hat{U}_0^\dagger\hat{U}_1^\dagger \end{bmatrix} &= \begin{bmatrix} |c_0|^2\hat{U}_1\hat{U}_0\hat{\Gamma}_{sc}\hat{U}_0^\dagger\hat{U}_1^\dagger & c_0c_1^*\hat{U}_1\hat{U}_0\hat{\Gamma}_{sc}\hat{U}_0^\dagger\hat{U}_2^\dagger \\ c_1c_0^*\hat{U}_2\hat{U}_0\hat{\Gamma}_{sc}\hat{U}_0^\dagger\hat{U}_1^\dagger & |c_1|^2\hat{U}_2\hat{U}_0\hat{\Gamma}_{sc}\hat{U}_0^\dagger\hat{U}_2^\dagger \end{bmatrix} \\ &= \hat{\mathbf{\Gamma}}_{U_{12}},\end{aligned} \tag{4.10}$$

since $\hat{\Gamma}_G \equiv \hat{U}_0\hat{\Gamma}_{sc}\hat{U}_0^\dagger$ by Eq. (2.95). On taking partial transpose on $\hat{\mathbf{\Gamma}}_U$ we obtain

$$\hat{\mathbf{\Gamma}}_U^{\text{PT}} = \begin{bmatrix} |c_0|^2\hat{\Gamma}_{sc} & c_0c_1^*\hat{U}^*\hat{\Gamma}_{sc} \\ c_1c_0^*\hat{\Gamma}_{sc}\hat{U}^{\text{T}} & |c_1|^2\hat{U}^*\hat{\Gamma}_{sc}\hat{U}^{\text{T}} \end{bmatrix}. \tag{4.11}$$

Note that, here we have made use of the fact that $\hat{\Gamma}_{sc} = \hat{\Gamma}_{sc}^{\text{T}}$. Since conjugation does not affect the positivity of a matrix operator, positivity of $\hat{\mathbf{\Gamma}}_U^{\text{PT}}$ is same as positivity of $\hat{\mathbf{\Gamma}}_{U_c}^{\text{PT}}$, where

$\hat{\mathbf{\Gamma}}^{\text{PT}}_{U_c} = \left(\frac{1}{c_0}|0\rangle\langle 0| \otimes \mathbb{1} + \frac{1}{c_1}|1\rangle\langle 1| \otimes \hat{U}^*\right) \hat{\mathbf{\Gamma}}^{\text{PT}}_{U} \left(\frac{1}{c_0^*}|0\rangle\langle 0| \otimes \mathbb{1} + \frac{1}{c_1^*}|1\rangle\langle 1| \otimes \hat{U}^{\text{T}}\right)$, that is,

$$\hat{\mathbf{\Gamma}}^{\text{PT}}_{U_c} = \begin{bmatrix} \frac{1}{c_0} & 0 \\ 0 & \frac{1}{c_1}\hat{U}^* \end{bmatrix} \hat{\mathbf{\Gamma}}^{\text{PT}}_{U} \begin{bmatrix} \frac{1}{c_0^*} & 0 \\ 0 & \frac{1}{c_1^*}\hat{U}^{\text{T}} \end{bmatrix} = \begin{bmatrix} \hat{\Gamma}_{sc} & \hat{U}^*\hat{\Gamma}_{sc}\hat{U}^{\text{T}} \\ \hat{U}^*\hat{\Gamma}_{sc}\hat{U}^{\text{T}} & \hat{U}^*\hat{U}^*\hat{\Gamma}_{sc}\hat{U}^{\text{T}}\hat{U}^{\text{T}} \end{bmatrix}. \tag{4.12}$$

If $\hat{\mathbf{\Gamma}}_{U_{12}}$ is separable, then we have

$$\text{tr}(\hat{m}_v\hat{m}_v^\dagger\hat{\mathbf{\Gamma}}^{\text{PT}}_{U}) \geq 0 \iff \text{tr}(\hat{m}_v\hat{m}_v^\dagger\hat{\mathbf{\Gamma}}^{\text{PT}}_{U_c}) \geq 0. \tag{4.13}$$

By making use of Eq. (2.89) and (2.106), the inequality in (4.13) (the uncertainty principle corresponding to $\hat{\mathbf{\Gamma}}^{\text{PT}}_{U_c}$) can be rewritten as

$$\begin{bmatrix} V_{sc} + \frac{i}{2\kappa}\Omega & \tilde{S}V_{sc}\tilde{S}^{\text{T}} + \frac{i}{2\kappa}\Omega \\ \tilde{S}V_{sc}\tilde{S}^{\text{T}} + \frac{i}{2\kappa}\Omega & \tilde{S}^2V_{sc}\tilde{S}^{2^{\text{T}}} + \frac{i}{2\kappa}\Omega \end{bmatrix} \geq 0, \tag{4.14}$$

where $\tilde{S}$ is the symplectic ray transfer matrix corresponding to the Gaussian unitary $\hat{U}^*$. If the inequality in (4.14) is not satisfied, then $\hat{\mathbf{\Gamma}}_{U_{12}}$ is entangled in the polarization-spatial degrees of freedom.

By Euler decomposition a general symplectic ray transfer matrix $\tilde{S}$ can be written as [80]

$$\tilde{S} = \mathcal{R}_{\theta_1}\mathbf{\Lambda}\mathcal{R}_{\theta_2}, \tag{4.15}$$

where $\mathcal{R}_\theta$ is as defined by Eq. (4.5) and $\mathbf{\Lambda}$ is defined as $\mathbf{\Lambda} = \text{diag}(\Lambda, 1/\Lambda)$. On substituting Eq. (4.15) in (4.14) and by making use of Eq. (4.6), we obtain

$$\begin{bmatrix} V_{sc} + \frac{i}{2\kappa}\Omega & \mathcal{R}_{\theta_1}\mathbf{\Lambda}V_{sc}\mathbf{\Lambda}\mathcal{R}_{\theta_1}^{\text{T}} + \frac{i}{2\kappa}\Omega \\ \mathcal{R}_{\theta_1}\mathbf{\Lambda}V_{sc}\mathbf{\Lambda}\mathcal{R}_{\theta_1}^{\text{T}} + \frac{i}{2\kappa}\Omega & \mathcal{R}_{\theta_1}\mathbf{\Lambda}\mathcal{R}_{\phi}\mathbf{\Lambda}V_{sc}\mathbf{\Lambda}\mathcal{R}_{\phi}^{\text{T}}\mathbf{\Lambda}\mathcal{R}_{\theta_1}^{\text{T}} + \frac{i}{2\kappa}\Omega \end{bmatrix} \geq 0, \tag{4.16}$$

where $\mathcal{R}_\phi = \mathcal{R}_{\theta_2}\mathcal{R}_{\theta_1},$ and $\phi = \theta_1 + \theta_2$. The inequality (4.16) can be rewritten as

$$\begin{bmatrix} \mathcal{R}_{\theta_1} & 0 \\ 0 & \mathcal{R}_{\theta_1} \end{bmatrix} \begin{bmatrix} V_{sc} + \frac{i}{2\kappa}\Omega & \mathbf{\Lambda}V_{sc}\mathbf{\Lambda} + \frac{i}{2\kappa}\Omega \\ \mathbf{\Lambda}V_{sc}\mathbf{\Lambda} + \frac{i}{2\kappa}\Omega & \mathbf{\Lambda}\mathcal{R}_{\phi}\mathbf{\Lambda}V_{sc}\mathbf{\Lambda}\mathcal{R}_{\phi}^{\text{T}}\mathbf{\Lambda} + \frac{i}{2\kappa}\Omega \end{bmatrix} \begin{bmatrix} \mathcal{R}_{\theta_1}^{\text{T}} & 0 \\ 0 & \mathcal{R}_{\theta_1}^{\text{T}} \end{bmatrix} \geq 0, \tag{4.17}$$

which is equivalent to

$$\begin{bmatrix} V_{sc} + \frac{i}{2\kappa}\Omega & \mathbf{\Lambda} V_{sc} \mathbf{\Lambda} + \frac{i}{2\kappa}\Omega \\ \mathbf{\Lambda} V_{sc} \mathbf{\Lambda} + \frac{i}{2\kappa}\Omega & \mathbf{\Lambda}\mathcal{R}_\phi \mathbf{\Lambda} V_{sc} \mathbf{\Lambda} \mathcal{R}_\phi^{\mathrm{T}} \mathbf{\Lambda} + \frac{i}{2\kappa}\Omega \end{bmatrix} \equiv \begin{bmatrix} \mathbf{A} & \mathbf{B} \\ \mathbf{C} & \mathbf{D} \end{bmatrix} \geq 0. \tag{4.18}$$

Demanding positivity of the LHS of (4.18) is equivalent to demanding positivity of its Schur compliment [132], that is,

$$\mathbf{D} - \mathbf{C}\mathbf{A}^{-1}\mathbf{B} \geq 0. \tag{4.19}$$

We have,

$$\begin{aligned} \mathbf{D} &= \mathbf{\Lambda}\mathcal{R}_\phi \mathbf{\Lambda} V_{sc} \mathbf{\Lambda} \mathcal{R}_\phi^{\mathrm{T}} \mathbf{\Lambda} + \frac{i}{2\kappa}\Omega \\ &= \begin{bmatrix} a\left[\Lambda^4 + \sin^2\phi(1-\Lambda^4)\right] & \frac{ac}{\kappa\Lambda^2}\sin\phi\cos\phi(1-\Lambda^4) + \frac{i}{2\kappa} \\ \frac{b\kappa}{c\Lambda^2}\sin\phi\cos\phi(1-\Lambda^4) - \frac{i}{2\kappa} & \frac{b}{\Lambda^4}\left[1 - \sin^2\phi(1-\Lambda^4)\right] \end{bmatrix}, \text{ and} \end{aligned} \tag{4.20}$$

$$\begin{aligned} \mathbf{C}\mathbf{A}^{-1}\mathbf{B} &= \frac{1}{ab - \frac{1}{4\kappa^2}} \begin{bmatrix} a\Lambda^2 & \frac{i}{2\kappa} \\ -\frac{i}{2\kappa} & \frac{b}{\Lambda^2} \end{bmatrix} \begin{bmatrix} b & -\frac{i}{2\kappa} \\ \frac{i}{2\kappa} & a \end{bmatrix} \begin{bmatrix} a\Lambda^2 & \frac{i}{2\kappa} \\ -\frac{i}{2\kappa} & \frac{b}{\Lambda^2} \end{bmatrix} \\ &= \frac{1}{ab - \frac{1}{4\kappa^2}} \begin{bmatrix} a\left[ab\Lambda^4 - \frac{\Lambda^2}{2\kappa^2} + \frac{1}{4\kappa^2}\right] & \frac{i}{2\kappa}\left[ab\left(\Lambda^2 + \frac{1}{\Lambda^2}\right) - ab - \frac{1}{4\kappa^2}\right] \\ -\frac{i}{2\kappa}\left[ab\left(\Lambda^2 + \frac{1}{\Lambda^2}\right) - ab - \frac{1}{4\kappa^2}\right] & b\left[\frac{1}{4\kappa^2} - \frac{1}{2\kappa^2\Lambda^2} + \frac{ab}{\Lambda^4}\right] \end{bmatrix}. \end{aligned} \tag{4.21}$$

Performing the necessary algebra and demanding the positivity of the lower diagonal entry of the Schur compliment reduces to

$$\begin{aligned} \frac{b}{\Lambda^4}\left[1 - \sin^2\phi(1-\Lambda^4)\right] - \frac{b}{ab - \frac{1}{4\kappa^2}}\left[\frac{1}{4\kappa^2} - \frac{1}{2\kappa^2\Lambda^2} + \frac{ab}{\Lambda^4}\right] &\geq 0 \\ -\frac{\mathrm{c}(1+q)(1-\Lambda^4)\sin^2\phi}{2\kappa^2\Lambda^4(1-q)} - \frac{\mathrm{c}(1-q^2)(1-\Lambda^2)^2}{8\kappa^2\Lambda^4 q} &\geq 0. \end{aligned} \tag{4.22}$$

Since both c and q are positive parameters and $0 \leq q < 1$, this is not true for $\Lambda \neq 1$. When $\Lambda = 1$, we have $\tilde{S} = \mathcal{R}_\phi$. That is, $\hat{U}^*$ considered in $\hat{\mathbf{\Gamma}}_U^{\mathrm{PT}}$ of Eq. (4.11), is $\hat{U}^* = \hat{U}_{\mathcal{R}_\phi}$. As a result, $\hat{\mathbf{\Gamma}}_U^{\mathrm{PT}}$ of Eq. (4.11) reduces to $\hat{\mathbf{\Gamma}}_{U_{12}}$ of Eq. (4.7), which is manifestly separable. We thus have :

Theorem 1 : Negativity under partial transpose is a necessary and sufficient condition to detect polarization-spatial entanglement in the cross-spectral density operator $\hat{\mathbf{\Gamma}}_{U_{12}} = \hat{U}_{12}\left(|\eta\rangle\langle\eta| \otimes \hat{\Gamma}_G\right)\hat{U}_{12}^\dagger$, where $\hat{U}_{12} = |0\rangle\langle 0| \otimes \hat{U}_1 + |1\rangle\langle 1| \otimes \hat{U}_2$ is a polarization-conditional

Gaussian unitary transformation, with $\hat{U}_1$ and $\hat{U}_2$ to be Gaussian unitaries generated by quadratic Hamiltonians.

The following remark is in order concerning Theorem 1. While every Gaussian cross-spectral density $\hat{\Gamma}_G$ is completely specified by its variance matrix V_G, every cross-spectral density $\hat{\Gamma}$ possesses a variance matrix denoted by V which obeys the uncertainty principle as in (2.86), and can be brought to diagonal form (V_{sc}) as in Eq. (2.96). Consequently, the test for polarization-spatial entanglement as contained in (4.14) - (4.22) holds, and violation of the inequality in (4.22) is a sufficient criterion for polarization-spatial entanglement in the cross-spectral density operator of the form $\hat{\mathbf{\Gamma}}_{U_{12}} = \hat{U}_{12}\left(|\eta\rangle\langle\eta| \otimes \hat{\Gamma}\right)\hat{U}_{12}^{\dagger}$.

Let us now move on to the situation when the polarization-conditional Gaussian unitaries $\hat{U}_1$ and $\hat{U}_2$ of $\hat{U}_{12}$ include translations as well. That is, the polarization-conditional Gaussian unitary can now be written as

$$\hat{\mathcal{U}}_{12} = |0\rangle\langle 0| \otimes \hat{\mathcal{U}}_1 + |1\rangle\langle 1| \otimes \hat{\mathcal{U}}_2 = \begin{bmatrix} \hat{\mathcal{U}}_1 & 0 \\ 0 & \hat{\mathcal{U}}_2 \end{bmatrix}, \tag{4.23}$$

where $\hat{\mathcal{U}}_1$ and $\hat{\mathcal{U}}_2$ are of the form [see Eq. (2.68)]

$$\hat{\mathcal{U}}_1 \equiv \hat{\mathcal{U}}_1(S_1, \mathbf{d}_1) = \hat{D}(\mathbf{d}_1)\hat{U}(S_1), \text{ and } \hat{\mathcal{U}}_2 \equiv \hat{\mathcal{U}}_2(S_2, \mathbf{d}_2) = \hat{D}(\mathbf{d}_2)\hat{U}(S_2). \tag{4.24}$$

We are interested in detecting bipartite entanglement in the state $\hat{\mathbf{\Gamma}}_{\mathcal{U}_{12}}$ given by

$$\hat{\mathbf{\Gamma}}_{\mathcal{U}_{12}} = \hat{\mathcal{U}}_{12}\left(|\eta\rangle\langle\eta| \otimes \hat{\Gamma}_G\right)\hat{\mathcal{U}}_{12}^{\dagger}, \tag{4.25}$$

where $\hat{\mathcal{U}}_1$ and $\hat{\mathcal{U}}_2$ are as given in (4.24). The generalized uncertainty principle suited for the present context is discussed in Section 2.11.2, and can be recalled as

$$\text{tr}(\hat{m}_c\hat{m}_c^{\dagger}\hat{\mathbf{\Gamma}}_G) \geq 0. \tag{4.26}$$

Without loss of generality we can assume that the initial state $\hat{\Gamma}_G$ in Eq. (4.25) is centered (zero displacement), i.e., $\hat{\mathcal{U}}_0 = \hat{U}(S_0)$ [see Eq. (2.95)]. As in the previous situation, to detect entanglement, we implement partial transpose using the procedure outlined in Eqs. (4.9) - (4.12). We need to check if

$$\text{tr}(\hat{m}_c\hat{m}_c^{\dagger}\hat{\mathbf{\Gamma}}_{\mathcal{U}_c}^{\text{PT}}) \geq 0, \tag{4.27}$$

where $\hat{\mathbf{\Gamma}}^{\text{PT}}_{\mathcal{U}_c}$ can now be written as

$$\hat{\mathbf{\Gamma}}^{\text{PT}}_{\mathcal{U}_c} = \begin{bmatrix} \frac{1}{c_0} & 0 \\ 0 & \frac{1}{c_1}\hat{\mathcal{U}}^* \end{bmatrix} \hat{\mathbf{\Gamma}}^{\text{PT}}_{\mathcal{U}} \begin{bmatrix} \frac{1}{c_0^*} & 0 \\ 0 & \frac{1}{c_1^*}\hat{\mathcal{U}}^{\text{T}} \end{bmatrix} = \begin{bmatrix} \hat{\Gamma}_{sc} & \hat{\mathcal{U}}^*\hat{\Gamma}_{sc}\hat{\mathcal{U}}^{\text{T}} \\ \hat{\mathcal{U}}^*\hat{\Gamma}_{sc}\hat{\mathcal{U}}^{\text{T}} & \hat{\mathcal{U}}^*\hat{\mathcal{U}}^*\hat{\Gamma}_{sc}\hat{\mathcal{U}}^{\text{T}}\hat{\mathcal{U}}^{\text{T}} \end{bmatrix}. \tag{4.28}$$

The unitary transformation $\hat{U}^*$ in Eq. (4.12) is now given by

$$\begin{aligned} \hat{\mathcal{U}}^* &= \left[\hat{\mathcal{U}}_1^*(S_1, \mathbf{d}_1)\hat{U}^*(S_0)\right]^{-1} \hat{\mathcal{U}}_2^*(S_2, \mathbf{d}_2)\hat{U}^*(S_0) \\ &= \left(\hat{D}^*(\mathbf{d}_1)\hat{U}^*(S_1)\hat{U}^*(S_0)\right)^{-1} \hat{D}^*(\mathbf{d}_2)\hat{U}^*(S_2)\hat{U}^*(S_0) \\ &= \hat{U}^*(S_0^{-1})\hat{U}^*(S_1^{-1})\hat{D}^*(\mathbf{d}_1^{-1})\hat{D}^*(\mathbf{d}_2)\hat{U}^*(S_2)\hat{U}^*(S_0). \end{aligned} \tag{4.29}$$

Using the fact that $\hat{\mathcal{U}}(S, \mathbf{d})$ form a semi-group [133], and by denoting $D^*(\mathbf{d}) \equiv D(\tilde{\mathbf{d}})$ and $U^*(S) \equiv U(\tilde{S})$, the unitary composition outlined in Eq. (4.29) can be carried out and we obtain

$$\begin{aligned} \hat{\mathcal{U}}^{\text{T}}\hat{\xi}\hat{\mathcal{U}}^* =& \hat{U}^{\text{T}}(S_0)\hat{U}^{\text{T}}(S_2)\hat{D}^{\text{T}}(\mathbf{d}_2)\hat{D}^{\text{T}}(\mathbf{d}_1^{-1})\hat{U}^{\text{T}}(S_1^{-1})\hat{U}^{\text{T}}(S_0^{-1})\hat{\xi}\hat{U}^*(S_0^{-1})\hat{U}^*(S_1^{-1}) \\ & \hat{D}^*(\mathbf{d}_1^{-1})\hat{D}^*(\mathbf{d}_2)\hat{U}^*(S_2)\hat{U}^*(S_0) \\ =& \tilde{S}_0^{-1}\tilde{S}_1^{-1}\tilde{S}_2\tilde{S}_0\hat{\xi} + \tilde{S}_0^{-1}\tilde{S}_1^{-1}\left(\tilde{\mathbf{d}}_2 - \tilde{\mathbf{d}}_1\right) \equiv \tilde{S}\hat{\xi} + \mathbf{d}', \quad \text{and} \end{aligned} \tag{4.30}$$

$$\begin{aligned} \hat{\mathcal{U}}^{\text{T}}\hat{\mathcal{U}}^{\text{T}}\hat{\xi}\hat{\mathcal{U}}^*\hat{\mathcal{U}}^* =& \hat{U}^{\text{T}}(S_0)\hat{U}^{\text{T}}(S_2)\hat{D}^{\text{T}}(\mathbf{d}_2)\hat{D}^{\text{T}}(\mathbf{d}_1^{-1})\hat{U}^{\text{T}}(S_1^{-1})\hat{U}^{\text{T}}(S_0^{-1})\tilde{S}\hat{\xi}\hat{U}^*(S_0^{-1})\hat{U}^*(S_1^{-1}) \\ & \hat{D}^*(\mathbf{d}_1^{-1})\hat{D}^*(\mathbf{d}_2)\hat{U}^*(S_2)\hat{U}^*(S_0) + \mathbf{d}' \\ =& \tilde{S}\tilde{S}_0^{-1}\tilde{S}_1^{-1}\tilde{S}_2\tilde{S}_0\hat{\xi} + \tilde{S}\tilde{S}_0^{-1}\tilde{S}_1^{-1}\tilde{\mathbf{d}}_2 - \tilde{S}\tilde{S}_0^{-1}\tilde{S}_1^{-1}\tilde{\mathbf{d}}_1 + \mathbf{d}' \equiv \tilde{S}^2\hat{\xi} + \mathbf{d}''. \end{aligned} \tag{4.31}$$

Note that, here

$$\tilde{S} = \tilde{S}_0^{-1}\tilde{S}_1^{-1}\tilde{S}_2\tilde{S}_0, \tag{4.32}$$

$$\mathbf{d}' = \tilde{S}_0^{-1}\tilde{S}_1^{-1}\left(\tilde{\mathbf{d}}_2 - \tilde{\mathbf{d}}_1\right), \quad \text{and} \tag{4.33}$$

$$\mathbf{d}'' = \tilde{S}_0^{-1}\tilde{S}_1^{-1}\tilde{S}_2\tilde{S}_1^{-1}\left(\tilde{\mathbf{d}}_2 - \tilde{\mathbf{d}}_1\right) + \tilde{S}_0^{-1}\tilde{S}_1^{-1}\left(\tilde{\mathbf{d}}_2 - \tilde{\mathbf{d}}_1\right), \quad \text{with} \tag{4.34}$$

$$\tilde{\mathbf{d}}_i = \sigma_3\mathbf{d}_i, \quad \text{and } i = 1, 2, \tag{4.35}$$

where σ_3 is the Pauli matrix. By making use of Eqs. (4.28) - (4.31) and the inequality given in (2.108), the inequality in (4.27) (the uncertainty principle corresponding to $\hat{\mathbf{\Gamma}}^{\text{PT}}_{\mathcal{U}_c}$) can be

rewritten in block form as

$$\mathbf{M}=\left[\begin{array}{ccc|ccc} 1 & \vdots & \mathbf{0}^{\mathrm{T}} & 1 & \vdots & \mathbf{d}'^{\mathrm{T}} \\ \cdots & & \cdots & \cdots & & \cdots \\ \mathbf{0} & \vdots & V_{sc}+\frac{i}{2\kappa}\Omega & \mathbf{d}' & \vdots & \tilde{S}V_{sc}\tilde{S}^{\mathrm{T}}+\frac{i}{2\kappa}\Omega+\mathbf{d}'\mathbf{d}'^{\mathrm{T}} \\ \hline 1 & \vdots & \mathbf{d}'^{\mathrm{T}} & 1 & \vdots & \mathbf{d}''^{\mathrm{T}} \\ \cdots & & \cdots & \cdots & & \cdots \\ \mathbf{d}' & \vdots & \tilde{S}V_{sc}\tilde{S}^{\mathrm{T}}+\frac{i}{2\kappa}\Omega+\mathbf{d}'\mathbf{d}'^{\mathrm{T}} & \mathbf{d}'' & \vdots & \tilde{S}^{2}V_{sc}\tilde{S}^{2^{\mathrm{T}}}+\frac{i}{2\kappa}\Omega+\mathbf{d}''\mathbf{d}''^{\mathrm{T}} \end{array}\right]\geq 0, \quad (4.36)$$

where $\mathbf{0}=[0,0]^{\mathrm{T}}$. Substituting for $\left(V_{sc}+\frac{i}{2\kappa}\Omega\right)$ from (2.94), and denoting $\mathbf{d}'\equiv\left[\frac{\delta_1'}{\sqrt{c}},\frac{\delta_2'\sqrt{c}}{\kappa}\right]^{\mathrm{T}}$ and $\mathbf{d}''\equiv\left[\frac{\delta_1''}{\sqrt{c}},\frac{\delta_2''\sqrt{c}}{\kappa}\right]^{\mathrm{T}}$, the above inequality can be explicitly written as

$$\mathbf{M}=\left[\begin{array}{ccc|ccc} 1 & 0 & 0 & 1 & \frac{\delta_1'}{\sqrt{c}} & \frac{\delta_2'\sqrt{c}}{\kappa} \\ 0 & a & \frac{i}{2\kappa} & \frac{\delta_1'}{\sqrt{c}} & \alpha+\frac{\delta_1'^2}{c} & \beta+\frac{\delta_1'\delta_2'}{\kappa} \\ 0 & -\frac{i}{2\kappa} & b & \frac{\delta_2'\sqrt{c}}{\kappa} & \beta^*+\frac{\delta_1'\delta_2'}{\kappa} & \gamma+\frac{\delta_2'^2c}{\kappa^2} \\ \hline 1 & \frac{\delta_1'}{\sqrt{c}} & \frac{\delta_2'\sqrt{c}}{\kappa} & 1 & \frac{\delta_1''}{\sqrt{c}} & \frac{\delta_2''\sqrt{c}}{\kappa} \\ \frac{\delta_1'}{\sqrt{c}} & \alpha+\frac{\delta_1'^2}{c} & \beta+\frac{\delta_1'\delta_2'}{\kappa} & \frac{\delta_1''}{\sqrt{c}} & \alpha'+\frac{\delta_1''^2}{c} & \beta'+\frac{\delta_1''\delta_2''}{\kappa} \\ \frac{\delta_2'\sqrt{c}}{\kappa} & \beta^*+\frac{\delta_1'\delta_2'}{\kappa} & \gamma+\frac{\delta_2'^2c}{\kappa^2} & \frac{\delta_2''\sqrt{c}}{\kappa} & \beta'^*+\frac{\delta_1''\delta_2''}{\kappa} & \gamma'+\frac{\delta_2''^2c}{\kappa^2} \end{array}\right]\equiv\begin{bmatrix}\mathcal{A} & \mathcal{B}\\ \mathcal{C} & \mathcal{D}\end{bmatrix}\geq 0, \quad (4.37)$$

where,

$$\begin{bmatrix}\alpha & \beta\\ \beta^* & \gamma\end{bmatrix}\equiv\tilde{S}V_{sc}\tilde{S}^{\mathrm{T}}+\frac{i}{2\kappa}\Omega, \quad \text{and} \quad \begin{bmatrix}\alpha' & \beta'\\ \beta'^* & \gamma'\end{bmatrix}\equiv\tilde{S}^{2}V_{sc}\tilde{S}^{2^{\mathrm{T}}}+\frac{i}{2\kappa}\Omega. \quad (4.38)$$

If the inequality in (4.37) is not satisfied, then $\hat{\mathbf{\Gamma}}_{U_{12}}$ is entangled in the polarization-spatial degrees of freedom. Now to explicitly determine the positivity of $\mathbf{M}$, we evaluate the Schur complement of $\mathbf{M}$. There are two situations that arise here, first, V_{sc} does not saturate the uncertainty principle in (2.94), i.e., $ab-\frac{1}{4\kappa^2}>0$, and second, V_{sc} saturates the uncertainty principle, i.e., $ab-\frac{1}{4\kappa^2}=0$. Performing the Schur complement of $\mathbf{M}$ and demanding the positivity of its $(1,1)^{\text{th}}$ element reduces to

$$\mathcal{D}(1,1)-(\mathcal{C}\mathcal{A}^{-1}\mathcal{B})(1,1)\geq 0. \quad (4.39)$$

For $ab-\frac{1}{4\kappa^2}>0$, we have

$$\mathcal{C}\mathcal{A}^{-1}\mathcal{B}=\begin{bmatrix} 1 & \frac{\delta_1'}{\sqrt{c}} & \frac{\delta_2'\sqrt{c}}{\kappa} \\ \frac{\delta_1'}{\sqrt{c}} & \alpha+\frac{\delta_1'^2}{c} & \beta+\frac{\delta_1'\delta_2'}{\kappa} \\ \frac{\delta_2'\sqrt{c}}{\kappa} & \beta^*+\frac{\delta_1'\delta_2'}{\kappa} & \gamma+\frac{\delta_2'^2 c}{\kappa^2} \end{bmatrix}\begin{bmatrix} 1 & 0 & 0 \\ 0 & \frac{b}{ab-\frac{1}{4\kappa^2}} & \frac{-\frac{i}{2\kappa}}{ab-\frac{1}{4\kappa^2}} \\ 0 & \frac{\frac{i}{2\kappa}}{ab-\frac{1}{4\kappa^2}} & \frac{a}{ab-\frac{1}{4\kappa^2}} \end{bmatrix}\begin{bmatrix} 1 & \frac{\delta_1'}{\sqrt{c}} & \frac{\delta_2'\sqrt{c}}{\kappa} \\ \frac{\delta_1'}{\sqrt{c}} & \alpha+\frac{\delta_1'^2}{c} & \beta+\frac{\delta_1'\delta_2'}{\kappa} \\ \frac{\delta_2'\sqrt{c}}{\kappa} & \beta^*+\frac{\delta_1'\delta_2'}{\kappa} & \gamma+\frac{\delta_2'^2 c}{\kappa^2} \end{bmatrix}. \tag{4.40}$$

The $(1,1)^{\text{th}}$ of $\mathcal{C}\mathcal{A}^{-1}\mathcal{B}$ for this situation is given by

$$\begin{aligned}(\mathcal{C}\mathcal{A}^{-1}\mathcal{B})(1,1) &= 1+\frac{\delta_1'}{\sqrt{\mathrm{c}}}\left(\frac{\frac{b\delta_1'}{\sqrt{\mathrm{c}}}-\frac{i\delta_2'\sqrt{\mathrm{c}}}{2\kappa^2}}{ab-\frac{1}{4\kappa^2}}\right)+\frac{\delta_2'\sqrt{\mathrm{c}}}{\kappa}\left(\frac{\frac{i\delta_1'}{2\kappa\sqrt{\mathrm{c}}}+\frac{a\delta_2'\sqrt{\mathrm{c}}}{\kappa}}{ab-\frac{1}{4\kappa^2}}\right) \\ &= 1+\frac{(1-q^2)\left(\delta_1'^2+\delta_2'^2\right)}{2q}.\end{aligned} \tag{4.41}$$

Thus the inequality in (4.39) can now be rewritten as

$$-\frac{(1-q^2)(\delta_1'^2+\delta_2'^2)}{2q}\geq 0. \tag{4.42}$$

For $ab-\frac{1}{4\kappa^2}=0$, we have

$$\mathcal{C}\mathcal{A}^{-1}\mathcal{B}=\begin{bmatrix} 1 & \frac{\delta_1'}{\sqrt{c}} & \frac{\delta_2'\sqrt{c}}{\kappa} \\ \frac{\delta_1'}{\sqrt{c}} & \alpha+\frac{\delta_1'^2}{c} & \beta+\frac{\delta_1'\delta_2'}{\kappa} \\ \frac{\delta_2'\sqrt{c}}{\kappa} & \beta^*+\frac{\delta_1'\delta_2'}{\kappa} & \gamma+\frac{\delta_2'^2 c}{\kappa^2} \end{bmatrix}\begin{bmatrix} 1 & 0 & 0 \\ 0 & \frac{a}{(a+b)^2} & \frac{\frac{i}{2\kappa}}{(a+b)^2} \\ 0 & \frac{-\frac{i}{2\kappa}}{(a+b)^2} & \frac{b}{(a+b)^2} \end{bmatrix}\begin{bmatrix} 1 & \frac{\delta_1'}{\sqrt{c}} & \frac{\delta_2'\sqrt{c}}{\kappa} \\ \frac{\delta_1'}{\sqrt{c}} & \alpha+\frac{\delta_1'^2}{c} & \beta+\frac{\delta_1'\delta_2'}{\kappa} \\ \frac{\delta_2'\sqrt{c}}{\kappa} & \beta^*+\frac{\delta_1'\delta_2'}{\kappa} & \gamma+\frac{\delta_2'^2 c}{\kappa^2} \end{bmatrix}. \tag{4.43}$$

The $(1,1)^{\text{th}}$ of $\mathcal{C}\mathcal{A}^{-1}\mathcal{B}$ is given by

$$\begin{aligned}(\mathcal{C}\mathcal{A}^{-1}\mathcal{B})(1,1) &= 1+\frac{\delta_1'}{\sqrt{\mathrm{c}}}\left(\frac{\frac{a\delta_1'}{\sqrt{\mathrm{c}}}+\frac{i\delta_2'\sqrt{\mathrm{c}}}{2\kappa^2}}{(a+b)^2}\right)+\frac{\delta_2'\sqrt{\mathrm{c}}}{\kappa}\left(\frac{-\frac{i\delta_1'}{2\kappa\sqrt{\mathrm{c}}}+\frac{b\delta_2'\sqrt{\mathrm{c}}}{\kappa}}{(a+b)^2}\right) \\ &= 1+\frac{2(1-q)}{1+q}\frac{(\delta_1'^2\kappa^4+\delta_2'^2\mathrm{c}^4)}{\left(\kappa^2+\mathrm{c}^2\right)^2}.\end{aligned} \tag{4.44}$$

Thus the inequality in (4.39) can now be rewritten as

$$-\frac{2(1-q)}{1+q}\frac{(\delta_1'^2\kappa^4+\delta_2'^2\mathrm{c}^4)}{\left(\kappa^2+\mathrm{c}^2\right)^2}\geq 0. \tag{4.45}$$

As evident from (4.42) and (4.45), $\mathbf{M}$ violates positivity for any non zero translation $\mathbf{d}'$, since $0 \leq q < 1$. Note that this is independent of S_1 and S_2. As evident from Eqs. (4.30) - (4.35), $\mathbf{d}'$ is non zero if and only if $\mathbf{d}_1 - \mathbf{d}_2$ is non zero. That is, for any $\hat{\mathcal{U}}_1$ and $\hat{\mathcal{U}}_2$ as in (4.24) with $\mathbf{d}_1 - \mathbf{d}_2 \neq 0$, and with $\hat{\mathcal{U}}^*$ as in Eq. (4.29), $\hat{\mathbf{\Gamma}}^{\text{PT}}_{\mathcal{U}_c}$ of Eq. (4.28) is not positive, and consequently, $\hat{\mathbf{\Gamma}}_{\mathcal{U}_{12}}$ of Eq. (4.25) is entangled. When $\mathbf{d}_1 - \mathbf{d}_2 = 0$, i.e., $\mathbf{d}' = 0$, by Eqs. (4.30) - (4.35), the positivity requirement in (4.36) reduces to the positivity requirement in (4.14), in which case, Theorem 1 holds. We have

Theorem 2 : Negativity under partial transpose is a necessary and sufficient condition to detect polarization-spatial entanglement in the cross-spectral density operator $\hat{\mathbf{\Gamma}}_{\mathcal{U}_{12}} = \hat{\mathcal{U}}_{12}$ $(|\eta\rangle\langle\eta| \otimes \hat{\Gamma}_G)\,\hat{\mathcal{U}}^{\dagger}_{12}$, where $\hat{\mathcal{U}}_{12} = |0\rangle\langle 0| \otimes \hat{\mathcal{U}}_1 + |1\rangle\langle 1| \otimes \hat{\mathcal{U}}_2$ is a polarization-conditional Gaussian unitary transformation, with $\hat{\mathcal{U}}_1$ and $\hat{\mathcal{U}}_2$ to be the most general Gaussian unitaries.

We now have the following observation. Given that every cross-spectral density $\hat{\Gamma}$ possesses a variance matrix denoted by V which obeys the uncertainty principle as in (2.86), and can be brought to diagonal form (V_{sc}) as in Eq. (2.96), we can replace $\hat{\Gamma}_G$ with $\hat{\Gamma}$ in Eq. (4.4), and the analysis in (4.26) - (4.45) goes through. We thus have

Theorem 3 : The cross-spectral density operator $\hat{\mathbf{\Gamma}}_{\mathcal{U}_{12}} = \hat{\mathcal{U}}_{12}\,(|\eta\rangle\langle\eta| \otimes \hat{\Gamma})\,\hat{\mathcal{U}}^{\dagger}_{12}$ for any cross-spectral density $\hat{\Gamma}$ is entangled for $\hat{\mathcal{U}}_1$ and $\hat{\mathcal{U}}_2$ of $\hat{\mathcal{U}}_{12}$ with $\mathbf{d}_1 - \mathbf{d}_2$ non zero.

In the situation when the polarization-spatial cross-spectral density operator is of the form

$$\hat{\mathbf{\Gamma}}_{\mathcal{U}_{12}} = \hat{\mathcal{U}}_{12}\,(\tilde{\rho}_p \otimes \hat{\Gamma})\,\hat{\mathcal{U}}^{\dagger}_{12}, \quad \text{with} \tag{4.46}$$

$$\tilde{\rho}_p = \Sigma_i \tilde{p}_i |\eta_i\rangle\langle\eta_i|, \tag{4.47}$$

a mixed state of polarization, the analysis outlined in (4.2) - (4.22) and (4.26) - (4.45) can be carried out and we obtain modified versions of (4.22) and (4.42), (4.45). We find that the modified inequalities in (4.22) and (4.42), (4.45) have additional positive terms in the LHS, and the violation of the inequality is not strict. Even so, for $\tilde{\rho}_p$ with sufficiently high degree of polarization (close to 1), it is possible to choose $\hat{\mathcal{U}}_1$ and $\hat{\mathcal{U}}_2$ such that the modified inequalities (4.22) and (4.42), (4.45) are violated. For instance, in the modified inequalities (4.42) and (4.45), it is possible to choose sufficiently large relative shift factor $\mathbf{d}_1 - \mathbf{d}_2$ such that the modified inequalities are violated, and consequently the resulting

$\hat{\Gamma}_{\mathcal{U}_{12}}$ is polarization-spatial entangled.

4.3 Experimental realization

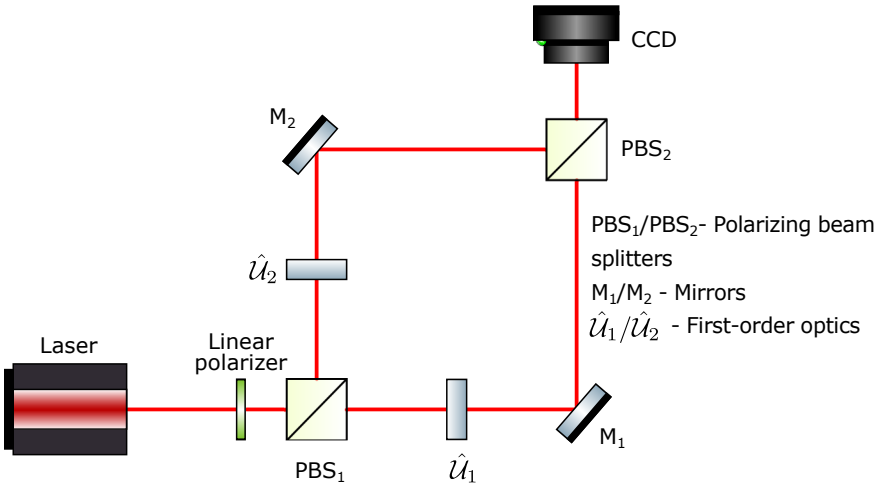

Figure 4.1: Schematic diagram of an experimental setup for realizing polarization-conditional Gaussian unitary transformation $\hat{\mathcal{U}}_{12}$ [see Eq. (4.23)].

Figure 4.1 shows an experimental setup for realizing the polarization-conditional Gaussian unitary transformation $\hat{\mathcal{U}}_{12}$. The incoming partially coherent vector Gaussian light field is passed through a linear polarizer to obtain the cross-spectral density operator as in Eq. (4.1). PBS_1 achieves the polarization-conditional separation of the light field to the two arms of the interferometer. A sequence of lenses and free propagations realize $\hat{\mathcal{U}}_1$ and $\hat{\mathcal{U}}_2$ [67, 82, 83, 134–136] in the two arms of the interferometer. The displacement parameters $\mathbf{d}_1$, $\mathbf{d}_2$ of $\hat{\mathcal{U}}_1$ and $\hat{\mathcal{U}}_2$ of (4.24) are naturally produced through misalignment in the lenses realizing $\hat{\mathcal{U}}_1$ and $\hat{\mathcal{U}}_2$ and tilts in mirrors M_1 and M_2. Further the coherence for each pure state component in the ensemble is retained across the two arms. The light fields are eventually recombined in PBS_2 to obtain the equivalent $\hat{\Gamma}_{\mathcal{U}_{12}}$ of Eq. (4.25), with $\hat{\mathcal{U}}_1$ and $\hat{\mathcal{U}}_2$ as in (4.24). As an example, a polarized GSM light field, say for instance generated using SLM [96–98] with 45° polarization and entering PBS_1 and propagating different distances in the two arms of the interferometer and with the mirrors M_1 and M_2 having relative tilt, readily produces partially coherent polarization-spatial entanglement on recombining at PBS_2. This may be understood as follows. The GSM itself is realized using a SLM by producing time varying spatially coherent light fields averaged over time (the ensemble realizing GSM). Each spatially coherent light field at a given instance of time

on passage through the setup and recombined at PBS_2 is polarization-spatial entangled for relative tilts $(\mathbf{d}_1 - \mathbf{d}_2)$ introduced in mirrors M_1 and M_2, an implication of the Theorem 3. Not only that, the time averaged (ensemble averaged) spatially coherent light fields recombined at PBS_2 is definitely polarization-spatial entangled, as seen through Theorems 2 and 3. In particular, when the GSM reduces to the fundamental Gaussian mode (limiting case), there is polarization-spatial entanglement in the recombined light field for non zero relative tilt in the two arms, which is readily confirmed through fringe movement as outlined in Chapter 3.

The following remarks are in order concerning the obtained results in Theorems 1 to 3, and in regard of the experimental setup outlined in Fig. 4.1. First, though the entanglement of the concerned states is technically detected through the partial transpose map, the violation of positivity condition is inferred through the violation of the uncertainty principle [see Eqs. (4.22), (4.42) and (4.45)], which is based on the first and second moments. We note that these moments are readily measured for a scalar light field [137–139], and thus in principle extendable to vector fields. This suggests that the polarization-spatial entanglement generated through the setup of Fig. 4.1 can indeed be experimentally demonstrated through appropriate measurement of the first and second moments. Second, the setup in Fig. 4.1 effectively simulates the class of $2 \times N$ dimensional quantum mechanical mixed 'entangled' states as stated in Eq. (4.46). This further suggests that the more general $2 \times N$ states such as those well studied in the quantum optical context [16–20, 120–126] can perhaps be simulated through classical optic means. Third, the setup gives us a flexible tool to engineer polarization-spatial entanglement through design of the unitaries $\hat{\mathcal{U}}_1$ and $\hat{\mathcal{U}}_2$, and this could be useful for instance in applications such as optical communication [127–129], polarization metrology [29], and sensing [30] where vector light fields are used. Fourth, the fact that the polarization-spatial entanglement is a function of the relative tilt for coherent inputs (as outlined in Chapter 3), could be effectively used to calibrate the relative tilt in the interferometer by measuring polarization-spatial entanglement.

4.4 Concluding remarks

To conclude, we have studied polarization-spatial entanglement in partially coherent vector light fields, or equivalently, mixed state qubit-harmonic oscillator mode entanglement. We have introduced a generalized uncertainty principle, suited for the present context, through which partial transpose is implemented. We have identified states for which partial transpose is found to be necessary and sufficient in detecting bipartite entanglement. We have

further proposed an experimental realization of such entangled states, which is very much feasible, given that the same has been achieved in the case of purely coherent vector light fields as seen in Chapter 3. While the presence of the phenomena of bound entanglement in such states is ruled out, the wide spectrum of possibilities in the polarization-spatial degrees of freedom, suggests that exotic quantum phenomena such as bound entanglement can be effectively simulated using classical optic vector light fields through the polarization-spatial degrees of freedom. For example, experimental demonstration of bound entanglement using optics has been done in Ref. [140], and such a state can be classically simulated by encoding the state into the polarization of the spatial modes of a classical optic vector light field. The work discussed in this chapter is definitely relevant given the current interest in bipartite entanglement, not only in vector paraxial wave optics [6, 7, 27, 29, 30, 33, 34, 36–38, 45–47, 127–129] but also in quantum optical systems [16–20, 120–126].

Chapter 5

Detection of polarization-spatial entanglement in partially coherent light fields using intensity measurements

5.1 Introduction

The partial transpose map has been well explored due to its applicability to both finite and infinite dimensional systems. In fact, it has been found to be necessary and sufficient in detecting bipartite entanglement for certain class of mixed states in both finite [60, 61] as well as infinite [21, 23, 63] dimensional settings. The partial transpose map can be implemented directly on the state (density matrix) [60, 61], and bipartite entanglement is then detected through violation of positivity of the resulting matrix. Alternatively, partial transpose can be implemented through observable moments evaluated on the state [63], and bipartite entanglement is then detected through violation of the uncertainty principle. In Chapter 4, partial transpose was implemented through a generalized uncertainty principle suited for the polarization-spatial context. Negativity under partial transpose was shown to be necessary and sufficient in detecting polarization-spatial entanglement for a class of partially coherent vector light fields, through the observable moments. It may be noted that the observable moments of the state of the light field are in principle estimated from the measured intensities.

In this chapter, we outline a method to implement partial transpose to detect entanglement in a partially coherent vector light field using intensities measured at various orientations of the polarizer on the incoming light field. We obtain a sufficient criteria for detecting polarization-spatial entanglement using the measured intensities. The present

method makes no restriction on the intensity measurements, for instance, as being confined to dichotomic observables on the spatial degree of freedom, in implementation of the CHSH [141] Bell-type inequality in the polarization-spatial context [33, 57]. That is, the method is applicable to partially coherent vector light fields, with no restriction on the spatial modes to be confined to a two dimensional subspace. Further, entanglement detection methods using uncertainty principle, as for instance outlined in Ref. [63] and in Chapter 4, requires the estimation of moments of field intensities, as well as moments of intensities of the field amplitude in the Fourier domain. The present method has no such requirements.

The chapter is organized as follows. In Section 5.2, we outline the implication of partial transpose on intensities measured at various orientations of the polarizer. The detection of polarization-spatial entanglement, through partial transpose map implemented using measured intensities, is discussed in Section 5.3. An experimental demonstration of the proposed method is also outlined here. The experimental results are discussed in Section 5.4. We finally end with some concluding remarks in Section 5.5.

5.2 Theoretical analysis

The cross-spectral density matrix or beam coherency matrix of a spatially partially coherent vector light field is given by [45, 100, 142]

$$\begin{aligned}\langle x_1, y_1|\hat{\mathbf{\Gamma}}|x_2, y_2\rangle &= \mathbf{\Gamma}(x_1, y_1; x_2, y_2) = \langle \Psi(x_1, y_1)\Psi(x_2, y_2)^\dagger\rangle \\ &= \begin{bmatrix} \Big\langle |c_0|^2\psi_1(x_1, y_1)\psi_1^*(x_2, y_2)\Big\rangle & \Big\langle c_0c_1^*\psi_1(x_1, y_1)\psi_2^*(x_2, y_2)\Big\rangle \\ \Big\langle c_1c_0^*\psi_2(x_1, y_1)\psi_1^*(x_2, y_2)\Big\rangle & \Big\langle |c_1|^2\psi_2(x_1, y_1)\psi_2^*(x_2, y_2)\Big\rangle \end{bmatrix}. \end{aligned} \tag{5.1}$$

Here $\langle\cdots\rangle$ denotes ensemble average, for instance,

$$\Big\langle |c_0|^2\psi_1(x_1, y_1)\psi_1^*(x_2, y_2)\Big\rangle \equiv \sum_i p_i|c_{0i}|^2\psi_{1i}(x_1, y_1)\psi_{1i}^*(x_2, y_2). \tag{5.2}$$

Here, the frequency dependence has been suppressed since we are working with a quasi-monochromatic source.

We may recall that on passage of light as described by the cross-spectral density matrix in Eq. (5.1) through a polarizer oriented at θ, the resulting intensity at the coordinate (x, y)

is

$$I_\theta(x,y) = C_\theta^2\Big\langle |c_0|^2|\psi_1(x,y)|^2\Big\rangle + C_\theta S_\theta\Big\langle c_0c_1^*\psi_1(x,y)\psi_2^*(x,y)\Big\rangle + S_\theta C_\theta\Big\langle c_1c_0^*\psi_2(x,y)\psi_1^*(x,y)\Big\rangle + S_\theta^2\Big\langle |c_1|^2|\psi_2(x,y)|^2\Big\rangle \geq 0. \tag{5.3}$$

Further, the intensity at the coordinate (x,y) is given by the trace of the cross-spectral density matrix $\mathbf{\Gamma}(x,y;x,y)$, that is, $I(x,y) = \Big\langle |c_0|^2|\psi_1(x,y)|^2\Big\rangle + \Big\langle |c_1|^2|\psi_2(x,y)|^2\Big\rangle$.

By definition $\hat{\mathbf{\Gamma}}$ is positive semi-definite. On taking the expectation value of $\hat{\mathbf{\Gamma}}$ with the vector $C_\theta|0\rangle|x-\alpha,y-\beta\rangle + S_\theta|1\rangle|x,y\rangle$, we obtain

$$I_\theta^{\alpha\beta}(x,y) = C_\theta^2\Big\langle |c_0|^2|\psi_1(x-\alpha,y-\beta)|^2\Big\rangle + C_\theta S_\theta\Big\langle c_0c_1^*\psi_1(x-\alpha,y-\beta)\psi_2^*(x,y)\Big\rangle + S_\theta C_\theta\Big\langle c_1c_0^*\psi_2(x,y)\psi_1^*(x-\alpha,y-\beta)\Big\rangle + S_\theta^2\Big\langle |c_1|^2|\psi_2(x,y)|^2\Big\rangle \geq 0, \tag{5.4}$$

where α and β are real numbers. Note that the intensity $I_\theta^{\alpha\beta}(x,y)$ of (5.4) is same as the intensity $I_\theta(x,y)$ of (5.3), however with the x-component of the cross-spectral density imparted a spatial shift of (α,β) in the x and y coordinates, in a polarization conditional manner, before being passed through the polarizer.

By Peres-Horodecki separability criterion [60,61], the partial transpose operation takes a separable cross-spectral density operator $\hat{\mathbf{\Gamma}}$ necessarily into a non-negative operator, i.e.,

$$\hat{\mathbf{\Gamma}}^{\text{PT}} = \sum_i p_i\left[|\Psi_i\rangle\langle\Psi_i|\right]^{\text{PT}} \geq 0, \tag{5.5}$$

where the superscript PT denotes partial transpose. Performing the transpose on the spatial states $|\psi_{1i}\rangle$ and $|\psi_{2i}\rangle$, i.e., $|\psi_{1i}\rangle\langle\psi_{2i}| \to |\psi_{2i}^*\rangle\langle\psi_{1i}^*|$ to obtain $\hat{\mathbf{\Gamma}}^{\text{PT}}$, the expectation value of $\hat{\mathbf{\Gamma}}^{\text{PT}}$ with the vector $C_\theta|0\rangle|x,y\rangle + S_\theta|1\rangle|x-\alpha,y-\beta\rangle$ is

$$\tilde{I}_\theta^{\alpha\beta}(x,y) = C_\theta^2\Big\langle |c_0|^2|\psi_1(x,y)|^2\Big\rangle + C_\theta S_\theta\Big\langle c_0c_1^*\psi_1(x-\alpha,y-\beta)\psi_2^*(x,y)\Big\rangle + S_\theta C_\theta\Big\langle c_1c_0^*\psi_2(x,y)\psi_1^*(x-\alpha,y-\beta)\Big\rangle + S_\theta^2\Big\langle |c_1|^2|\psi_2(x-\alpha,y-\beta)|^2\Big\rangle \geq 0. \tag{5.6}$$

Consider the instance when $\hat{\Gamma} = |\Psi\rangle\langle\Psi|$, with $|\Psi\rangle = (c_0|0\rangle + c_1|1\rangle)\otimes|\psi\rangle$, i.e, a product state, the inequality (5.6) then reduces to

$$|C_\theta c_0\psi(x,y) + S_\theta c_1\psi(x-\alpha,y-\beta)|^2 \geq 0, \tag{5.7}$$

which by definition is always true. Any violation of inequality (5.6) indicates the presence

of polarization-spatial entanglement. Thus, if we are able to experimentally determine all terms in the LHS of (5.6), then it is possible to detect the presence of polarization-spatial entanglement in a light field represented by the cross-spectral density matrix $\mathbf{\Gamma}$ in Eq. (5.1). A method to experimentally determine the LHS of (5.6) is discussed below.

Assume that a light field denoted by the cross-spectral density matrix $\mathbf{\Gamma}(x_1, y_1; x_2, y_2)$, as in Eq. (5.1), is available to us. In order to detect the presence of polarization-spatial entanglement in the given light field, we impart a spatial shift of (α, β) in the x and y coordinates onto the x-component of the light field. It is then passed through a polarizer to obtain the output intensity $I_\theta^{\alpha\beta}(x, y)$ as in (5.4). In order to evaluate the terms in the LHS of (5.6), we measure $I_\theta^{\alpha\beta}(x, y)$ of (5.4) at $\theta = 0°, 45°, 90°$, and $135°$, and we have

$$I_0^{\alpha\beta}(x, y) = \Big\langle |c_0|^2 |\psi_1(x-\alpha, y-\beta)|^2 \Big\rangle, \tag{5.8}$$

$$\begin{aligned} I_{45}^{\alpha\beta}(x, y) - I_{135}^{\alpha\beta}(x, y) =& \Big\langle c_0 c_1^* \psi_1(x-\alpha, y-\beta) \psi_2^*(x, y) \Big\rangle \\ &+ \Big\langle c_1 c_0^* \psi_2(x, y) \psi_1^*(x-\alpha, y-\beta) \Big\rangle, \text{ and} \end{aligned} \tag{5.9}$$

$$I_{90}^{\alpha\beta}(x, y) = \Big\langle |c_1|^2 |\psi_2(x, y)|^2 \Big\rangle. \tag{5.10}$$

Note that the point-wise Stokes parameters (generalized Stokes parameters) can be written in terms of the measured intensities of Eqs. (5.8)-(5.10) as, $\mathrm{S}_0(x, y) = I_0^{\alpha\beta}(x, y) + I_{90}^{\alpha\beta}(x, y)$, $\mathrm{S}_1(x, y) = I_0^{\alpha\beta}(x, y) - I_{90}^{\alpha\beta}(x, y)$, and $\mathrm{S}_2(x, y) = I_{45}^{\alpha\beta}(x, y) - I_{135}^{\alpha\beta}(x, y)$ [112]. Clearly from Eq. (5.9), we can infer that the second and third terms in the LHS of (5.6) are readily obtained from the intensities measured at $\theta = 45°$ and $135°$. The first term in the LHS of (5.6) can be determined by numerically shifting the intensity $I_0^{\alpha\beta}(x, y)$ [see Eq. (5.8)], through the knowledge of α and β, i.e., $I_0^{\alpha\beta}(x+\alpha, y+\beta) \equiv \Big\langle |c_0|^2 |\psi_1(x, y)|^2 \Big\rangle$. Likewise, the last term in the LHS of (5.6) can be determined by numerically shifting the intensity $I_{90}^{\alpha\beta}(x, y)$ [see Eq. (5.10)]. As we shall see, it is possible to estimate the required shifts α and β experimentally. Inequality (5.6) at $\theta = 45°$ can be rewritten as

$$\tilde{\mathcal{I}}_{45}^{\alpha\beta}(x, y) = \frac{1}{2}\Big[I_0^{\alpha\beta}(x+\alpha, y+\beta) + I_{45}^{\alpha\beta}(x, y) - I_{135}^{\alpha\beta}(x, y) + I_{90}^{\alpha\beta}(x-\alpha, y-\beta) \Big] \geq 0. \tag{5.11}$$

Here, $\tilde{\mathcal{I}}_{45}^{\alpha\beta}(x, y)$ denotes the intensity $\tilde{I}_{45}^{\alpha\beta}(x, y)$ in (5.6) obtained through sequential addition of measured and numerically shifted intensities. Though ideally we have $\tilde{\mathcal{I}}_{45}^{\alpha\beta}(x, y) = \tilde{I}_{45}^{\alpha\beta}(x, y)$, experimentally this may not be true owing to various factors such as intensity fluctuations that act as noise. As a further note, the LHS of (5.4) can be directly obtained from measured intensity $\Big[I_{45}^{\alpha\beta}(x, y) \Big]$ and by definition is point-wise positive, even so, it can

also be obtained as the sum of the LHS of Eqs. (5.8)-(5.10), i.e.,

$$\mathcal{I}_{45}^{\alpha\beta}(x,y) = \frac{1}{2}\left[I_{0}^{\alpha\beta}(x,y) + I_{45}^{\alpha\beta}(x,y) - I_{135}^{\alpha\beta}(x,y) + I_{90}^{\alpha\beta}(x,y)\right]. \tag{5.12}$$

Here, $\mathcal{I}_{45}^{\alpha\beta}(x,y)$ denotes the intensity $I_{45}^{\alpha\beta}(x,y)$ in (5.4) obtained through sequential addition of measured intensities. Ideally, $\mathcal{I}_{45}^{\alpha\beta}(x,y) = I_{45}^{\alpha\beta}(x,y)$. Nevertheless, experimental evaluation in this manner can render negative values owing to noise caused by the fluctuations of the light field during sequential intensity measurements.

5.3 Detection of polarization-spatial entanglement using intensity measurements

We now discuss an experiment which will demonstrate the inequality (5.11). Here, for our experiment, a coherent Gaussian light field coming from a 632.8 nm He-Ne laser source is passed through a linear polarizer (LP_1), and then through a PBS. The PBS splits the light field into its horizontal and vertical components. The horizontal and vertical components, traverse the two arms of the Mach-Zehnder interferometer through mirrors M_1 and M_2 and recombine at the beam splitter BS as in Fig. 5.1. Owing to the different paths traversed by the light fields, there exist a relative longitudinal displacement between the polarization components. In addition to that, the difference in orientation of mirrors M_1 and M_2 result in a relative tilt between the two polarization components. We may recall that in Chapters 3 and 4, such recombined light fields were shown to acquire polarization-spatial entanglement, even for a small relative tilt between the two mirrors. We now outline the possible detection of polarization-spatial entanglement in such light fields through violation of the inequality (5.11). Figure 5.1 outlines the experimental setup.

The initial polarizer LP_1 is oriented at an angle ϕ, and the light coming out of LP_1 is passed through a Mach-Zehnder interferometer as in Fig. 5.1. The mirrors M_1 and M_2 have a relative tilt, so that the recombined field at the output of the Mach-Zehnder interferometer is polarization-spatial entangled. Assume that the output light field is denoted by

$$\Psi(x,y) = \begin{bmatrix} c_0\psi_1(x,y) \\ c_1\psi_2(x,y) \end{bmatrix}, \tag{5.13}$$

as given in Eq. (2.100). The goal here is to detect polarization-spatial entanglement in $\Psi(x,y)$ through the measured intensities as in (5.11).

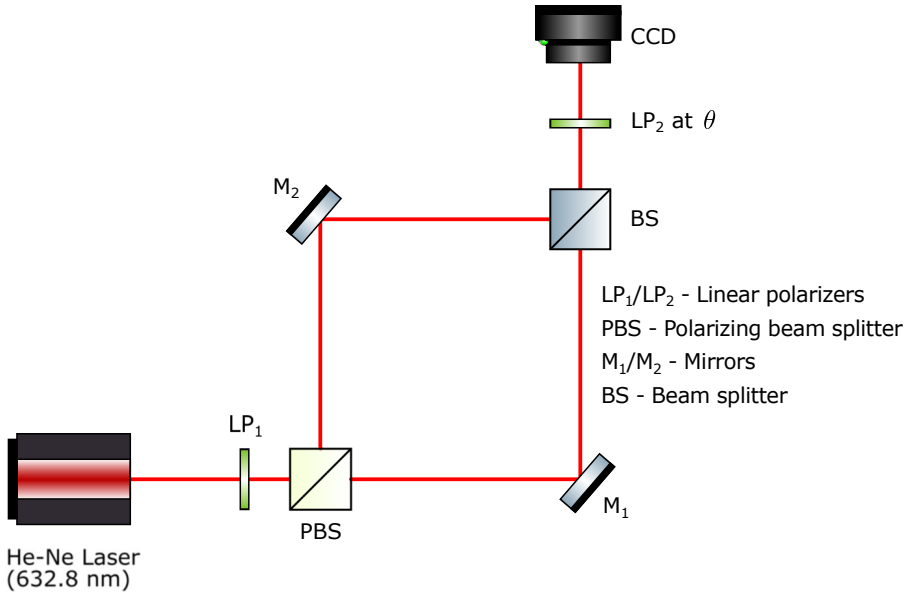

Figure 5.1: Schematic diagram of the experimental setup.

Let us assume that the horizontal component of the recombined light field $\psi_1(x, y)$ is centered with respect to the camera frame of reference, whereas the vertical component $\psi_2(x, y)$ is slightly off-centered due to the relative tilt in the mirrors. In order to achieve this in lab we visually center the intensity at $\theta = 0^\circ$ on the camera, and slightly off-center the intensity at $\theta = 90^\circ$, by adjusting the mirrors M_1 and M_2. The camera position is now fixed. The x and y moments of the intensity at $\theta = 0^\circ$ is evaluated, and then the camera coordinate system is recentered through the evaluated x and y moments. The x and y moments numerically evaluated on a measured intensity $I(x, y)$ is given by

$$\langle \hat{x} \rangle = \frac{\sum_{i=1}^{N} \sum_{j=1}^{N} x(i,j) I(i,j)}{\sum_{i=1}^{N} \sum_{j=1}^{N} I(i,j)}, \text{ and } \langle \hat{y} \rangle = \frac{\sum_{i=1}^{N} \sum_{j=1}^{N} y(i,j) I(i,j)}{\sum_{i=1}^{N} \sum_{j=1}^{N} I(i,j)}, \tag{5.14}$$

respectively, where $x(i, j) = i\delta_x$ and $y(i, j) = j\delta_y$. Here we have $\delta_x = \delta_y = 6.45\mu$m, the pixel size of the camera. The camera had 1392×1040 pixels, even so, we set $N = 1024$ by cropping the image in a centered manner. Note that the recentering of the camera coordinate system does not affect the relative tilt between the horizontal component $\psi_1(x, y)$ and the vertical component $\psi_2(x, y)$. Also, for polarizer LP_2 oriented at θ, the intensity at the CCD is of the form $I_\theta(x, y)$ defined in Eq. (5.3). From (5.6) we can infer that, in order to detect the presence of polarization-spatial entanglement between a centered $\psi_1(x, y)$ and a slightly off-centered $\psi_2(x, y)$, we need to displace $\psi_1(x, y)$ by a deterministic amount. An

angular tilt on mirror M_1 can be considered equivalently as a lateral shift of the horizontal component $\psi_1(x,y)$ of the light field. Hence, we tilt mirror M_1 to displace $\psi_1(x,y)$ and thus obtain $\psi_1(x-\alpha, y-\beta)$. Note that, the mirror M_2 is not disturbed and hence the vertical component $\psi_2(x,y)$ is not displaced. Thus for polarizer LP_2 oriented at θ, the intensity at the CCD after tilting mirror M_1, is of the form $I_\theta^{\alpha\beta}(x,y)$ defined in (5.4). In order to experimentally determine the displacement given to the horizontal component of the light field $\psi_1(x,y)$, we measure the intensity $I_0^{\alpha\beta}(x,y)$ for polarizer LP_2 oriented at $\theta = 0^\circ$. The moments $\langle\hat{x}\rangle$ and $\langle\hat{y}\rangle$ rounded off to the nearest pixel value, evaluated on the intensity $I_0^{\alpha\beta}(x,y)$ give the values of α and β respectively. Now that the values of α and β are known, in order to evaluate $\tilde{\mathcal{I}}_{45}^{\alpha\beta}(x,y)$ of (5.11), we measure the intensities at $\theta = 0^\circ, 45^\circ, 90^\circ$, and 135°, i.e., $I_0^{\alpha\beta}(x,y), I_{45}^{\alpha\beta}(x,y), I_{90}^{\alpha\beta}(x,y)$, and $I_{135}^{\alpha\beta}(x,y)$, respectively. The first and last terms out of the four terms that constitute $\tilde{\mathcal{I}}_{45}^{\alpha\beta}(x,y)$ of (5.11), is determined by numerically shifting the intensities $I_0^{\alpha\beta}(x,y)$ and $I_{90}^{\alpha\beta}(x,y)$ to obtain $I_0^{\alpha\beta}(x+\alpha, y+\beta)$ and $I_{90}^{\alpha\beta}(x-\alpha, y-\beta)$, through the knowledge of α and β. Thus, on obtaining the intensities $I_{45}^{\alpha\beta}(x,y)$ and $I_{135}^{\alpha\beta}(x,y)$, along with the numerically shifted intensities $I_0^{\alpha\beta}(x+\alpha, y+\beta)$ and $I_{90}^{\alpha\beta}(x-\alpha, y-\beta)$, we are able to determine $\tilde{\mathcal{I}}_{45}^{\alpha\beta}(x,y)$ of (5.11). We note that the same procedure can be followed for any partially coherent light source available at the input of Fig. 5.1. In what follows, we consider 'effective' partial coherent source as the input, which is generated through sequential coherent inputs.

In order to experimentally replicate a partially coherent vector light field, we vary the orientation of the initial polarizer LP_1 sequentially, and consider them to be probabilistic to obtain the ensemble. We also vary the tilt of mirror M_2 in a LP_1 controlled manner. The probabilities themselves are varied numerically on a computer. Consider the mixture

$$\hat{\mathbf{\Gamma}} = \sum_i^n p_i |\Psi_i\rangle\langle\Psi_i|, \tag{5.15}$$

as in Eq. (2.101). Assume $|\psi_{1i}\rangle$ are identical with $|\psi_{2i}\rangle$ non-identical. Also, c_{ji} are varying. Then a mixture as in Eq. (5.15) can be thought of as $|\Psi_i\rangle$ generated sequentially by varying the orientation of polarizer LP_1, simultaneously varying the orientation of mirror M_2 for every orientation of polarizer LP_1, while keeping the orientation of mirror M_1 fixed, with the probabilities p_i varied numerically. In what follows, we demonstrate how polarization-spatial entanglement in such a mixture can be detected through sequential intensity measurements.

As seen from (5.6), the displacements α and β are identical for all the constituting polarization components in the mixture. Thus to simulate the detection of entanglement in

a mixture as in Eq. (5.15), once mirror M_1 is tilted (horizontal component) and α and β are determined for an initial polarization state, we do not disturb it further. Note that, the vertical component need not be same for every orientation of the input polarizer LP_1, and hence the mirror M_2 can have differential tilt depending on the input polarizer orientation. Consider generating a state that is a mixture of n input polarization states, say LP_1 oriented at ϕ_1, ϕ_2,...,ϕ_n, with probabilities p_1, p_2,...,p_n, respectively. For an input polarization state with LP_1 oriented at ϕ_i, the recombined light field at the output of the beam splitter is of the form given by Eq. (5.13) and can be denoted as $\Psi_i(x, y)$, where the subscript i denotes the i^{th} instance of orientation of polarizer LP_1. For $i = 1$, the input polarizer LP_1 is oriented at ϕ_1 and we have the recombined light field denoted as $\Psi_1(x, y)$. The mirror M_1 is given a tilt to impart a spatial shift of (α, β) onto the horizontal component $\psi_{11}(x, y)$ of the light field in order to obtain $\psi_{11}(x - \alpha, y - \beta)$. The values of α and β are evaluated through the moments as outlined earlier. Once α and β are evaluated for the initial input polarization state, position of mirror M_1 is fixed. In order to evaluate $\tilde{\mathcal{I}}_{45}^{\alpha\beta}(x, y)$ of (5.11), the intensities are measured at $\theta = 0^\circ, 45^\circ, 90^\circ$, and 135°, i.e., $I_0^1(x, y), I_{45}^1(x, y), I_{90}^1(x, y)$, and $I_{135}^1(x, y)$, respectively. For the input polarization state where polarizer LP_1 is oriented at ϕ_2, mirror M_1 is not disturbed, and mirror M_2 is given an additional tilt to obtain the state $\Psi_2(x, y)$ at the output of the beam splitter. The intensities at $\theta = 0^\circ, 45^\circ, 90^\circ$, and 135°, i.e., $I_0^2(x, y), I_{45}^2(x, y), I_{90}^2(x, y)$, and $I_{135}^2(x, y)$, respectively, are measured. Similarly, the intensities $I_0^i(x, y), I_{45}^i(x, y), I_{90}^i(x, y)$, and $I_{135}^i(x, y)$, corresponding to the state $\Psi_i(x, y)$ for the next i, are measured without disturbing mirror M_1. Now to obtain the intensity corresponding to the mixture for a particular θ of polarizer LP_2, the intensities are multiplied by their corresponding probabilities and then added, i.e.,

$$I_\theta^{\alpha\beta}(x, y) = \sum_{i=1}^{n} p_i I_\theta^i(x, y), \tag{5.16}$$

and thereby determine the intensities given in Eqs. (5.8)-(5.10), for the partially coherent case. Using this newly obtained set of intensities, $\tilde{\mathcal{I}}_{45}^{\alpha\beta}(x, y)$ of (5.11) is determined by following the same procedure as in the case of coherent vector light fields. The intensities $I_0^{\alpha\beta}(x, y)$ and $I_{90}^{\alpha\beta}(x, y)$ are numerically shifted through the knowledge of α and β, to obtain $I_0^{\alpha\beta}(x+\alpha, y+\beta)$ and $I_{90}^{\alpha\beta}(x-\alpha, y-\beta)$. The intensities $I_{45}^{\alpha\beta}(x, y)$ and $I_{135}^{\alpha\beta}(x, y)$ are directly available to us, and thus $\tilde{\mathcal{I}}_{45}^{\alpha\beta}(x, y)$ of inequality (5.11) can be evaluated for the partially coherent light field as in Eq. (5.15).

5.4 Experimental results

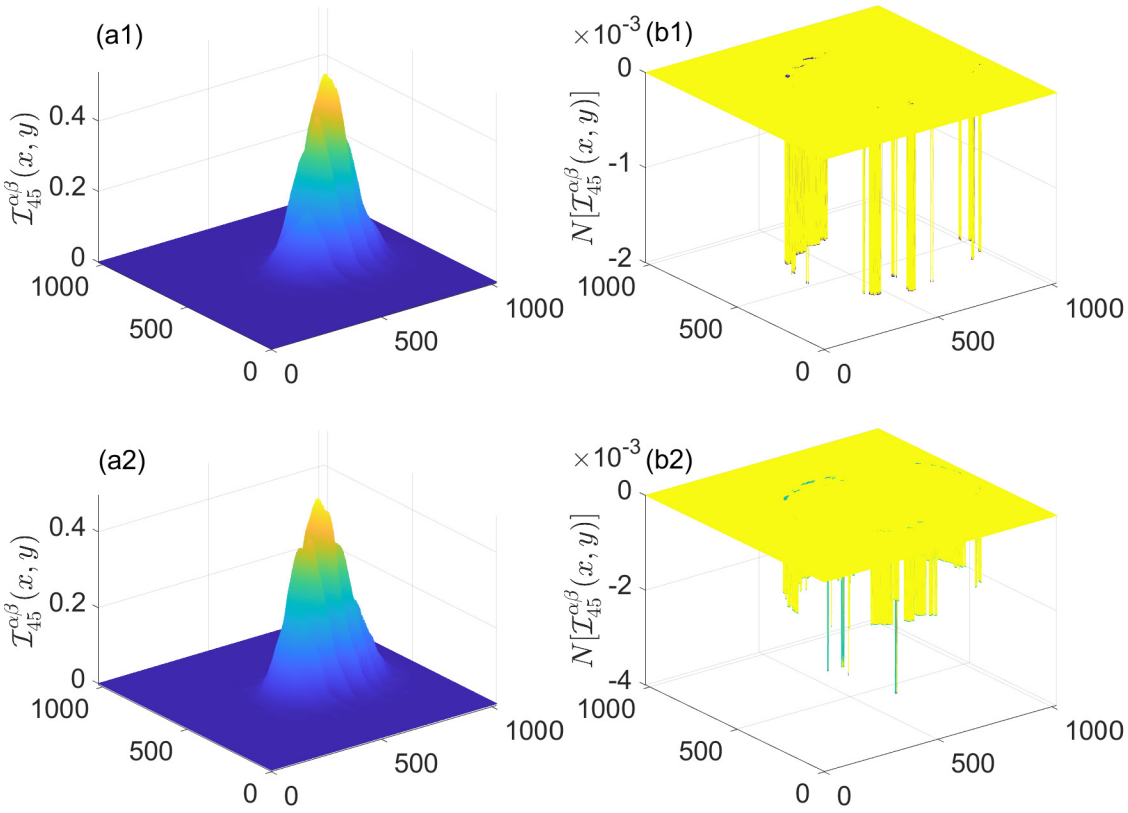

Figure 5.2: (a1) plots $\mathcal{I}_{45}^{\alpha\beta}(x,y)$ of Eq. (5.12), for a coherent vector light field with initial polarizer LP_1 oriented at 43° with a particular relative tilt between mirrors M_1 and M_2. (b1) plots $N[\mathcal{I}_{45}^{\alpha\beta}(x,y)]$, the negative values of $\mathcal{I}_{45}^{\alpha\beta}(x,y)$ plotted in (a1). (a2) and (b2) repeats the exercise as in (a1) and (b1), but for another example with different relative tilt between mirrors M_1 and M_2 and for polarizer LP_1 oriented at 47°. Note that, though ideally $\mathcal{I}_{45}^{\alpha\beta}(x,y)$ is supposed to be positive there exists some negative values of the order of 0.001 due to noise, which emerges as a consequence of sequential intensity measurements.

The measurement of the intensities were carried out in the following manner. At every instance, 100 images were taken manually, roughly at an interval of one second, and averaged. This ensured that the intensity fluctuations are taken care of, and the measured intensities are sufficiently stationary. We benchmark the stationarity of the measured intensities as follows. The intensity $I_{45}^{\alpha\beta}(x,y)$ as in (5.4), is readily available as a measurable intensity, which by definition is point-wise positive. However, it is also obtained by sequentially adding the intensities in Eqs. (5.8)-(5.10) [$\mathcal{I}_{45}^{\alpha\beta}(x,y)$ of Eq. (5.12)], which should also yield

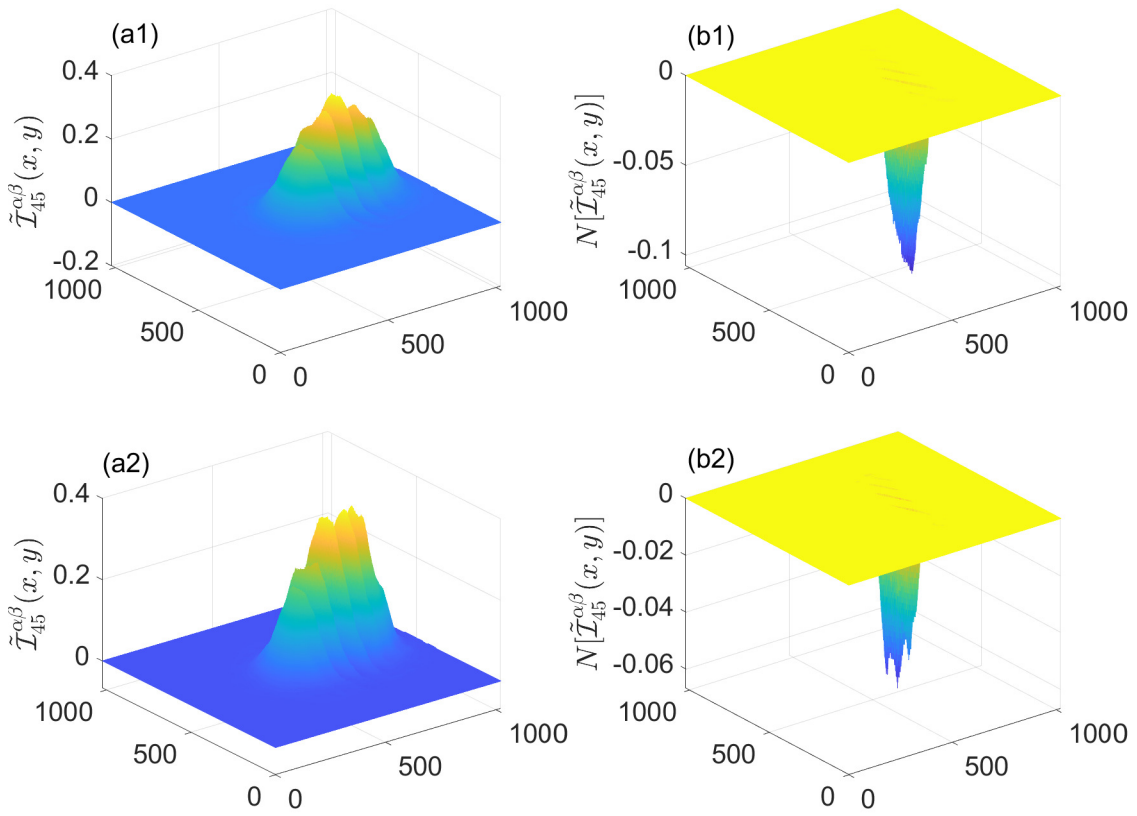

Figure 5.3: (a1) plots $\tilde{\mathcal{I}}_{45}^{\alpha\beta}(x,y)$ of (5.11) for the coherent vector light field considered in Fig. 5.2 (a1). (b1) plots $N[\tilde{\mathcal{I}}_{45}^{\alpha\beta}(x,y)]$, the negative values of $\tilde{\mathcal{I}}_{45}^{\alpha\beta}(x,y)$ plotted in (a1). (a2) and (b2) repeats the exercise as in (a1) and (b1), but for the example considered in Fig. 5.2 (a2). Note that in both the examples, the minimum of $\tilde{\mathcal{I}}_{45}^{\alpha\beta}(x,y)$ is an order lower than the minimum of $\mathcal{I}_{45}^{\alpha\beta}(x,y)$, suggesting that the considered input light fields are polarization-spatial entangled.

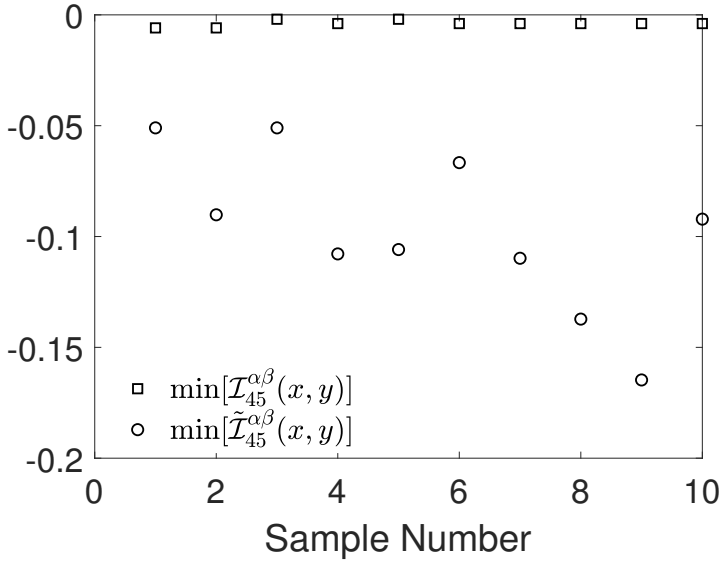

Figure 5.4: Ten different examples of coherent vector light fields are considered here, with P_1 oriented at 43° for four of them, and at 47° for the remaining six. The relative tilt between mirrors M_1 and M_2 is different for all ten. $\square$ plots the min$[\mathcal{I}_{45}^{\alpha\beta}(x,y)]$ and $\circ$ plots the min$[\tilde{\mathcal{I}}_{45}^{\alpha\beta}(x,y)]$ for varying samples.

point-wise positive values. $\mathcal{I}_{45}^{\alpha\beta}(x,y)$ of Eq. (5.12) having negative values is an indicator of the fluctuation of the light intensities. This is of relevance since a test for polarization-spatial entanglement as in (5.11) is also obtained as a sequential addition of intensities, i.e., $\tilde{\mathcal{I}}_{45}^{\alpha\beta}(x,y)$, albeit with numerical shift on the intensities. Figure 5.2 (a1) plots $\mathcal{I}_{45}^{\alpha\beta}(x,y)$ of Eq. (5.12), for an example with LP_1 oriented at 43°, with a particular relative tilt between mirrors M_1 and M_2. $N[\mathcal{I}_{45}^{\alpha\beta}(x,y)]$ which plots only the negative values of $\mathcal{I}_{45}^{\alpha\beta}(x,y)$, is plotted in Fig. 5.2 (b1). This is repeated in Figs. 5.2 (a2) and 5.2 (b2) for LP_1 oriented at 47°, with slightly different relative tilt between M_1 and M_2. We can clearly see that the resulting intensities plotted in Figs. 5.2 (a1) and 5.2(a2), does possess small negative values of the order of 0.001, for peak intensity values of 0.5372 and 0.4961, respectively. This can be attributed to noise due to the fluctuation of the light field and also to the non-uniform spatial modulation of intensities as introduced by the polarizers. This suggests that in order to detect entanglement through evaluation of $\tilde{\mathcal{I}}_{45}^{\alpha\beta}(x,y)$ of (5.11), we need to obtain negative values significantly larger than those caused by intensity fluctuations.

Now to test for entanglement through measured intensities, as a first example, we consider the case of coherent vector light fields. Figure 5.3 (a1) plot the resulting intensity obtained on evaluation of $\tilde{\mathcal{I}}_{45}^{\alpha\beta}(x,y)$ of (5.11), for the coherent vector light field consid-

ered in Fig. 5.2 (a1). $N[\tilde{\mathcal{I}}_{45}^{\alpha\beta}(x,y)]$ which plots only the negative values of $\tilde{\mathcal{I}}_{45}^{\alpha\beta}(x,y)$, is plotted in Fig. 5.3 (b1). This is repeated in Figs. 5.3 (a2) and 5.3 (b2) for the example considered in Fig. 5.2 (a2). The pixel values of (α,β) obtained for the two examples considered in Fig. 5.3 (a1) and (a2) are (-1,203) and (1,218), respectively. As evident from the plots, there are significant negative values of the order of 0.1, indicating the presence of polarization-spatial entanglement. To check further, we consider ten different examples of coherent vector light fields, four of which have LP_1 oriented at 43° and the remaining six have LP_1 oriented at 47°. The relative tilt between the mirrors M_1 and M_2 is different in all the considered examples. In Fig. 5.4, $\square$ plots the minimum value of $\mathcal{I}_{45}^{\alpha\beta}(x,y)$ denoted as $\min[\mathcal{I}_{45}^{\alpha\beta}(x,y)]$, whereas $\circ$ plots the corresponding minimum value of $\tilde{\mathcal{I}}_{45}^{\alpha\beta}(x,y)$ denoted as $\min[\tilde{\mathcal{I}}_{45}^{\alpha\beta}(x,y)]$), for all ten examples. As evident from the plot, the $\min[\tilde{\mathcal{I}}_{45}^{\alpha\beta}(x,y)]$ is lower than the $\min[\mathcal{I}_{45}^{\alpha\beta}(x,y)]$, indicating the presence of polarization-spatial entanglement in all the considered examples.

As a second example we consider the case of partially coherent vector light fields obtained by numerically mixing two pure state constituents. Figure 5.5 (a1) plots the resulting intensity obtained on evaluation of $\tilde{\mathcal{I}}_{45}^{\alpha\beta}(x,y)$ of (5.11), for such an example of partially coherent light field, for the choice of probabilities $p_1 = p_2 = 0.5$ [see Eq. (5.15)]. Here, $|\Psi_1\rangle$ is obtained by orienting the polarizer LP_1 at $\phi_1 = 43^\circ$ for a particular relative tilt between mirrors M_1 and M_2, and $|\Psi_2\rangle$ is obtained by orienting polarizer LP_1 at $\phi_2 = 47^\circ$ with mirror M_2 given an additional tilt. The negative values of $\tilde{\mathcal{I}}_{45}^{\alpha\beta}(x,y)$ plotted in Fig. 5.5 (a1), i.e., $N[\tilde{\mathcal{I}}_{45}^{\alpha\beta}(x,y)]$ is plotted in Fig. 5.5 (b1). This is repeated in Figs. 5.5 (a2) and 5.5 (b2) for another example of partially coherent light field with $p_1 = p_2 = 0.5$. Here, the polarizer LP_1 is initially oriented at $\phi_1 = 47^\circ$ with a different relative tilt between mirrors M_1 and M_2, and then the polarizer LP_1 is oriented at $\phi_2 = 43^\circ$ and mirror M_2 is given an additional tilt. Figures 5.6 (a) and 5.6 (b) plots the highest negative value obtained on evaluating $\tilde{\mathcal{I}}_{45}^{\alpha\beta}(x,y)$ of (5.11) against the probability of occurrence p_1 (varied from 0 to 1 in intervals of 0.1), for the same examples of mixed states considered in Figs. 5.5 (a1) and 5.5 (a2), respectively. Note that, in Fig. 5.6 (a) p_1 denotes the probability of occurrence of the input polarization state with LP_1 oriented at 43°, whereas in Fig. 5.6 (b) p_1 denotes the probability of occurrence of the input polarization state with LP_1 oriented at 47°. As evident from the plots in Fig. 5.6, the strength of the negative values depend on the probabilities as well as the relative tilt. Also, as seen from Fig. 5.6 (b), for the choice of $p_1 = 0.6$ and 0.7 the highest negative value obtained is of the order of 0.02, which is still significantly higher than 0.001 obtained due to intensity fluctuations, thus indicating the presence of polarization-spatial entanglement in such mixtures.

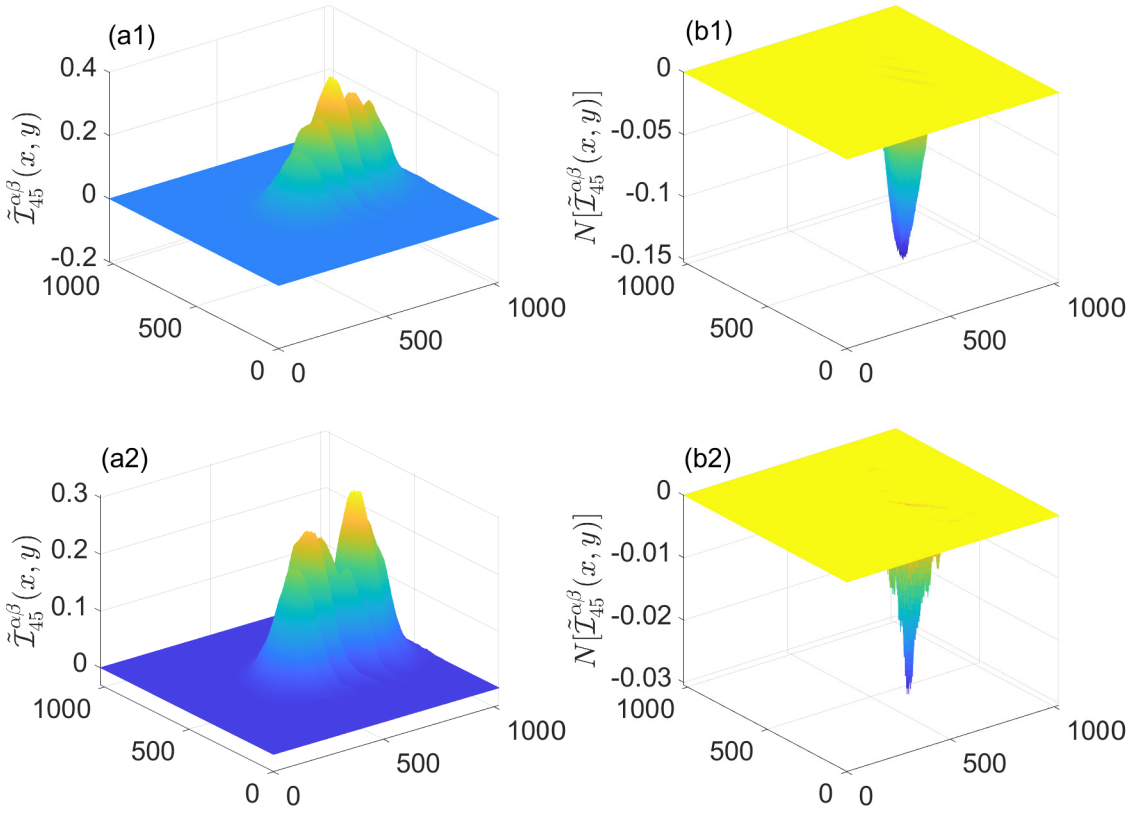

Figure 5.5: (a1) plots $\tilde{\mathcal{I}}_{45}^{\alpha\beta}(x,y)$ of (5.11) for a partially coherent light field, which is a mixture of two input polarization states with LP_1 oriented at $\phi_1 = 43^\circ$ with probability $p_1 = 0.5$, and at $\phi_2 = 47^\circ$ with probability $p_2 = 0.5$. (a2) repeats the exercise for a similar example of partially coherent light field, with LP_1 oriented at $\phi_1 = 47^\circ$ with probability $p_1 = 0.5$, and at $\phi_2 = 43^\circ$ with probability $p_2 = 0.5$. (b1) and (b2) plots $N[\tilde{\mathcal{I}}_{45}^{\alpha\beta}(x,y)]$, the negative values of $\tilde{\mathcal{I}}_{45}^{\alpha\beta}(x,y)$ plotted in (a1) and (a2), respectively.

As a third example we consider the case of partially coherent vector light fields obtained by numerically mixing three pure state constituents. Figure 5.7 plots the highest negative value obtained on evaluating $\tilde{\mathcal{I}}_{45}^{\alpha\beta}(x,y)$ of (5.11) against probabilities p_1 and p_2, for a mixture of three input polarization states with LP_1 oriented at $\phi_1 = 43^\circ$ with probability p_1, at $\phi_2 = 45^\circ$ with probability p_2, and at $\phi_3 = 47^\circ$ with probability p_3. $|\Psi_1\rangle$ is obtained by orienting LP_1 at 43° with a particular relative tilt between mirrors M_1 and M_2, $|\Psi_2\rangle$ is obtained by orienting LP_1 at 45° with mirror M_2 given an additional tilt, and $|\Psi_3\rangle$ is obtained by orienting LP_1 at 47° with mirror M_2 again given an additional tilt. As evident from the plot, we obtain significant negative values for the studied mixtures, suggesting polarization-spatial entanglement in such mixtures.

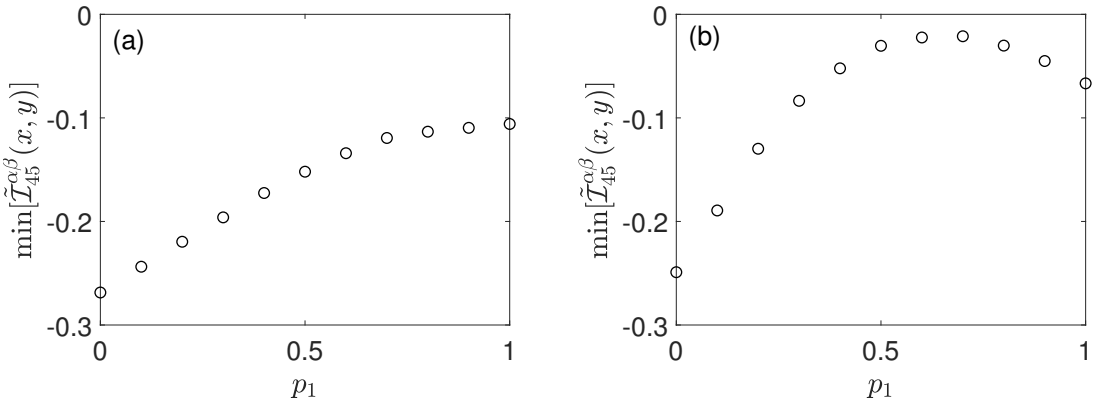

Figure 5.6: $\circ$ plots the highest negative value obtained on evaluating $\tilde{\mathcal{I}}_{45}^{\alpha\beta}(x,y)$ of (5.11) for two different examples of partially coherent light fields, against the probability of occurrence p_1 varied from 0 to 1 at intervals of 0.1. (a) corresponds to a mixture of two input polarization states with LP_1 oriented at $\phi_1 = 43^\circ$ with probability p_1, and at $\phi_2 = 47^\circ$ with probability p_2. Likewise, (b) corresponds to a mixture with LP_1 oriented at $\phi_1 = 47^\circ$ with probability p_1, and at $\phi_2 = 43^\circ$ with probability p_2.

To summarize, for the present experimental settings, in all the studied examples, the peak values of $\mathcal{I}_{45}^{\alpha\beta}(x,y)$ was of the order of ≈ 1, whereas the $\min[\mathcal{I}_{45}^{\alpha\beta}(x,y)]$ was of the order of ≈ 0.001. Even so, for the studied pure and mixed state examples, $\min[\tilde{\mathcal{I}}_{45}^{\alpha\beta}(x,y)]$ of one order higher, i.e., ≈ 0.01, could be obtained for $\min[\mathcal{I}_{45}^{\alpha\beta}(x,y)]$. This suggests that for the present experimental settings, the error bar in $\tilde{\mathcal{I}}_{45}^{\alpha\beta}(x,y)$ is about 0.001. Thus, with a negative value of $\min[\tilde{\mathcal{I}}_{45}^{\alpha\beta}(x,y)]$ lower than this value, we can safely conclude the presence of polarization-spatial entanglement. While these values are specific to the present experimental settings, the studied examples strongly suggest that the experiment is repeatable for a different experimental setting, such as use of a laser with different power rating, and a camera with different pixel size as well as differing gray scale values.

5.5 Concluding remarks

To conclude, we have outlined a method to detect polarization-spatial entanglement in partially coherent vector light fields through intensity measurements. Partial transpose is implemented through sequential addition of intensities measured at various orientations of the polarizer, and negativity of the added intensities (under partial transpose) is shown to be a sufficient criteria in detecting polarization-spatial entanglement. An experimental demonstration of detection of polarization-spatial entanglement using the outlined method, is car-

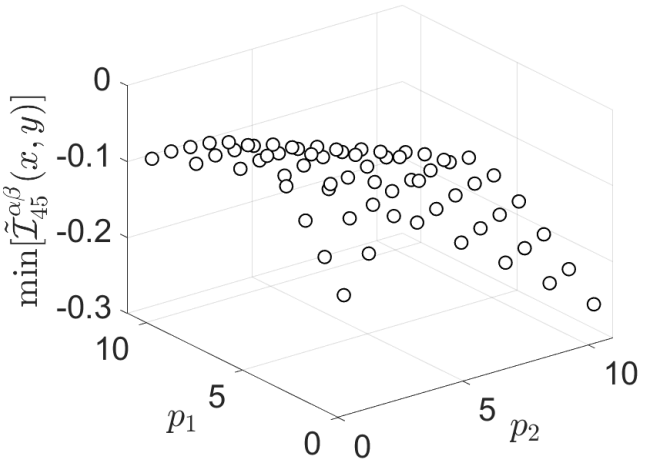

Figure 5.7: ∘ plots the highest negative value obtained on evaluating $\tilde{\mathcal{I}}_{45}^{\alpha\beta}(x,y)$ of (5.11), against the probability of occurrences p_1 and p_2, for a partially coherent light field $\hat{\mathbf{\Gamma}}$, which is a mixture of three different input polarization states, with LP_1 oriented at 43° with probability p_1, at 45° with probability p_2, and at 47° with probability p_3. Here, p_1 is varied from 0 to 1 in intervals of 0.1 and p_2 is varied from 0 to p_1 in intervals of 0.1.

ried out using a Mach-Zehnder interferometer setup. Examples of partially coherent vector light fields, simulated through sequential generation of pure input polarization-spatial entangled states, are shown to violate the obtained criteria thus indicating the presence of polarization-spatial entanglement. While the considered examples are restrictive, the method is general and can be applied to arbitrary partially coherent polarization-spatial states, in detecting entanglement. Further, $2 \times N$ dimensional 'mixed' entangled states, such as those studied in the quantum mechanical context [16–20], can be effectively simulated using partially coherent polarization-spatial entangled light fields, albeit without nonlocality, and the present method can be used to detect entanglement in such a scenario.

Chapter 6

Estimation of dislocated phases in wavefronts through intensity measurements using a Gerchberg-Saxton type algorithm

6.1 Introduction

The complete description of a coherent light field requires the knowledge of both its amplitude as well as its phase. While the amplitude is readily available the phase has to be retrieved from intensity measurements [67, 143–163]. The phase is typically retrieved through iterative algorithms such as the GS algorithm [154] and its variants [67, 145–152, 155, 163], or by solving the transport of intensity equation [156–160], or by making use of a combination of both [161]. Phase can also be retrieved using ptychographic methods as outlined in Refs. [153, 162]. Iterative methods inspired by the GS algorithm have been explored in several works [67, 145–152, 155, 163] both numerically [67, 145–147, 149–152, 155, 163] and experimentally [148]. For instance, in Refs. [146, 150, 151], variants of GS algorithm through use of additional constraints have been explored. Similarly in Refs. [145, 150], GS algorithm with random spatially varying phases modulating the input paraxial light field have been explored. An iterative algorithm using the Shack-Hartmann wavefront sensor has been numerically explored in Ref. [147]. Method using a combination of both transport of intensity equation and GS type iterative algorithm has been explored in Ref. [161]. Nevertheless, the aforementioned methods can suffer from convergence issues, especially when phases with dislocations are present in the problem, see for instance Refs. [143–146]. The methods typically use constraints [146, 150, 151], boundary conditions [160], or guesses on the initial trial phases [146, 150, 161], in arriving

at the solution. In Ref. [148], phase retrieval on a singular light field through measured intensities was demonstrated using an astigmatic lens. The charge was estimated on the input side. Ptychographic methods which use multiple coherent diffracted images of the object towards phase estimation have been demonstrated experimentally in Refs. [153, 162], and they are successful in retrieving phases with dislocations. For instance, in Ref. [153], a non-linear crystal was used in generating multiple diffracted images of a singular light field (in multiple wavelengths) from which the phase (dislocated) was retrieved. Numerical correction of dislocated phases in retrieved phases was outlined in Ref. [164]. Paraxial light fields whose phases have dislocations [67, 77, 91, 146–148, 153, 158, 160–162, 164–191] are known to possess OAM [91], and this aspect has been well explored [67, 77, 148, 153, 162, 166, 167, 169–173, 175–177, 180, 182, 185, 187–191] due to its potential applications such as in free space optical communication [77, 187, 188, 190], imaging [167], optical tweezing and microscopy [191]. Measurement of OAM of light has been explored in Refs. [67, 77, 148, 153, 169, 171, 173, 175–177, 180]. It may be noted that if the phase is unambiguously retrieved, then the OAM is readily evaluated from the measured intensity and the estimated phase [67, 77, 148, 153].

The GS algorithm makes use of the Fourier transform in relating the input and output light field amplitudes [154], which in practice is realized using a convex lens [69]. The phase is then retrieved iteratively using the measured intensities which are the inputs to the algorithm. However as observed in Ref. [67], Fourier transformation conserves the OAM of light, and phases with dislocations do not build naturally in the algorithm, and consequently the algorithm (and its variants) can have convergence issues in this regard, as seen in Refs. [143–146]. To address this issue, an iterative algorithm based on partial Fourier transformation was outlined in Ref. [67]. Partial Fourier transformation does not conserve the OAM of light, and phases with dislocations build naturally in the algorithm. Physical realization of the partial Fourier transformation was outlined in Refs. [67, 135], and several numerical examples which demonstrated unambiguous retrieval of phases with dislocations were presented in Ref. [67]. In this work, we experimentally demonstrate a GS type phase retrieval algorithm using a transformation that is outlined in Refs. [67, 135], which uses a combination of cylindrical lenses that does not conserve OAM. The singular light field is generated by passing a Gaussian light field through a SPP [183, 184] and on free propagation, the light field acquires the charge corresponding to the phase plate which introduces the phase dislocation. Consistent phase retrieval is demonstrated at both the input and output, using three transverse plane intensity measurements. It is noted that the light field emerging from the SPP on free propagation, is not a LG mode but a superposition

of LG modes with the same phase dislocation [186, 192].

The chapter is organized as follows. In Section 6.2 we explain necessary optical transformations and their corresponding realizations used in our algorithm. In Section 6.3 we explain our proposed algorithm and experimental setup. The experimental and the algorithm results are outlined in this section. Finally, we end up with some concluding remarks in Section 6.4.

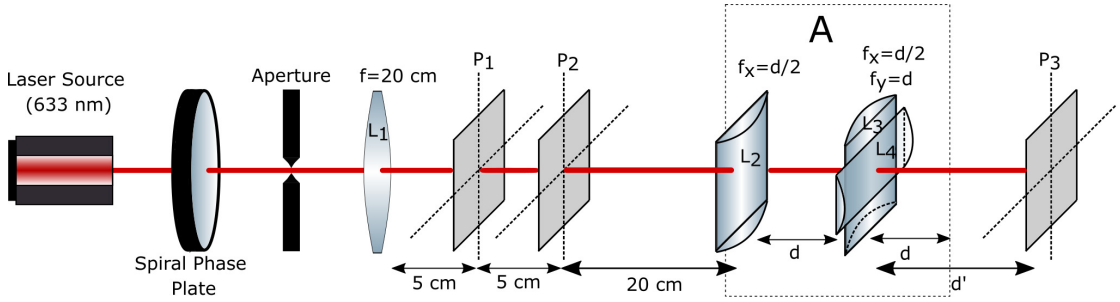

Figure 6.1: Experimental setup. Box A gives the lens arrangement required to perform the unitary transformation corresponding to the ray transfer matrix $\tilde{\mathbf{P}}_y(d)$ [see Eq. (6.5)]. The unitary transformation corresponding to $\tilde{\mathbf{P}}$ simultaneously images the light field $\psi(x, y; z)$ in the x variable in an inverted manner, while Fourier transforming $\psi(x, y; z)$ in the y variable [see Eq. (6.4)]. The lens L_1 is convex, whereas the cylindrical lenses L_2, L_3 and L_4 are plano-convex. Intensity is measured at the three transverse planes P_1, P_2 and P_3. In the present experiment $d = 10$ cm. See Section 6.3 for the details.

6.2 Theoretical analysis

As is well known, Fourier transform in both the x and y variable is realized using a convex lens and free propagation, that is, the ray transfer matrix corresponding to the two dimensional Fourier transformation (unitary) is given by [69, 83, 135]

$$\mathbf{P}(d) = \mathbf{F}(d)\mathbf{L}(d)\mathbf{F}(d) = \begin{bmatrix} 0 & d \\ -1/d & 0 \end{bmatrix} \oplus \begin{bmatrix} 0 & d \\ -1/d & 0 \end{bmatrix}, \tag{6.1}$$

with $d > 0$. Here, $\mathbf{F}(d)$ and $\mathbf{L}(d)$ are ray transfer matrices corresponding to free propagation by distance d and thin lens of focal length d, respectively (see Section 2.1.1). Under the transformation given in Eq. (6.1) a paraxial light field $\psi(x, y; z)$ propagating along the

z-direction, as in Eq. (2.71), is transformed as [69]

$$\tilde{\psi}(\tilde{x},\tilde{y};z)=\frac{1}{i\lambda d}\int_{-\infty}^{\infty}\int_{-\infty}^{\infty}\psi(x,y;z)\exp\left(\frac{-i\kappa}{d}(x\tilde{x}+y\tilde{y})\right)dxdy. \tag{6.2}$$

Note that the GS algorithm uses Eq. 6.2 in retrieving the phase.

In Ref. [67], partial Fourier transform was used towards retrieving the phase, however in the present experimental work we use the unitary transformation whose ray transfer matrix is denoted as $\tilde{\mathbf{P}}$, which is a constituent of the inverse partial-Fourier transformation [67, 135]. The ray transfer matrix $\tilde{\mathbf{P}}$ is given by :

$$\tilde{\mathbf{P}}_y(d)=-\mathbb{1}\oplus\begin{bmatrix}0 & d\\ -1/d & 0\end{bmatrix}. \tag{6.3}$$

The unitary transformation corresponding to $\tilde{\mathbf{P}}$ simultaneously images the light field $\psi(x,y;z)$ in the x variable in an inverted manner, while Fourier transforming $\psi(x,y;z)$ in the y variable. That is, $\psi(x,y;z)$ is transformed as

$$\tilde{\psi}(x,\tilde{y};z)=\sqrt{\frac{1}{i\lambda d}}\int_{-\infty}^{\infty}\psi(-x,y;z)\exp\left(\frac{-i\kappa}{d}(y\tilde{y})\right)dy. \tag{6.4}$$

By Eq. (39) of Ref. [135], the physical realization of the ray transfer matrix $\tilde{\mathbf{P}}_y(d)$ in terms of free propagations and lenses is given by ray transfer matrix composition

$$\tilde{\mathbf{P}}_y(d)=\mathbf{F}(d)\mathbf{L}_x\left(\frac{d}{2}\right)\mathbf{L}_y(d)\mathbf{F}(d)\mathbf{L}_x\left(\frac{d}{2}\right), \tag{6.5}$$

where $\mathbf{L}_x(d)$ and $\mathbf{L}_y(d)$ represent cylindrical lenses of focal length d with their curvatures oriented along the x and y coordinates respectively (see Section 2.1.1). Note that, $\mathbf{L}_x(d)$ corresponds to $\psi(x,y;z)\rightarrow\exp[-i\frac{\kappa}{2d}(x^2)]\psi(x,y;z)$, and $\mathbf{L}_y(d)$ corresponds to the unitary transformation $\psi(x,y;z)\rightarrow\exp[-i\frac{\kappa}{2d}(y^2)]\psi(x,y;z)$ [69]. The schematic of the realization of $\tilde{\mathbf{P}}_y(d)$ [Eq. (6.5)] is outlined in box A of Fig. 6.1. It is readily checked that the unitary transformation corresponding to $\tilde{\mathbf{P}}$ need not conserve OAM τ [see Eq. (2.78)] and can distinguish the signature of τ, since light fields with opposing signatures of τ result in different intensities on passage through $\tilde{\mathbf{P}}$ [67] (see second column of Fig. 6.2). It may be noted that τ is a free propagation invariant [193].

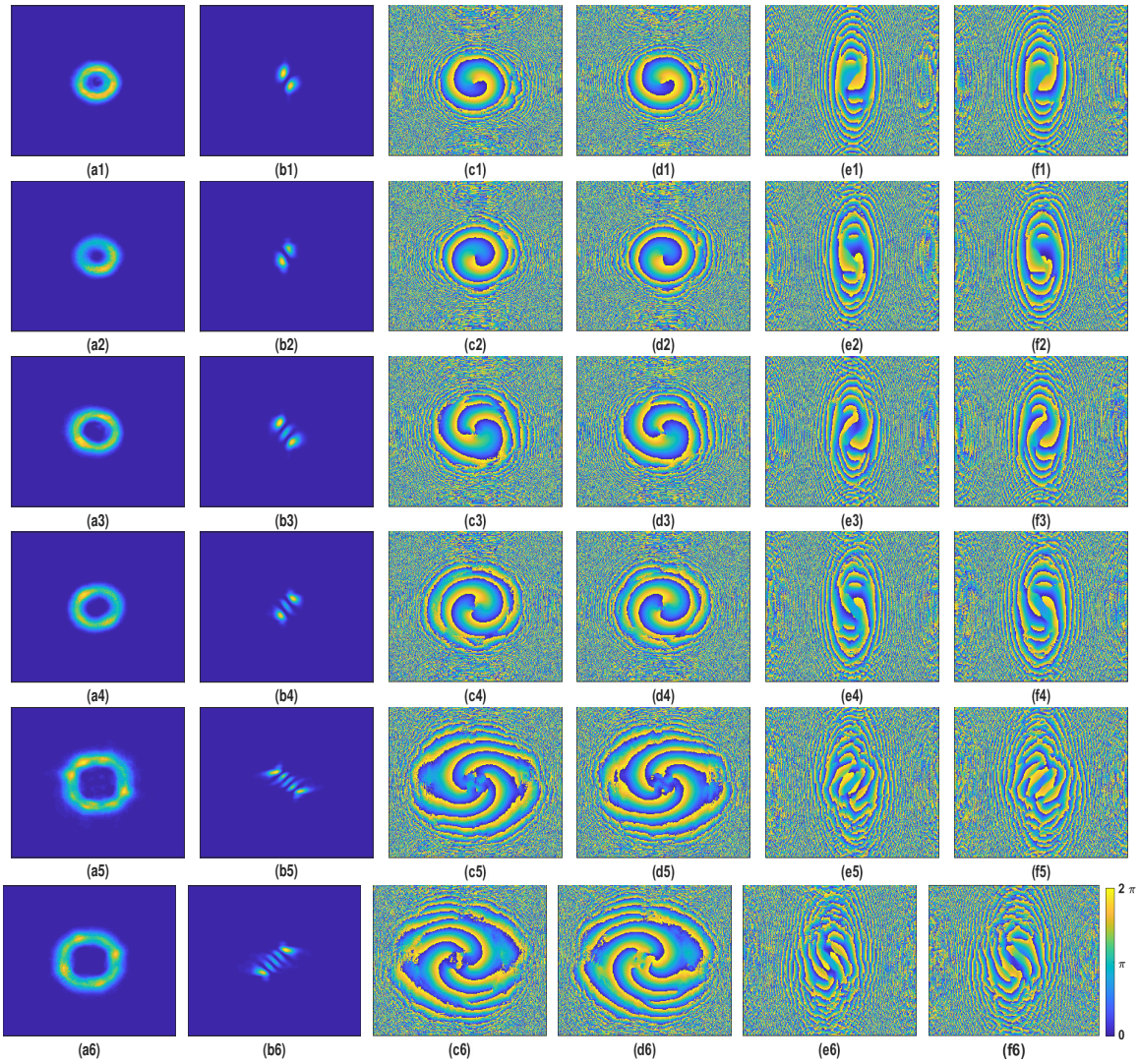

Figure 6.2: Measured intensities at transverse plane P_1 (first column) and transverse plane P_3 (second column) for $d' = 19$ cm. Converged phase of the light field after 500 iterations at transverse planes P_1 for $d' = 19$ and 20 cm (third and fourth column respectively) and P_3 for $d' = 19$ and 20 cm (fifth and sixth column respectively), for input singular light fields of charge ± 1 (first and second row respectively), ± 2 (third and fourth row respectively) and ± 4 (fifth and sixth row respectively). For the first and second column yellow indicates the peak value of the normalized intensities whereas blue indicates the least value which is zero. For the converged phase plots in columns three to six the color map is as shown in (f6). Frame size of all plots are 512×512.

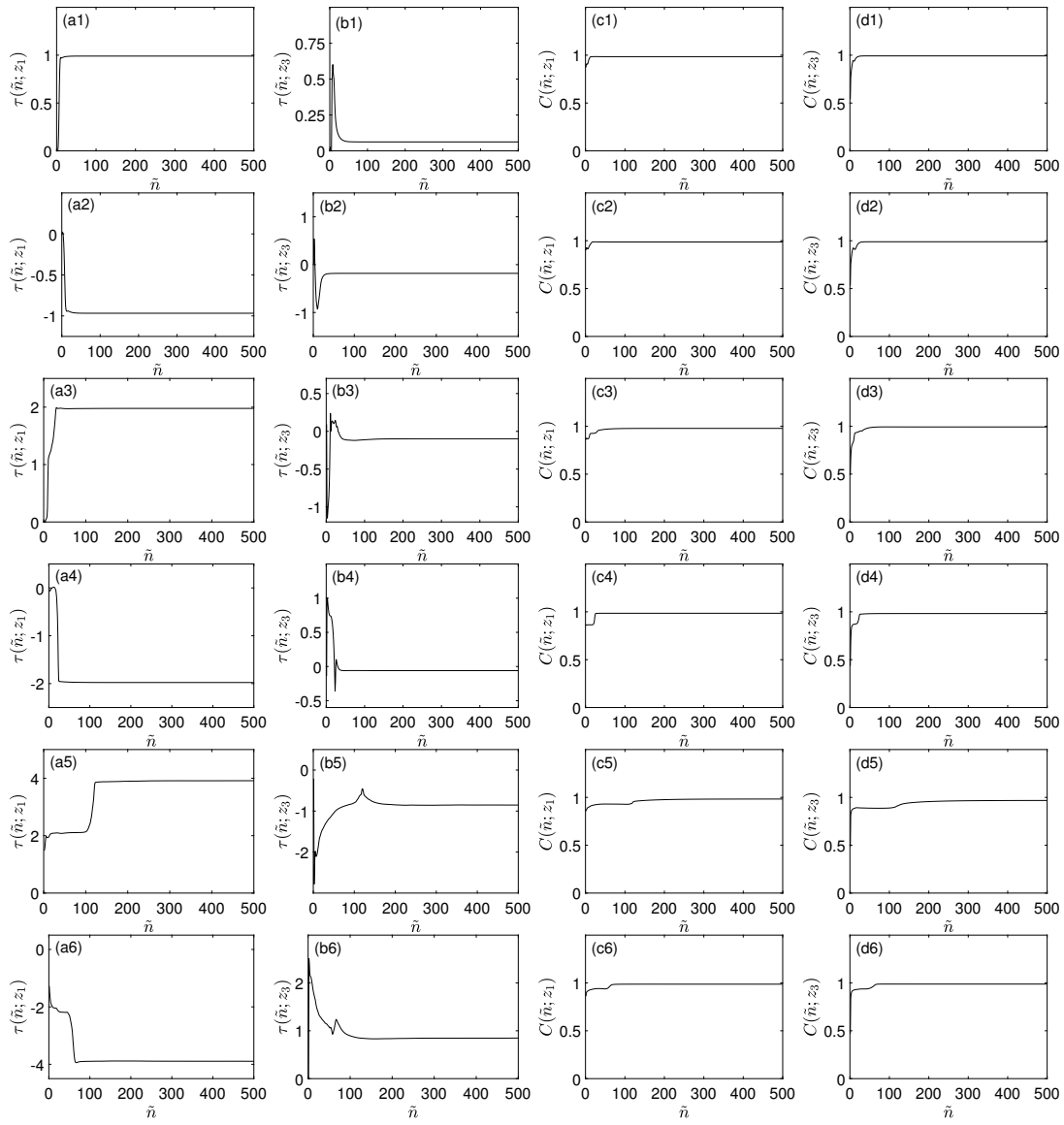

Figure 6.3: Estimated OAM $\tau(\tilde{n}, z_j)$ versus iteration number at transverse plane P_1 (first column) and transverse plane P_3 (second column). Correlation $C(\tilde{n}; z_j)$ versus iteration number at transverse plane P_1 (third column) and transverse plane P_3 (fourth column). Singular light fields of charge ± 1 (first and second row respectively), ± 2 (third and fourth row respectively) and ± 4 (fifth and sixth row respectively). All the plots are for $d' = 19$ cm. See the corresponding rows of Fig. 6.2 for the measured intensities and estimated phases.

6.3 Proposed algorithm and experiment

The experimental setup is as outlined in Fig. 6.1. The Gaussian light field coming out of a 633 nm laser is aligned and passed through a SPP (VPP-m633 from RPC photonics) which reshapes the light field, and we obtain a singular light field on further propagation [186, 192]. The emergent light field has zero intensity in the origin and its phase possesses a dislocation depending on the charge of the SPP intersecting the Gaussian light field. The emergent singular light field is passed through an aperture to filter out the diffractive noise. It is then passed through a convex lens L_1, of focal length 20 cm, which controls the divergence of the light field. The light field coming out of lens L_1 is then passed through the cylindrical lens assembly L_2, L_3 and L_4 in box A (realizing the paraxial transformation $\tilde{\mathbf{P}}_y(d)$, with $d = 10$ cm) which is at a distance of 30 cm from lens L_1. The cylindrical lenses are all plano-convex as outlined in Fig. 6.1 and have the focal lengths 5 cm for lenses L_2 and L_3, and 10 cm for lens L_4. Intensities are measured in planes P_1, P_2, and P_3, as outlined in the figure. While the planes P_1 and P_2 are fixed with the respective distances as outlined in Fig. 6.1, the position of plane P_3 is varied. That is, the distance d' in Fig. 6.1 is taken as 19 cm and 20 cm which also give the location of plane P_3 in the experiment. The intensities measured in planes P_1 (at $z = z_1$), P_2 (at $z = z_2$), and P_3 (at $z = z_3$) are $I(x, y; z_1)$, $I(x, y; z_2)$, and $I(x, y; z_3)$ respectively. Assuming that the light fields at these respective planes are given by $\psi(x, y; z_j) = \sqrt{I(x, y; z_j)} \exp[i\phi(x, y; z_j)]$ with $j = 1, 2, 3$, the goal is to extract the phases $\phi(x, y; z_j)$ from the intensity measurements $I(x, y; z_j)$. This is done using the iterative algorithm which is described as follows.

In the forward direction, we begin with the field amplitude $\sqrt{I(x, y; z_1)}$ at P_1 with the initial trial phase which is assumed to be zero. This field amplitude is numerically Fresnel propagated through a distance of 5 cm in order to obtain $\psi_1(x, y; z_2) = \sqrt{I_1(x, y; z_2)}\mathrm{e}^{i\phi_1(x,y;z_2)}$ at plane P_2. Now $\sqrt{I_1(x, y; z_2)}$ is replaced by $\sqrt{I(x, y; z_2)}$ at P_2, and the resulting field amplitude is numerically Fresnel propagated through a distance of 20 cm, numerically passed through a cylindrical lens of focal length $f_x = 5$ cm, numerically Fresnel propagated through a distance of 10 cm, numerically passed through a cylindrical lens combination of focal length $f_x = 5$ cm and $f_y = 10$ cm, and finally Fresnel propagated numerically through a distance of d' cm. The obtained field amplitude is $\psi_1(x, y; z_3) = \sqrt{I_1(x, y; z_3)}\mathrm{e}^{i\phi_1(x,y;z_3)}$ at plane P_3 and $\sqrt{I_1(x, y; z_3)}$ is replaced by $\sqrt{I(x, y; z_3)}$ at P_3. The process is inverted in the reverse direction to obtain $\psi_1(x, y; z_1) = \sqrt{I_1(x, y; z_1)}\mathrm{e}^{i\phi_1(x,y;z_1)}$ at P_1. Finally, $\sqrt{I_1(x, y; z_1)}$ is replaced with $\sqrt{I(x, y; z_1)}$ at P_1 to repeat the process. The process is repeated $\tilde{n}$ times such that $I_{\tilde{n}}(x, y; z_j) \approx I(x, y; z_j)$, which would then suggest

that the algorithm has converged, and that the estimated phases $\phi_{\tilde{n}}(x, y; z_1)$, $\phi_{\tilde{n}}(x, y; z_2)$, and $\phi_{\tilde{n}}(x, y; z_3)$ are commensurate with the amplitudes $\sqrt{I(x, y; z_1)}$, $\sqrt{I(x, y; z_2)}$, and $\sqrt{I(x, y; z_3)}$. Note that in the numerical implementation, we do not use Eq. (6.4), but rather implement the transformation outlined in the setup of Fig. (6.1) explicitly in terms of Fresnel propagations and action of thin lenses. This is done to avoid differential sampling of the x and y variables present in the numerical implementation of Eq. (6.4).

Since only the measured intensities are available and the phases are unknown, in order to check for the convergence of the algorithm, the correlation $C(\tilde{n}; z_j)$ between the measured intensity $I(x, y; z_j)$, and the estimated intensity $I_{\tilde{n}}(x, y, z_j)$, is evaluated at the transverse planes P_1, P_2 and P_3 for every iteration. The intensity correlation is defined as [143, 155] :

$$C(\tilde{n}; z_j) = \frac{1}{\mathrm{N}_1 \mathrm{N}_2} \left| \int_{-\infty}^{\infty} \int_{-\infty}^{\infty} I(x, y; z_j) I_{\tilde{n}}(x, y; z_j) dx dy \right|, \tag{6.6}$$

where

$$\mathrm{N}_1 = \left[\int_{-\infty}^{\infty} \int_{-\infty}^{\infty} I(x, y; z_j) I(x, y; z_j) dx dy \right]^{\frac{1}{2}} \quad \text{and} \tag{6.7}$$

$$\mathrm{N}_2 = \left[\int_{-\infty}^{\infty} \int_{-\infty}^{\infty} I_{\tilde{n}}(x, y; z_j) I_{\tilde{n}}(x, y; z_j) dx dy \right]^{\frac{1}{2}}. \tag{6.8}$$

The algorithm is said to have 'converged' when $C(\tilde{n}; z_j) \approx 1$ after $\tilde{n}$ iterations. Similarly, the OAM τ, outlined in Eq. 2.78, is evaluated at every iteration at transverse planes P_1, P_2 and P_3 and the estimated OAM is denoted as $\tau(\tilde{n}; z_j)$. Consistency of the algorithm is checked by comparing the estimated values of the OAM $\tau(\tilde{n}; z_j)$ in planes P_1 and P_2, by varying P_3, for a given charge introduced by the SPP.

The intensities at the three planes were recorded using a CCD camera which has 1392×1040 pixels with pixel size $6.45\,\mu$m. The measured intensities were truncated to 512×512 pixels, since the measured intensities were well captured in all the three planes in the truncated region. Fifty intensity samples were taken at each transverse plane and averaged to suppress point wise intensity fluctuation. A background zero frequency component was subtracted from the measured intensities to suppress background noise and the intensity in each of the three planes was normalized before being fed in to the algorithm. The length of the grid was chosen to be 3.3024 mm with $d = 10$ cm and wavelength $\lambda = 633$ nm.

Table 6.1: Here we list the converged OAM values $\tau(500; z_j)$ and intensity correlation values after 500 iterations $C(500; z_j)$, corresponding to the input singular light field of charge varying from -4 to 4, at planes P_1, P_2 and P_3 for $d' = 19$ and 20 cm.

Charge	Transverse	$\tau(500; z_j)$		$C(500; z_j)$	
on SPP	plane	19	20	19	20
-4	P_1	-3.90	-3.94	0.99	0.98
	P_2	-3.90	-3.93	0.99	0.98
	P_3	0.85	0.78	0.99	0.98
-3	P_1	-2.90	-2.88	0.99	0.99
	P_2	-2.90	-2.86	0.99	0.99
	P_3	0.26	0.20	0.99	0.98
-2	P_1	-1.98	-1.98	0.99	0.99
	P_2	-1.99	-1.98	0.98	0.99
	P_3	-0.06	-0.03	0.98	0.98
-1	P_1	-0.97	-0.97	0.99	0.99
	P_2	-0.96	-0.97	0.99	0.99
	P_3	-0.18	-0.20	0.99	0.99
1	P_1	0.99	0.99	0.99	0.98
	P_2	0.99	0.99	0.99	0.99
	P_3	0.06	0.05	0.99	0.99
2	P_1	1.98	1.98	0.98	0.98
	P_2	1.99	1.98	0.98	0.98
	P_3	-0.10	-0.05	0.99	0.99
3	P_1	2.90	2.94	0.99	0.98
	P_2	2.93	2.95	0.99	0.98
	P_3	0.07	0.02	0.99	0.99
4	P_1	3.92	3.93	0.98	0.99
	P_2	3.90	3.90	0.99	0.99
	P_3	-0.85	-0.92	0.97	0.97

Eight singular light fields with charge varying from -4 through 4 were studied and for each such light field two variations with $d' = 19$ and 20 cm were considered. Field amplitudes with negative charges were obtained by reversing the orientation of the phase plate. First and second column of Fig. 6.2 plot the intensities measured at transverse planes P_1 and P_3 for $d' = 19$ cm, respectively. Third and fourth column of Fig. 6.2 plot the converged phases of the light field after 500 iterations at transverse plane P_1 for $d' = 19$ and 20 cm respectively, whereas fifth and sixth column of Fig. 6.2 plot the converged phases at transverse plane P_3 for $d' = 19$ and 20 cm respectively. Rows one to six of Fig. 6.2

correspond to input singular light fields of charge values ± 1, ± 2 and ± 4 respectively. The estimated OAM $\tau(\tilde{n}; z_j)$ versus the iteration number $\tilde{n}$ and the correlation $C(\tilde{n}; z_j)$ versus the iteration number $\tilde{n}$ is plotted in Fig. 6.3, for the examples considered in Fig. 6.2. The rows of Fig. 6.2 are in correspondence with rows of Fig. 6.3. First and second column of Fig. 6.3 plot the OAM τ at every iteration at transverse planes P_1 and P_3 respectively for $d' = 19$ cm, whereas third and fourth column of Fig. 6.3 plot correlation $C(\tilde{n}; z_j)$ at every iteration at transverse planes P_1 and P_3 respectively for $d' = 19$ cm. In all the considered examples the values of the OAM $\tau(\tilde{n}; z_j)$ and the intensity correlation values $C(\tilde{n}; z_j)$ stagnated in less than 500 iterations, and the stagnated values of $C(\tilde{n}; z_j)$ were reasonably close to 1 as seen in Fig. 6.3. The converged values of $\tau(\tilde{n}; z_j)$ in planes P_1 and P_2 were also found to be close to the charge value of the inserted SPP. Even so, fractional but consistent values of $\tau(\tilde{n}; z_j)$ were obtained in P_3 for varying d'. The converged values of the OAM $\tau(\tilde{n}; z_j)$ and the correlation value $C(\tilde{n}; z_j)$ obtained at the 500^{th} iteration for the studied samples is summarized in Table 6.1. It may be noted that the OAM acquired by the light field on insertion of the SPP is constant even if there is a slight misalignment between the in coming laser light field and the SPP [185]. Even so, in the present experiment, the obtained accuracy is only up to the second digit after the decimal in the estimated OAM $\tau(\tilde{n}; z_j)$, as seen in Table 6.1. This can be attributed to the fluctuation of the measured intensities. Further, we have significantly lesser OAM $\tau(\tilde{n}; z_3)$ in plane P_3 as compared to planes P_1 and P_2, and this is a consequence of the fact that the transformation corresponding to $\tilde{\mathbf{P}}$, does not conserve the OAM. Nevertheless, the fact it is non zero at plane P_3 can be attributed to the circular asymmetry of the input light field caused by the slight misalignment of the incoming laser light field with the SPP.

6.4 Concluding remarks

To conclude, we have experimentally demonstrated the extraction of phases with dislocations using a GS type algorithm from transverse plane intensity measurements on singular light fields. We have also demonstrated the extraction of phases of field amplitudes at the output, which possess fractional OAM. The work experimentally substantiates the method outlined in Ref. [67]. Since the method does not impose any constraints on the mode expansion of the light field, it is generic in extracting the dislocated phases from intensity measurements. Consequently, the mode expansion, the OAM, and the radial-angular entanglement [68] of the light field, can be extracted from the estimated field amplitudes in a straight forward manner, at both the input and output transverse planes.

Chapter 7

Conclusion, possible applications, and future scope

7.1 Conclusion

In this thesis we explored some aspects of entanglement in paraxial light fields using methods typically used in the classical domain. We have presented a method for detecting polarization-spatial entanglement in coherent vectorial paraxial light fields by observing fringe movement resulting from the rotation of a linear polarizer. This fringe movement has been shown as a sufficient criterion for detection of polarization-spatial entanglement in such light fields. Through experimental demonstration we have shown that close to 1 ebit of polarization-spatial entanglement can be achieved using solely Gaussian spatial modes with orthogonal polarizations, even when there is a significant overlap between the spatial modes. Furthermore, we have showcased the tunability of polarization-spatial Gaussian entanglement by varying the polarization of the input in a folded Mach-Zehnder interferometer setup.

We have studied polarization-spatial entanglement in partially coherent vector light fields, which is equivalent to mixed state qubit-harmonic oscillator mode entanglement. We introduced a generalized uncertainty principle that is suited for polarization spatial degrees of freedom. Partial transpose, which was originally introduced in the quantum mechanical context, was implemented through the obtained generalized uncertainty principle. It was shown to be necessary and sufficient in detecting polarization- spatial entanglement for a class of states which have their spatial part to be Gaussian. Additionally, we proposed an experimental approach to realize such entangled states.

We have presented a method for detecting polarization-spatial entanglement in partially coherent vector light fields using intensity measurements. The implementation of

partial transpose is achieved by sequentially adding intensities obtained from measurements at different polarizer orientations. We have established that the negativity of the intensity thus obtained (after sequential addition), serves as a sufficient criterion for detecting polarization-spatial entanglement. To demonstrate the effectiveness of our method, we conducted an experimental verification of polarization-spatial entanglement detection, using a Mach-Zehnder interferometer setup. By simulating partially coherent vector light fields through the sequential generation of pure input polarization-spatial entangled states, we observed violations of the criterion, indicating the presence of polarization-spatial entanglement.

Our experimental study successfully demonstrated the extraction of phases with dislocations from singular light fields by employing a GS type algorithm and utilizing transverse plane intensity measurements. Additionally, we showcased the extraction of phases associated with field amplitudes possessing fractional OAM. This experimental verification provides substantial support to the methodology outlined in the Ref. [67]. One of the key advantages of our method is its generality in extracting dislocated phases from intensity measurements, as it does not impose any constraints on the mode expansion of the light field. Consequently, the method allows for straightforward extraction of the mode expansion, the OAM, and the radial-angular entanglement of the light field from the estimated field amplitudes. This capability holds true for both the input and output transverse planes.

7.2 Possible applications and future scope

According to the Schmidt decomposition, the presence of orthogonal modes has traditionally been considered necessary for achieving maximal entanglement. This requirement often necessitated complex experimental setups utilizing devices such as SLMs, dove prisms, and digital micromirror devices. However, our research has demonstrated an alternative approach. We have shown that two Gaussian light fields, with a small relative tilt and substantial spatial overlap, along with orthogonal polarizations, can exhibit near-maximal entanglement. This discovery has significant implications for various applications where maximal entanglement is desired. Importantly, we were able to achieve this high degree of entanglement without resorting to higher-order spatial modes or relying on complex experimental setups. Our findings suggest that even with simple experimental setups and fundamental Gaussian beams, it is possible to achieve entangled states that closely approach maximal entanglement. This opens up new possibilities for practical implementation and simplifies the experimental requirements in areas where maximal entanglement is sought

after.

We have studied polarization-spatial entanglement in partially coherent vector light fields and have settled the issue of separability for a class of states that have their spatial part to be Gaussian. Bound entanglement is not present in such states. However, the broad range of possibilities offered by the polarization-spatial degrees of freedom suggests that classical optical vector light fields can effectively simulate and exhibit exotic quantum phenomena, including bound entanglement. This observation highlights the relevance of our work, particularly in the current scientific interest surrounding bipartite entanglement, not only in vector paraxial wave optics [6, 7, 27, 29, 30, 33, 34, 36–38, 45–47, 127–129] but also in quantum optical systems [16–20, 120–126]. While our study has yielded definite conclusions regarding bipartite entanglement for a specific class of states and their potential experimental generation, further work remains to be done. Specifically, it is necessary to conduct experiments to generate the entanglement and verify it through the uncertainty principle. These experimental aspects and validation of the generated entanglement need to be explored.

We have introduced a method for detecting polarization-spatial entanglement in partially coherent vector light fields by utilizing intensity measurements. Although the examples we considered were limited in scope, the method itself is applicable to arbitrary partially coherent polarization-spatial states for entanglement detection. Furthermore, our approach allows for the effective simulation of $2 \times N$ dimensional 'mixed' entangled states, similar to those studied in the quantum mechanical context [16–20]. These simulations, achieved using partially coherent polarization-spatial entangled light fields, lack non-locality. Nonetheless, our method remains capable of detecting entanglement in such scenarios.

Through our experimental work, we have provided a demonstration of successfully extracting phases with dislocations from singular light fields. This extraction was achieved using a GS type algorithm that utilizes transverse plane intensity measurements. Our experimental results validate the effectiveness of this algorithm in accurately capturing the phase information associated with dislocations present in the light fields. The proposed method is highly versatile as it does not impose any constraints on the mode expansion of the light field. This generic approach allows for the straightforward extraction of various properties, including the mode expansion, the OAM, and the radial-angular entanglement [68], from the estimated field amplitudes. This extraction can be performed with ease at both the input and output transverse planes, enabling a comprehensive understanding of the light field's characteristics. While the evaluation of OAM of the light field (from the estimated field

amplitude) is already presented in Chapter 6, detection and evaluation of other properties such as radial-angular entanglement and mode expansion of the light field needs to be explored. Also, other first-order optical systems known to not conserve OAM of the incoming light field could in principle be used to retrieve phases with dislocations. Such an attempt was done using a first-order optical system consisting of only two cylindrical lenses, and we were not only able to estimate phases with dislocations, we were also able to generate fractional (tunable) OAM [194].

Bibliography

[1] P. L. Knight, E. Roldán, and J. E. Sipe, "Quantum walk on the line as an interference phenomenon," *Physical Review A*, vol. 68, no. 2, p. 020301, 2003.

[2] F. Elster, S. Barkhofen, T. Nitsche, J. Novotný, A. Gábris, I. Jex, and C. Silberhorn, "Quantum walk coherences on a dynamical percolation graph," *Scientific Reports*, vol. 5, no. 1, p. 13495, 2015.

[3] S. K. Goyal, F. S. Roux, A. Forbes, and T. Konrad, "Implementing quantum walks using orbital angular momentum of classical light," *Physical Review Letters*, vol. 110, no. 26, p. 263602, 2013.

[4] H. Jeong, M. Paternostro, and M. S. Kim, "Simulation of quantum random walks using the interference of a classical field," *Physical Review A*, vol. 69, no. 1, p. 012310, 2004.

[5] D. Pandey, N. Satapathy, M. S. Meena, and H. Ramachandran, "Quantum walk of light in frequency space and its controlled dephasing," *Physical Review A*, vol. 84, no. 4, p. 042322, 2011.

[6] B. P. da Silva, M. A. Leal, C. E. R. Souza, E. F. Galvão, and A. Z. Khoury, "Spin-orbit laser mode transfer via a classical analogue of quantum teleportation," *Journal of Physics B: Atomic, Molecular and Optical Physics*, vol. 49, no. 5, p. 055501, 2016.

[7] D. Guzman-Silva, R. Brüning, F. Zimmermann, C. Vetter, M. Gräfe, M. Heinrich, S. Nolte, M. Duparré, A. Aiello, M. Ornigotti, and A. Szameit, "Demonstration of local teleportation using classical entanglement," *Laser & Photonics Reviews*, vol. 10, no. 2, pp. 317–321, 2016.

[8] M. R. Andrews, C. G. Townsend, H.-J. Miesner, D. S. Durfee, D. M. Kurn, and W. Ketterle, "Observation of interference between two Bose condensates," *Science*, vol. 275, no. 5300, pp. 637–641, 1997.

[9] Z. Hadzibabic, S. Stock, B. Battelier, V. Bretin, and J. Dalibard, "Interference of an array of independent Bose-Einstein condensates," *Physical Review Letters*, vol. 93, no. 18, p. 180403, 2004.

[10] A. Burchianti, C. D'Errico, L. Marconi, F. Minardi, C. Fort, and M. Modugno, "Effect of interactions in the interference pattern of Bose-Einstein condensates," *Physical Review A*, vol. 102, no. 4, p. 043314, 2020.

[11] M. Arndt, O. Nairz, J. Vos-Andreae, C. Keller, G. Van der Zouw, and A. Zeilinger, "Wave-particle duality of c_{60} molecules," *Nature*, vol. 401, no. 6754, pp. 680–682, 1999.

[12] A. D. Cronin, J. Schmiedmayer, and D. E. Pritchard, "Optics and interferometry with atoms and molecules," *Reviews of Modern Physics*, vol. 81, no. 3, pp. 1051–1129, 2009.

[13] C. Brand, F. Kiałka, S. Troyer, C. Knobloch, K. Simonović, B. A. Stickler, K. Hornberger, and M. Arndt, "Bragg diffraction of large organic molecules," *Physical Review Letters*, vol. 125, no. 3, p. 033604, 2020.

[14] R. Horodecki, P. Horodecki, M. Horodecki, and K. Horodecki, "Quantum entanglement," *Reviews of Modern Physics*, vol. 81, no. 2, pp. 865–942, 2009.

[15] O. Gühne and G. Tóth, "Entanglement detection," *Physics Reports*, vol. 474, no. 1-6, pp. 1–75, 2009.

[16] H. Yuan and S. Lloyd, "Controllability of the coupled spin-$\frac{1}{2}$ harmonic oscillator system," *Physical Review A*, vol. 75, no. 5, p. 052331, 2007.

[17] M. Schlosshauer, A. P. Hines, and G. J. Milburn, "Decoherence and dissipation of a quantum harmonic oscillator coupled to two-level systems," *Physical Review A*, vol. 77, no. 2, p. 022111, 2008.

[18] S. Krastanov, V. V. Albert, C. Shen, C.-L. Zou, R. W. Heeres, B. Vlastakis, R. J. Schoelkopf, and L. Jiang, "Universal control of an oscillator with dispersive coupling to a qubit," *Physical Review A*, vol. 92, no. 4, p. 040303, 2015.

[19] D. Von Lindenfels, O. Gräb, C. T. Schmiegelow, V. Kaushal, J. Schulz, M. T. Mitchison, J. Goold, F. Schmidt-Kaler, and U. G. Poschinger, "Spin heat engine coupled to a harmonic-oscillator flywheel," *Physical Review Letters*, vol. 123, no. 8, p. 080602, 2019.

[20] X. F. Qian, C. J. Broadbent, and J. H. Eberly, "Bell violation for unknown continuous-variable states," *New Journal of Physics*, vol. 16, no. 1, p. 013033, 2014.

[21] R. F. Werner and M. M. Wolf, "Bound entangled Gaussian states," *Physical Review Letters*, vol. 86, no. 16, p. 3658, 2001.

[22] A. Serafini, G. Adesso, and F. Illuminati, "Unitarily localizable entanglement of Gaussian states," *Physical Review A*, vol. 71, no. 3, p. 032349, 2005.

[23] J. S. Ivan, N. Mukunda, and R. Simon, "Generation and distillation of non-Gaussian entanglement from nonclassical photon statistics," *Quantum Information Processing*, vol. 11, pp. 873–885, 2012.

[24] M. Horodecki, P. Horodecki, and R. Horodecki, "Mixed-state entanglement and distillation: Is there a "bound" entanglement in nature?," *Physical Review Letters*, vol. 80, no. 24, p. 5239, 1998.

[25] K. H. Kagalwala, G. Di Giuseppe, A. F. Abouraddy, and B. E. A. Saleh, "Bell's measure in classical optical coherence," *Nature Photonics*, vol. 7, no. 1, pp. 72–78, 2013.

[26] R. J. C. Spreeuw, "A classical analogy of entanglement," *Foundations of Physics*, vol. 28, no. 3, pp. 361–374, 1998.

[27] X.-F. Qian and J. H. Eberly, "Entanglement and classical polarization states," *Optics Letters*, vol. 36, no. 20, pp. 4110–4112, 2011.

[28] A. Aiello, F. Töppel, C. Marquardt, E. Giacobino, and G. Leuchs, "Quantum-like nonseparable structures in optical beams," *New Journal of Physics*, vol. 17, no. 4, p. 043024, 2015.

[29] F. Töppel, A. Aiello, C. Marquardt, E. Giacobino, and G. Leuchs, "Classical entanglement in polarization metrology," *New Journal of Physics*, vol. 16, no. 7, p. 073019, 2014.

[30] S. Berg-Johansen, F. Töppel, B. Stiller, P. Banzer, M. Ornigotti, E. Giacobino, G. Leuchs, A. Aiello, and C. Marquardt, "Classically entangled optical beams for high-speed kinematic sensing," *Optica*, vol. 2, no. 10, pp. 864–868, 2015.

[31] P. Ghose and A. Mukherjee, "Entanglement in classical optics," *Reviews in Theoretical Science*, vol. 2, no. 4, pp. 274–288, 2014.

[32] J. H. Eberly, X.-F. Qian, A. Al Qasimi, H. Ali, M. A. Alonso, R. Gutiérrez-Cuevas, B. J. Little, J. C. Howell, T. Malhotra, and A. N. Vamivakas, "Quantum and classical optics-emerging links," *Physica Scripta*, vol. 91, no. 6, p. 063003, 2016.

[33] M. McLaren, T. Konrad, and A. Forbes, "Measuring the nonseparability of vector vortex beams," *Physical Review A*, vol. 92, no. 2, p. 023833, 2015.

[34] X.-F. Qian, B. Little, J. C. Howell, and J. H. Eberly, "Shifting the quantum-classical boundary: theory and experiment for statistically classical optical fields," *Optica*, vol. 2, no. 7, pp. 611–615, 2015.

[35] R. J. C. Spreeuw, "Classical wave-optics analogy of quantum-information processing," *Physical Review A*, vol. 63, no. 6, p. 062302, 2001.

[36] C. V. S. Borges, M. Hor-Meyll, J. A. O. Huguenin, and A. Z. Khoury, "Bell-like inequality for the spin-orbit separability of a laser beam," *Physical Review A*, vol. 82, no. 3, p. 033833, 2010.

[37] G. Milione, T. A. Nguyen, J. Leach, D. A. Nolan, and R. R. Alfano, "Using the nonseparability of vector beams to encode information for optical communication," *Optics Letters*, vol. 40, no. 21, pp. 4887–4890, 2015.

[38] P. Li, B. Wang, and X. Zhang, "High-dimensional encoding based on classical nonseparability," *Optics express*, vol. 24, no. 13, pp. 15143–15159, 2016.

[39] B. Ndagano, B. Perez-Garcia, F. S. Roux, M. McLaren, C. Rosales-Guzman, Y. Zhang, O. Mouane, R. I. Hernandez-Aranda, T. Konrad, and A. Forbes, "Characterizing quantum channels with non-separable states of classical light," *Nature Physics*, vol. 13, no. 4, pp. 397–402, 2017.

[40] B. Perez-Garcia, J. Francis, M. McLaren, R. I. Hernandez-Aranda, A. Forbes, and T. Konrad, "Quantum computation with classical light: The Deutsch Algorithm," *Physics Letters A*, vol. 379, no. 28-29, pp. 1675–1680, 2015.

[41] A. F. Abouraddy, K. H. Kagalwala, and B. E. Saleh, "Two-point optical coherency matrix tomography," *Optics Letters*, vol. 39, no. 8, pp. 2411–2414, 2014.

[42] K. H. Kagalwala, H. E. Kondakci, A. F. Abouraddy, and B. E. Saleh, "Optical coherency matrix tomography," *Scientific Reports*, vol. 5, no. 1, p. 15333, 2015.

[43] X.-F. Qian, T. Malhotra, A. N. Vamivakas, and J. H. Eberly, "Coherence constraints and the last hidden optical coherence," *Physical Review Letters*, vol. 117, no. 15, p. 153901, 2016.

[44] C. Okoro, H. E. Kondakci, A. F. Abouraddy, and K. C. Toussaint, "Demonstration of an optical-coherence converter," *Optica*, vol. 4, no. 9, pp. 1052–1058, 2017.

[45] B. N. Simon, S. Simon, F. Gori, M. Santarsiero, R. Borghi, N. Mukunda, and R. Simon, "Nonquantum entanglement resolves a basic issue in polarization optics," *Physical Review Letters*, vol. 104, no. 2, p. 023901, 2010.

[46] N. Sandeau, H. Akhouayri, A. Matzkin, and T. Durt, "Experimental violation of Tsirelson's bound by Maxwell fields," *Physical Review A*, vol. 93, no. 5, p. 053829, 2016.

[47] E. Otte, I. Nape, C. Rosales-Guzmán, A. Vallés, C. Denz, and A. Forbes, "Recovery of nonseparability in self-healing vector Bessel beams," *Physical Review A*, vol. 98, no. 5, p. 053818, 2018.

[48] S. A. Ponomarenko, "Twist phase and classical entanglement of partially coherent light," *Optics Letters*, vol. 46, no. 23, pp. 5958–5961, 2021.

[49] S. Arun and J. S. Ivan, "Polarisation-spatial entanglement upon reflection across a dielectric," *Optics Communications*, vol. 511, p. 128006, 2022.

[50] Y. Shen and C. Rosales-Guzmán, "Nonseparable states of light: from quantum to classical," *Laser & Photonics Reviews*, vol. 16, no. 7, p. 2100533, 2022.

[51] A. Aiello, X.-B. Hu, V. Rodríguez-Fajardo, A. Forbes, R. I. Hernandez-Aranda, B. Perez-Garcia, and C. Rosales-Guzmán, "A non-separability measure for spatially disjoint vectorial fields," *New Journal of Physics*, vol. 24, no. 6, p. 063032, 2022.

[52] Yao-Li, X.-B. Hu, B. Perez-Garcia, Bo-Zhao, W. Gao, Z.-H. Zhu, and C. Rosales-Guzman, "Classically entangled Ince-Gaussian modes," *Applied Physics Letters*, vol. 116, no. 22, p. 221105, 2020.

[53] M. A. Goldin, D. Francisco, and S. Ledesma, "Simulating Bell inequality violations with classical optics encoded qubits," *Journal of Optical Society of America B*, vol. 27, no. 4, pp. 779–786, 2010.

[54] H. E. Kondakci, M. A. Alonso, and A. F. Abouraddy, "Classical entanglement underpins the invariant propagation of space-time wave packets," *Optics Letters*, vol. 44, no. 11, pp. 2645–2648, 2019.

[55] A. Forbes, A. Aiello, and B. Ndagano, "Classically entangled light," *Progress in Optics*, vol. 64, pp. 99–153, 2019.

[56] C. T. Samlan and N. K. Viswanathan, "Generation of vector beams using a double-wedge depolarizer: Non-quantum entanglement," *Optics and Lasers in Engineering*, vol. 82, pp. 135–140, 2016.

[57] X. Song, Y. Sun, P. Li, H. Qin, and X. Zhang, "Bell's measure and implementing quantum Fourier transform with orbital angular momentum of classical light," *Scientific Reports*, vol. 5, no. 1, p. 14113, 2015.

[58] L. J. Pereira, A. Z. Khoury, and K. Dechoum, "Quantum and classical separability of spin-orbit laser modes," *Physical Review A*, vol. 90, no. 5, p. 053842, 2014.

[59] S. Prabhakar, S. G. Reddy, A. Aadhi, C. Perumangatt, G. K. Samanta, and R. P. Singh, "Violation of Bell's inequality for phase-singular beams," *Physical Review A*, vol. 92, no. 2, p. 023822, 2015.

[60] A. Peres, "Separability criterion for density matrices," *Physical Review Letters*, vol. 77, no. 8, pp. 1413–1415, 1996.

[61] M. Horodecki, P. Horodecki, and R. Horodecki, "Separability of mixed states: necessary and sufficient conditions," *Physics Letters A*, vol. 223, pp. 1–8, 1996.

[62] P. Horodecki, "Separability criterion and inseparable mixed states with positive partial transposition," *Physics Letters A*, vol. 232, no. 5, pp. 333–339, 1997.

[63] R. Simon, "Peres-Horodecki separability criterion for continuous variable systems," *Physical Review Letters*, vol. 84, no. 12, p. 2726, 2000.

[64] G. Tóth and O. Gühne, "Entanglement and permutational symmetry," *Physical Review Letters*, vol. 102, no. 17, p. 170503, 2009.

[65] B. Zhao, X.-B. Hu, V. Rodríguez-Fajardo, A. Forbes, W. Gao, Z.-H. Zhu, and C. Rosales-Guzmán, "Determining the non-separability of vector modes with digital micromirror devices," *Applied Physics Letters*, vol. 116, no. 9, p. 091101, 2020.

[66] M. A. Nielsen and I. L. Chuang, *Quantum computation and quantum information*. Cambridge university press, 2004.

[67] P. A. A. Yasir and J. S. Ivan, "Estimation of phases with dislocations in paraxial wave fields from intensity measurements," *Physical Review A*, vol. 97, no. 2, p. 023817, 2018.

[68] S. Asokan and J. S. Ivan, "Radial-angular entanglement in Laguerre-Gaussian mode superpositions," *Journal of Optical Society of America A*, vol. 35, no. 5, pp. 785–793, 2018.

[69] J. W. Goodman, *Introduction to Fourier optics*. Roberts and Company publishers, 2005.

[70] M. Born and E. Wolf, *Principles of Optics: Electromagnetic Theory of Propagation, Interference and Diffraction of Light*. Elsevier, 2013.

[71] A. E. Siegman, *Lasers*. University Science books, 1986.

[72] H. Kogelnik and T. Li, "Laser beams and resonators," *Applied Optics*, vol. 5, no. 10, pp. 1550–1567, 1966.

[73] D. J. Griffiths, *Introduction to Electrodynamics*. Prentice Hall, 1999.

[74] G. B. Arfken and H. J. Weber, *Mathematical methods for physicists*. Elsevier, 2005.

[75] M. W. Beijersbergen, L. Allen, H. E. L. O. van der Veen, and J. P. Woerdman, "Astigmatic laser mode converters and transfer of orbital angular momentum," *Optics Communications*, vol. 96, no. 1-3, pp. 123–132, 1993.

[76] R. Simon, K. Sundar, and N. Mukunda, "Twisted Gaussian Schell-model beams. I. Symmetry structure and normal-mode spectrum," *Journal of Optical Society of America A*, vol. 10, no. 9, pp. 2008–2016, 1993.

[77] V. Madhu and J. S. Ivan, "Robustness of the twist parameter of Laguerre-Gaussian mode superpositions against atmospheric turbulence," *Physical Review A*, vol. 95, no. 4, p. 043836, 2017.

[78] H. Bacry and M. Cadilhac, "Metaplectic group and Fourier optics," *Physical Review A*, vol. 23, no. 5, p. 2533, 1981.

[79] R. Simon, E. C. G. Sudarshan, and N. Mukunda, "Gaussian-Wigner distributions in quantum mechanics and optics," *Physical Review A*, vol. 36, no. 8, p. 3868, 1987.

[80] Arvind, B. Dutta, N. Mukunda, and R. Simon, "The real symplectic groups in quantum mechanics and optics," *Pramana*, vol. 45, pp. 471–497, 1995.

[81] D. Stoler, "Operator methods in physical optics," *Journal of Optical Society of America*, vol. 71, no. 3, pp. 334–341, 1981.

[82] E. C. G. Sudarshan, N. Mukunda, and R. Simon, "Realization of first order optical systems using thin lenses," *Optica Acta*, vol. 32, pp. 855–872, 1985.

[83] P. A. A. Yasir and J. S. Ivan, "Realization of first-order optical systems using thin convex lenses of fixed focal length," *Journal of Optical Society of America A*, vol. 31, no. 9, pp. 2011–2020, 2014.

[84] R. Simon, E. C. G. Sudarshan, and N. Mukunda, "Generalized rays in first-order optics: transformation properties of Gaussian Schell-model fields," *Physical Review A*, vol. 29, no. 6, p. 3273, 1984.

[85] R. Simon, E. C. G. Sudarshan, and N. Mukunda, "Gaussian Wigner distributions: a complete characterization," *Physics Letters A*, vol. 124, no. 4-5, pp. 223–228, 1987.

[86] L. Mandel and E. Wolf, *Optical coherence and quantum optics*. Cambridge university press, 1995.

[87] R. Simon and N. Mukunda, "Optical phase space, Wigner representation, and invariant quality parameters," *Journal of Optical Society of America A*, vol. 17, no. 12, pp. 2440–2463, 2000.

[88] E. Wigner, "On the quantum correction for thermodynamic equilibrium," *Physical Review*, vol. 40, pp. 749–759, 1932.

[89] R. Simon and N. Mukunda, "Twisted Gaussian Schell-model beams," *Journal of Optical Society of America A*, vol. 10, no. 1, pp. 95–109, 1993.

[90] R. Simon, N. Mukunda, and B. Dutta, "Quantum-noise matrix for multimode systems: U(n) invariance, squeezing, and normal forms," *Physical Review A*, vol. 49, no. 3, p. 1567, 1994.

[91] L. Allen, M. W. Beijersbergen, R. J. C. Spreeuw, and J. P. Woerdman, "Orbital angular momentum of light and the transformation of Laguerre-Gaussian laser modes," *Physical Review A*, vol. 45, no. 11, p. 8185, 1992.

[92] A. Walther, "Radiometry and coherence," *Journal of Optical Society of America*, vol. 58, no. 9, pp. 1256–1259, 1968.

[93] V. I. Tatarskii, *The Effects of the Turbulent Atmosphere on Wave Propagation*. Israel Program for Scientific Translations, 1971.

[94] P. De Santis, F. Gori, G. Guattari, and C. Palma, "An example of a Collett-Wolf source," *Optics Communications*, vol. 29, no. 3, pp. 256–260, 1979.

[95] J. D. Farina, L. M. Narducci, and E. Collett, "Generation of highly directional beams from a globally incoherent source," *Optics Communications*, vol. 32, no. 2, pp. 203–208, 1980.

[96] S. Basu, M. W. Hyde, X. Xiao, D. G. Voelz, and O. Korotkova, "Computational approaches for generating electromagnetic Gaussian Schell-model sources," *Optics Express*, vol. 22, no. 26, pp. 31691–31707, 2014.

[97] M. W. Hyde, S. Basu, D. G. Voelz, and X. Xiao, "Experimentally generating any desired partially coherent Schell-model source using phase-only control," *Journal of Applied Physics*, vol. 118, no. 9, p. 093102, 2015.

[98] M. W. Hyde IV, S. Bose-Pillai, D. G. Voelz, and X. Xiao, "Generation of vector partially coherent optical sources using phase-only spatial light modulators," *Physical Review Applied*, vol. 6, no. 6, p. 064030, 2016.

[99] F. Gori, M. Santarsiero, R. Simon, G. Piquero, R. Borghi, and G. Guattari, "Coherent-mode decomposition of partially polarized, partially coherent sources," *Journal of Optical Society of America A*, vol. 20, no. 1, pp. 78–84, 2003.

[100] F. Gori, M. Santarsiero, S. Vicalvi, R. Borghi, and G. Guattari, "Beam coherence-polarization matrix," *Pure and Applied Optics: Journal of the European Optical Society Part A*, vol. 7, no. 5, p. 941, 1998.

[101] J. S. Ivan, N. Mukunda, and R. Simon, "Moments of non-gaussian wigner distributions and a generalized uncertainty principle: I. the single-mode case," *Journal of Physics A: Mathematical and Theoretical*, vol. 45, no. 19, p. 195305, 2012.

[102] S. Chaturvedi and N. Mukunda, "Entanglement and complete positivity: relevance and manifestations in classical scalar wave optics," *Fortschritte der Physik*, vol. 66, no. 2, p. 1700077, 2018.

[103] P. Chowdhury, A. S. Majumdar, and G. S. Agarwal, "Nonlocal continuous-variable correlations and violation of Bell's inequality for light beams with topological singularities," *Physical Review A*, vol. 88, no. 1, p. 013830, 2013.

[104] B. Ndagano, I. Nape, M. A. Cox, C. Rosales-Guzman, and A. Forbes, "Creation and detection of vector vortex modes for classical and quantum communication," *Journal of Lightwave Technology*, vol. 36, no. 2, pp. 292–301, 2018.

[105] W. Balthazar, C. Souza, D. Caetano, E. Galvão, J. Huguenin, and A. Khoury, "Tripartite nonseparability in classical optics," *Optics Letters*, vol. 41, no. 24, pp. 5797–5800, 2016.

[106] M. H. M. Passos, W. F. Balthazar, J. A. de Barros, C. E. R. Souza, A. Z. Khoury, and J. A. O. Huguenin, "Classical analog of quantum contextuality in spin-orbit laser modes," *Physical Review A*, vol. 98, no. 6, p. 062116, 2018.

[107] B. Ndagano, H. Sroor, M. McLaren, C. Rosales-Guzmán, and A. Forbes, "Beam quality measure for vector beams," *Optics Letters*, vol. 41, no. 15, pp. 3407–3410, 2016.

[108] V. D'Ambrosio, G. Carvacho, F. Graffitti, C. Vitelli, B. Piccirillo, L. Marrucci, and F. Sciarrino, "Entangled vector vortex beams," *Physical Review A*, vol. 94, no. 3, p. 030304, 2016.

[109] E. Otte, C. Rosales-Guzmán, B. Ndagano, C. Denz, and A. Forbes, "Entanglement beating in free space through spin-orbit coupling," *Light: Science & Applications*, vol. 7, no. 5, p. 18009, 2018.

[110] F. De Zela, "Optical approach to concurrence and polarization," *Optics Letters*, vol. 43, no. 11, pp. 2603–2606, 2018.

[111] A. Selyem, C. Rosales-Guzmán, S. Croke, A. Forbes, and S. Franke-Arnold, "Basis-independent tomography and nonseparability witnesses of pure complex vectorial light fields by Stokes projections," *Physical Review A*, vol. 100, no. 6, p. 063842, 2019.

[112] E. Wolf, *Introduction to the Theory of Coherence and Polarization of Light*. Cambridge university press, 2007.

[113] F. Gori, G. Guattari, C. Palma, and C. Padovani, "Specular cross-spectral density functions," *Optics Communications*, vol. 68, no. 4, pp. 239–243, 1988.

[114] P. Rungta, V. Bužek, C. M. Caves, M. Hillery, and G. J. Milburn, "Universal state inversion and concurrence in arbitrary dimensions," *Physical Review A*, vol. 64, no. 4, p. 042315, 2001.

[115] A. Uhlmann, "Fidelity and concurrence of conjugated states," *Physical Review A*, vol. 62, no. 3, p. 032307, 2000.

[116] C. H. Bennett, D. P. DiVincenzo, J. A. Smolin, and W. K. Wootters, "Mixed-state entanglement and quantum error correction," *Physical Review A*, vol. 54, no. 5, p. 3824, 1996.

[117] C. H. Bennett, G. Brassard, C. Crépeau, R. Jozsa, A. Peres, and W. K. Wootters, "Teleporting an unknown quantum state via dual classical and Einstein-Podolsky-Rosen channels," *Physical Review Letters*, vol. 70, no. 13, p. 1895, 1993.

[118] D. Clarke and J. F. Grainger, *Polarized light and optical measurement: international series of monographs in natural philosophy*, vol. 35. Elsevier, 2013.

[119] A. Peres, *Quantum theory: concepts and methods*. Springer, 1997.

[120] J. Leppäkangas, J. Braumüller, M. Hauck, J.-M. Reiner, I. Schwenk, S. Zanker, L. Fritz, A. V. Ustinov, M. Weides, and M. Marthaler, "Quantum simulation of the spin-boson model with a microwave circuit," *Physical Review A*, vol. 97, no. 5, p. 052321, 2018.

[121] S. Takeda, T. Mizuta, M. Fuwa, P. van Loock, and A. Furusawa, "Deterministic quantum teleportation of photonic quantum bits by a hybrid technique," *Nature*, vol. 500, no. 7462, pp. 315–318, 2013.

[122] H. Jeong, A. Zavatta, M. Kang, S.-W. Lee, L. S. Costanzo, S. Grandi, T. C. Ralph, and M. Bellini, "Generation of hybrid entanglement of light," *Nature Photonics*, vol. 8, no. 7, pp. 564–569, 2014.

[123] U. L. Andersen, J. S. Neergaard-Nielsen, P. van Loock, and A. Furusawa, "Hybrid discrete-and continuous-variable quantum information," *Nature Physics*, vol. 11, no. 9, pp. 713–719, 2015.

[124] A. A. Clerk and D. W. Utami, "Using a qubit to measure photon-number statistics of a driven thermal oscillator," *Physical Review A*, vol. 75, no. 4, p. 042302, 2007.

[125] F. Yoshihara, T. Fuse, S. Ashhab, K. Kakuyanagi, S. Saito, and K. Semba, "Superconducting qubit-oscillator circuit beyond the ultrastrong-coupling regime," *Nature Physics*, vol. 13, no. 1, pp. 44–47, 2017.

[126] I. Chiorescu, P. Bertet, K. Semba, Y. Nakamura, C. J. P. M. Harmans, and J. E. Mooij, "Coherent dynamics of a flux qubit coupled to a harmonic oscillator," *Nature*, vol. 431, no. 7005, pp. 159–162, 2004.

[127] W. Cheng, J. W. Haus, and Q. Zhan, "Propagation of vector vortex beams through a turbulent atmosphere," *Optics Express*, vol. 17, no. 20, pp. 17829–17836, 2009.

[128] M. A. Cox, N. Mphuthi, I. Nape, N. Mashaba, L. Cheng, and A. Forbes, "Structured light in turbulence," *IEEE Journal of Selected Topics in Quantum Electronics*, vol. 27, no. 2, pp. 1–21, 2020.

[129] Z. Zhu, M. Janasik, A. Fyffe, D. Hay, Y. Zhou, B. Kantor, T. Winder, R. W. Boyd, G. Leuchs, and Z. Shi, "Compensation-free high-dimensional free-space optical communication using turbulence-resilient vector beams," *Nature Communications*, vol. 12, no. 1, p. 1666, 2021.

[130] N. Mukunda, R. Simon, and E. C. G. Sudarshan, "Paraxial Maxwell beams: transformation by general linear optical systems," *Journal of Optical Society of America A*, vol. 2, no. 8, pp. 1291–1296, 1985.

[131] N. Mukunda, R. Simon, and E. C. G. Sudarshan, "Fourier optics for the Maxwell field: formalism and applications," *Journal of Optical Society of America A*, vol. 2, no. 3, pp. 416–426, 1985.

[132] R. A. Horn and C. R. Johnson, *Matrix analysis*. Cambridge university press, 2012.

[133] S. Mukhi and N. Mukunda, *Lectures on advanced mathematical methods for physicists*. World Scientific, 2010.

[134] X. Liu and K.-H. Brenner, "Minimal optical decomposition of ray transfer matrices," *Applied Optics*, vol. 47, no. 22, pp. E88–E98, 2008.

[135] P. A. A. Yasir and J. S. Ivan, "Realization of first-order optical systems using thin lenses of positive focal length," *Journal of Optical Society of America A*, vol. 34, no. 11, pp. 2007–2012, 2017.

[136] P. A. A. Yasir, "Realization of general first-order optical systems using nine thin cylindrical lenses of arbitrary focal length and four units of free propagation distance," *Journal of Optical Society of America A*, vol. 38, no. 5, pp. 644–653, 2021.

[137] R. Sharma, J. S. Ivan, and C. S. Narayanamurthy, "Wave propagation analysis using the variance matrix," *Journal of Optical Society of America A*, vol. 31, no. 10, pp. 2185–2191, 2014.

[138] G. Nemes and A. E. Siegman, "Measurement of all ten second-order moments of an astigmatic beam by the use of rotating simple astigmatic (anamorphic) optics," *Journal of Optical Society of America A*, vol. 11, no. 8, pp. 2257–2264, 1994.

[139] B. Schäfer and K. Mann, "Determination of beam parameters and coherence properties of laser radiation by use of an extended Hartmann-Shack wave-front sensor," *Applied Optics*, vol. 41, no. 15, pp. 2809–2817, 2002.

[140] J. Lavoie, R. Kaltenbaek, M. Piani, and K. J. Resch, "Experimental bound entanglement in a four-photon state," *Physical Review Letters*, vol. 105, no. 13, p. 130501, 2010.

[141] J. F. Clauser, M. A. Horne, A. Shimony, and R. A. Holt, "Proposed experiment to test local hidden-variable theories," *Physical Review Letters*, vol. 23, no. 15, p. 880, 1969.

[142] F. Gori, "Matrix treatment for partially polarized, partially coherent beams," *Optics Letters*, vol. 23, no. 4, pp. 241–243, 1998.

[143] J. R. Fienup, "Phase retrieval algorithms: a comparison," *Applied Optics*, vol. 21, no. 15, pp. 2758–2769, 1982.

[144] J. R. Fienup and C. C. Wackerman, "Phase-retrieval stagnation problems and solutions," *Journal of Optical Society of America A*, vol. 3, no. 11, pp. 1897–1907, 1986.

[145] R. Yazdani and H. Fallah, "Iterative phase retrieval algorithm for reconstruction of two arbitrary interfering fields," *Journal of Optical Society of America B*, vol. 35, no. 12, pp. 3063–3068, 2018.

[146] A. V. Martin and L. J. Allen, "Phase imaging from a diffraction pattern in the presence of vortices," *Optics Communications*, vol. 277, no. 2, pp. 288–294, 2007.

[147] R. Yazdani and H. Fallah, "Wavefront sensing for a Shack-Hartmann sensor using phase retrieval based on a sequence of intensity patterns," *Applied Optics*, vol. 56, no. 5, pp. 1358–1364, 2017.

[148] C. A. Henderson, G. J. Williams, A. G. Peele, H. M. Quiney, and K. A. Nugent, "Astigmatic phase retrieval: an experimental demonstration," *Optics Express*, vol. 17, no. 14, pp. 11905–11915, 2009.

[149] E. A. Akhlaghi, A. Darudi, and M. T. Tavassoly, "Reconstructing the phase distribution of two interfering wavefronts by analysis of their nonlocalized fringes with an iterative method," *Optics Express*, vol. 19, no. 17, pp. 15976–15981, 2011.

[150] C. Guo, S. Liu, and J. T. Sheridan, "Iterative phase retrieval algorithms. I: optimization," *Applied Optics*, vol. 54, no. 15, pp. 4698–4708, 2015.

[151] B. Shi, Q. Lian, X. Huang, and N. An, "Constrained phase retrieval: when alternating projection meets regularization," *Journal of Optical Society of America B*, vol. 35, no. 6, pp. 1271–1281, 2018.

[152] H. Chang, X.-l. Yin, X.-z. Cui, Z.-c. Zhang, J.-x. Ma, G.-h. Wu, L.-j. Zhang, and X.-j. Xin, "Adaptive optics compensation of orbital angular momentum beams with a modified Gerchberg-Saxton-based phase retrieval algorithm," *Optics Communications*, vol. 405, pp. 271–275, 2017.

[153] Y. Esashi, C.-T. Liao, B. Wang, N. Brooks, K. M. Dorney, C. Hernández-García, H. Kapteyn, D. Adams, and M. Murnane, "Ptychographic amplitude and phase reconstruction of bichromatic vortex beams," *Optics Express*, vol. 26, no. 26, pp. 34007–34015, 2018.

[154] R. W. Gerchberg and W. O. Saxton, "A practical algorithm for the determination of phase from image and diffraction plane pictures," *Optik*, vol. 35, no. 2, pp. 237–246, 1972.

[155] V. J. Deepak and J. S. Ivan, "Contextual phase estimation from two-plane intensity measurements," *Journal of Optical Society of America A*, vol. 33, no. 6, pp. 1198–1206, 2016.

[156] M. R. Teague, "Deterministic phase retrieval: a Green's function solution," *Journal of Optical Society of America*, vol. 73, no. 11, pp. 1434–1441, 1983.

[157] T. E. Gureyev, A. Roberts, and K. A. Nugent, "Phase retrieval with the transport-of-intensity equation: matrix solution with use of Zernike polynomials," *Journal of Optical Society of America A*, vol. 12, no. 9, pp. 1932–1941, 1995.

[158] G. J. Gbur, *Singular Optics*. CRC press, 2016.

[159] J. Frank, S. Altmeyer, and G. Wernicke, "Non-interferometric, non-iterative phase retrieval by Green's functions," *Journal of Optical Society of America A*, vol. 27, no. 10, pp. 2244–2251, 2010.

[160] A. Lubk, G. Guzzinati, F. Börrnert, and J. Verbeeck, "Transport of intensity phase retrieval of arbitrary wave fields including vortices," *Physical Review Letters*, vol. 111, no. 17, p. 173902, 2013.

[161] L. J. Allen, H. M. L. Faulkner, K. A. Nugent, M. Oxley, and D. Paganin, "Phase retrieval from images in the presence of first-order vortices," *Physical Review E*, vol. 63, no. 3, p. 037602, 2001.

[162] J. Vila-Comamala, A. Sakdinawat, and M. Guizar-Sicairos, "Characterization of x-ray phase vortices by ptychographic coherent diffractive imaging," *Optics Letters*, vol. 39, no. 18, pp. 5281–5284, 2014.

[163] V. Elser, "Phase retrieval by iterated projections," *Journal of Optical Society of America A*, vol. 20, no. 1, pp. 40–55, 2003.

[164] A. M. S. Maallo and P. F. Almoro, "Numerical correction of optical vortex using a wrapped phase map analysis algorithm," *Optics Letters*, vol. 36, no. 7, pp. 1251–1253, 2011.

[165] J. F. Nye and M. V. Berry, "Dislocations in wave trains," *Proceedings of the Royal Society of London. A. Mathematical and Physical Sciences*, vol. 336, no. 1605, pp. 165–190, 1974.

[166] L. Marrucci, C. Manzo, and D. Paparo, "Optical spin-to-orbital angular momentum conversion in inhomogeneous anisotropic media," *Physical Review Letters*, vol. 96, no. 16, p. 163905, 2006.

[167] A. M. Yao and M. J. Padgett, "Orbital angular momentum: origins, behavior and applications," *Advances in Optics and Photonics*, vol. 3, no. 2, pp. 161–204, 2011.

[168] Y. Qiao, W. Wang, N. Minematsu, J. Liu, M. Takeda, and X. Tang, "A theory of phase singularities for image representation and its applications to object tracking and image matching," *IEEE Transactions on Image Processing*, vol. 18, no. 10, pp. 2153–2166, 2009.

[169] J. Leach, J. Courtial, K. Skeldon, S. M. Barnett, S. Franke-Arnold, and M. J. Padgett, "Interferometric methods to measure orbital and spin, or the total angular momentum of a single photon," *Physical Review Letters*, vol. 92, no. 1, p. 013601, 2004.

[170] G. C. Berkhout, M. P. Lavery, J. Courtial, M. W. Beijersbergen, and M. J. Padgett, "Efficient sorting of orbital angular momentum states of light," *Physical Review Letters*, vol. 105, no. 15, p. 153601, 2010.

[171] G. C. G. Berkhout, M. P. J. Lavery, M. J. Padgett, and M. W. Beijersbergen, "Measuring orbital angular momentum superpositions of light by mode transformation," *Optics Letters*, vol. 36, no. 10, pp. 1863–1865, 2011.

[172] Y. Zhou, M. Mirhosseini, D. Fu, J. Zhao, S. M. H. Rafsanjani, A. E. Willner, and R. W. Boyd, "Sorting photons by radial quantum number," *Physical Review Letters*, vol. 119, no. 26, p. 263602, 2017.

[173] S. N. Alperin, R. D. Niederriter, J. T. Gopinath, and M. E. Siemens, "Quantitative measurement of the orbital angular momentum of light with a single, stationary lens," *Optics Letters*, vol. 41, no. 21, pp. 5019–5022, 2016.

[174] V. V. Kotlyar, A. A. Kovalev, and A. P. Porfirev, "Astigmatic transforms of an optical vortex for measurement of its topological charge," *Applied Optics*, vol. 56, no. 14, pp. 4095–4104, 2017.

[175] V. V. Kotlyar, A. A. Kovalev, and A. P. Porfirev, "Calculation of fractional orbital angular momentum of superpositions of optical vortices by intensity moments," *Optics Express*, vol. 27, no. 8, pp. 11236–11251, 2019.

[176] A. A. Kovalev, V. V. Kotlyar, A. P. Porfirev, and D. S. Kalinkina, "Measuring the orbital angular momentum of light beams by using a single intensity distribution," in *Journal of Physics: Conference Series*, vol. 1400, p. 066025, IOP Publishing, 2019.

[177] A. Volyar, M. Bretsko, Y. Akimova, and Y. Egorov, "Measurement of the vortex and orbital angular momentum spectra with a single cylindrical lens," *Applied Optics*, vol. 58, no. 21, pp. 5748–5755, 2019.

[178] A. Bekshaev, L. Mikhaylovskaya, S. Patil, V. Kumar, and R. P. Singh, "Optical-vortex diagnostics via Fraunhofer slit diffraction with controllable wavefront curvature," *Journal of Optical Society of America A*, vol. 37, no. 5, pp. 780–786, 2020.

[179] V. V. Kotlyar, A. A. Kovalev, and A. V. Volyar, "Topological charge of a linear combination of optical vortices: topological competition," *Optics Express*, vol. 28, no. 6, pp. 8266–8281, 2020.

[180] C. Schulze, A. Dudley, D. Flamm, M. Duparre, and A. Forbes, "Measurement of the orbital angular momentum density of light by modal decomposition," *New Journal of Physics*, vol. 15, no. 7, p. 073025, 2013.

[181] J. Chen, X. Liu, J. Yu, and Y. Cai, "Simultaneous determination of the sign and the magnitude of the topological charge of a partially coherent vortex beam," *Applied Physics B*, vol. 122, pp. 1–12, 2016.

[182] M. Mirhosseini, M. Malik, Z. Shi, and R. W. Boyd, "Efficient separation of the orbital angular momentum eigenstates of light," *Nature Communications*, vol. 4, no. 1, p. 2781, 2013.

[183] M. W. Beijersbergen, R. P. C. Coerwinkel, M. Kristensen, and J. P. Woerdman, "Helical-wavefront laser beams produced with a spiral phaseplate," *Optics Communications*, vol. 112, no. 5-6, pp. 321–327, 1994.

[184] S. N. Khonina, V. V. Kotlyar, M. V. Shinkaryev, V. A. Soifer, and G. V. Uspleniev, "The phase rotor filter," *Journal of Modern Optics*, vol. 39, no. 5, pp. 1147–1154, 1992.

[185] V. Kotlyar, A. Kovalev, A. Porfirev, and E. Kozlova, "Orbital angular momentum of a laser beam behind an off-axis spiral phase plate," *Optics Letters*, vol. 44, no. 15, pp. 3673–3676, 2019.

[186] V. V. Kotlyar, A. A. Almazov, S. N. Khonina, V. A. Soifer, H. Elfstrom, and J. Turunen, "Generation of phase singularity through diffracting a plane or Gaussian beam by a spiral phase plate," *Journal of Optical Society of America A*, vol. 22, no. 5, pp. 849–861, 2005.

[187] G. Gibson, J. Courtial, M. J. Padgett, M. Vasnetsov, V. Pas'ko, S. M. Barnett, and S. Franke-Arnold, "Free-space information transfer using light beams carrying orbital angular momentum," *Optics Express*, vol. 12, no. 22, pp. 5448–5456, 2004.

[188] M. Krenn, R. Fickler, M. Fink, J. Handsteiner, M. Malik, T. Scheidl, R. Ursin, and A. Zeilinger, "Communication with spatially modulated light through turbulent air across Vienna," *New Journal of Physics*, vol. 16, no. 11, p. 113028, 2014.

[189] D. L. Andrews and M. Babiker, *The angular momentum of light*. Cambridge University Press, 2012.

[190] G. Gbur and R. K. Tyson, "Vortex beam propagation through atmospheric turbulence and topological charge conservation," *Journal of Optical Society of America A*, vol. 25, no. 1, pp. 225–230, 2008.

[191] S. Franke-Arnold, L. Allen, and M. Padgett, "Advances in optical angular momentum," *Laser & Photonics Reviews*, vol. 2, no. 4, pp. 299–313, 2008.

[192] S. Ramee and R. Simon, "Effect of holes and vortices on beam quality," *Journal of Optical Society of America A*, vol. 17, no. 1, pp. 84–94, 2000.

[193] J. S. Ivan and K. Goswami, "Free space optical communication using beam parameters with translational and transverse rotational invariance," *Journal of Optical Society of America A*, vol. 32, no. 6, pp. 1118–1125, 2015.

[194] B. H. Swaliha, S. Asokan, and J. S. Ivan, "Estimation of dislocated phases and tunable orbital angular momentum using two cylindrical lenses," *Applied Optics*, vol. 62, no. 12, pp. 3083–3092, 2023.